UNIVERSITY
OF TRENTO - Italy
DEPARTMENT OF INDUSTRIAL ENGINEERING

Doctoral School in Material Science and Engineering
XXIV cycle

Production and Performance of Cu-based anode-supported tubular IT-SOFCs

Andrea Azzolini

Tutor
Prof. Ing. V. M. Sglavo

Doctoral Committee:
Prof. P. Scardi, Universita degli Studi di Trento
Prof, I. Robinson, University College of London
Dott.ssa P. Frontera, Università Mediterranea di Reggio Calabria

pe' fa' 'e cose bone ce vo' tiemp'

Cosimo Rummo,
Mastro Pastaio in Benevento dal 1846

Abstract

Tubular SOFCs were produced by extrusion of the supporting anode composed by GDC10 and Cu oxides. A 10 µm thin GDC10 electrolytic layer and the LSF20:GDC10 cathode were deposited by dip-coating and the complete cell was co-sintered in one step. Thanks to the optimization of the composition and the employment of Li_2O as sintering aid, the densification of the electrolyte was accomplished more than 500°C below the sintering temperature of GDC10. The cell had a maximum OCV of 0.54 V and the highest measured power density was 8.98 mW cm^{-2} with a peak power density projected to be 27.5 mW cm^{-2}.

Table of Contents

1. Introduction

The SOFC technology allows the conversion of the chemical energy of a fuel in electrical energy with efficiencies higher than any other known device. Although its discovery dates back to the 70's, its diffusion is still not as wide as it was expected. The reasons are multiple and mostly related to economic factors. SOFCs with performances and reliability that would allow their commercialization are still limited to operate with hydrogen and it is well established that an H_2-based economy is not a feasible option. To slow down the possibilities of further applications, there are several problems arising when the state-of-the-art materials have to be adapted to new and more complex fuels. One above all, is the carbon deposition on the nickel particles composing the conductive phase of the anodic cermet. And this is caused primarily because the carbon produced by some reactions when hydrocarbons are used to fuel the cell, is relatively soluble in the metallic nickel. Carbon deposits are formed on the metal surface and grow until they become complex structures that irreparably damage the anode. Many efforts were and still are aimed to the research of a material that could represent an alternative to nickel but still having similar properties such as conductivity and cost. Among the possible alternatives, copper has always been one of the most favored, both for its high conductivity, its low cost and its inertness to the carbon deposition. However, two are the aspects that hinder this material to become the new state-of-the-art anodic conductor for cell operated with hydrocarbons: the low melting temperature of the metal and its oxides and the considerably low value of thermal expansion coefficient.

The motivation of the work contained in this thesis regards the simple, rapid and cost-effective realization of tubular SOFCs able of being operated with unconventional fuels, hence not containing nickel in their anodic composition. The substitution of nickel with copper in the anodic cermet was the starting point that conditioned most of the successive steps of the project. Copper, although having an optimal electronic conductivity and low cost, does not catalyze the formation of carbon deposits on its surface. However, its low melting temperature strongly limits the maximum operating temperature of the cell. Then the selection of the anode-supported configuration and of an electrolyte with improved ionic conductivity in the intermediate temperature range was consequential. GDC10, chose as electrolytic material, necessitates high sintering temperature during the fabrication step. Thanks to the employment of sintering aids, the temperature required for the adequate densification of the gas-tight electrolyte could be lowered below the melting temperature of the

copper oxides, essential for maintaining a well-connected metallic network. A study on the effect of the doping with different sintering aids on the GDC10 and on the mechanism suggested for their functioning, is covered in Chapter 4.
Ceramic extrusion is one of the most diffused techniques to produce tubular cells. It is rapid, cost-effective and permits the fabrication of resistant supports with uniform density. A preliminary study regarding the formulation of ceramic extrusion pastes, the design and realization of the lab-scale ram extruder and the extrusion procedure is contained in Chapter 3. This was functional to the realization of GDC10-Cu cermet tubes to be used as support for tubular SOFCs. The anode-supported configuration, while it permits to decrease the electrolyte thickness, it requires co-sintering anode and electrolyte in one single sintering step. Then, an investigation on the electrolyte constrained densification on tubular supports with different copper oxide and doping contents was required and is covered in Chapter 5.
In Chapter 6, finally, the analysis of the production process and electrochemical performance of complete tubular anode-supported SOFCs and a comparison of the feasibility of using copper oxide as electronic conductive phase in a cermet anode is proposed.

Trento, Friday 5th December 2014

2. Background

A Solid Oxide Fuel Cell (SOFC) is a ceramic device capable of converting the chemical energy of a fuel in to electrical energy directly and without transforming it in to other forms of energy, like mechanical energy in the case of combustion heat engines. The conversion occurs through electrochemical combination of the reactants, exactly as in a conventional battery. Unlike a battery though, a SOFC does not discharge with time but generates electricity as long as the fuel and the oxidant are supplied to the electrodes. Considering that in a SOFC the chemical energy is not converted in thermal energy by combustion, as happens in the conventional thermal power system, its efficiency does not obey to the Carnot cycle limitation. The efficiency of an ideally reversible heat engine operating between two temperatures T_1 and T_2 with $T_1 < T_2$ is given by:

$$\eta = 1 - \frac{T_1}{T_2} \qquad (2.1)$$

To obtain high efficiencies, the difference between T_2 and T_1 has to be as large as possible. However practical limitations due to stability of the materials prevent reaching very high temperatures and an internal combustion engine cannot produce mechanical power at greater than 20 to 30% efficiency. A SOFC, instead, obtains efficiency values higher than any other known thermal device: between 50 and 65% when converting fuel to electricity and if the heat they produce is also harnessed, in combined heat and power, their overall efficiency can reach over 80%, almost independently from the size of the unit. The absence of moving parts and noise during operation together with the theoretical flexibility of using different fuels, make the SOFC one of the most versatile and promising device for energy conversion. In this chapter, the principles of functioning of the cell are introduced, followed by a discussion on the materials used for its fabrication. Particular importance is given to the issues emerging in case of operation with fuels alternative to hydrogen and methods to solve them are proposed. Finally, the most common configurations and architectures are presented with special attention to the fabrication method considered in the following experimental section.

2.1 Thermodynamics and efficiency of a SOFC.

The basic functioning of a SOFC relies on the discovery of solid ions conducting materials. Through substitution of host ions with aliovalent ions in various crystalline oxides structures, the concentration of oxygen vacancies is increased creating conduction paths for oxygen ions but with negligible electronic conductivity. Oxygen ion conductivity was first observed at the end of the 19th century by Nerst[1] in Zr_2O doped with Y_2O_3 and the first solid oxide fuel cell was constructed by Baur and Preis[2] using that same material as electrolyte in 1937.

In a SOFC, a solid electrolyte is sandwiched between two electrically conductive electrodes: the anode (or fuel electrode) and the cathode (or air electrode) connected by the external current collector as shown in Fig. 2.1. At the cathode side, the oxidant is reduced thanks to the catalytic action of the cathode material and to an excess of electrons. The oxygen ions can then occupy the vacancies present in the electrolyte and can travel through the conduction path by hopping, driven by the gradient of the oxygen partial pressure between the two sides of the cell. When they reach the anode, they are used to oxidize the fuel, releasing electrons to the external circuit and by-products depending on the fuel employed. The electrons produced are needed at the cathode side, where the reduction take place, and move to the cathode travelling through the external current collector, closing the circuit. In principle, and thanks to the high temperature of operation, any gas capable of being electrochemically oxidized can be used as fuel in a SOFC. Hydrogen is originally and currently the fuel more commonly employed, thanks to its high electrochemical reactivity and the simplicity of the reactions involved.

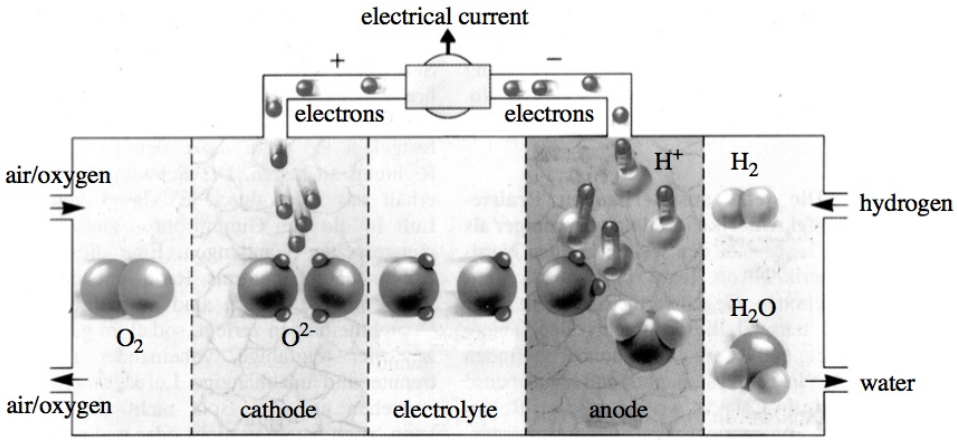

Fig. 2.1 Schematic representation of the operating principle of a SOFC. Hydrogen is oxidized at the anode; oxygen is reduced at the cathode. The oxygen ions diffuse through the electrolyte to the anode side, where water is generated[3].

The fuel cell reaction is a chemical process that can be divided into two electrochemical half-cell reactions. We shall consider the redox reactions of oxygen on both sides of the cell. The subscripts *c*, *a*, and *e* stands for the states at the cathode, anode and electrolyte. As stated above, the oxygen molecule is reduced at the cathode following the reaction:

$$O_{2(c)} + 4e^- = 2O^{2-}_{(e)} \qquad (2.2)$$

At the anode, the inverse reaction can be considered thermodynamically as the primary reaction:

$$2O^{2-}_{(e)} = O_{2(a)} + 4e^- \qquad (2.3)$$

The overall reaction can be expressed as:

$$O_{2(c)} = O_{2(a)} \qquad (2.4)$$

A SOFC can be considered preliminary as a concentration cell, where the reversible thermodynamic voltage E_r is defined by the partial pressure of oxygen on both sides of the cell and is described by Nerst equation:

$$E_r = \frac{RT}{4F} \ln \frac{P_{O_{2(c)}}}{P_{O_{2(a)}}} \qquad (2.5)$$

Where R (8.314 J/K·mol) is the gas constant, T the temperature in Kelvin, F the Faraday constant ($9.648 \cdot 10^4$ C/mol) and P_{O_2} the oxygen partial pressure at the cathode (c) or anode (a). At the anode side, the oxygen partial pressure depends on the type and composition of the employed fuel. For the simple case of H_2, the anode reaction is:

$$H_{2(a)} + \frac{1}{2} O_{2(a)} = H_2O_{(a)} \qquad (2.6)$$

The equilibrium constant K of the reaction can be expressed as:

$$K = \frac{P_{H_2O_{(a)}}}{P_{H_{2(a)}} \cdot \sqrt[2]{P_{O_{2(a)}}}} \qquad (2.7)$$

The oxygen partial pressure at the anode is then given by:

$$P_{O_{2(a)}} = \left(\frac{P_{H_2O_{(a)}}}{P_{H_{2(a)}} \cdot K}\right)^2 \tag{2.8}$$

and the Nerst equation becomes:

$$E_r = E^0 + \frac{RT}{4F} \ln P_{O_{2(c)}} + \frac{RT}{2F} \ln \frac{P_{H_2(a)}}{P_{H_2O_{(a)}}} \tag{2.9}$$

Where:

$$E^0 = \frac{RT}{2F} \ln K \tag{2.10}$$

Is the reversible voltage at standard state, i.e. when the partial pressures (or fugacities) of the reactants are equal to unity. The reversible voltage is related to the standard Gibbs free energy change of the reaction by the equation:

$$\Delta G = -nFE \tag{2.11}$$

Where n is the number of moles of oxygen required to oxidize the fuel. If the reactants and the products are in their standard state, the equation becomes:

$$\Delta G^0 = -nFE^0 \tag{2.12}$$

The standard Gibbs free energy change ΔG^0 gives an indication whether the reaction is spontaneous and thermodynamically favored ($\Delta G^0 < 0$) or not ($\Delta G^0 > 0$) and is defined by using the standard enthalpy change ΔH^0, and the standard entropy change ΔS^0:

$$E^0 = -\frac{\Delta G^0}{nF} = -\frac{\Delta H^0 - T\Delta S^0}{nF} \tag{2.13}$$

ΔG^0 corresponds to the maximum electrical work output obtainable from the reaction (2.6), ΔH^0 indicates the total thermal energy available by the same reaction at constant pressure and $T\Delta S^0$ is the amount of heat released or absorbed. Thus the ideal thermodynamic efficiency can be defined as:

$$\epsilon_T = \frac{\Delta G^0}{\Delta H^0} \tag{2.14}$$

In Fig. 2.2 some thermodynamic function for several of the most common reactions in a SOFC are reported. It is noteworthy that for carbon and methane oxidation, the thermodynamic efficiency is ~1.

Reaction	T, K	ΔG^0, kJ	ΔH^0, kJ	E^0, V	ϵ_T
$H_2 + ½O_2 = H_2O$	1000	-192.5	-247.3	0.997	0.78
	1250	-178.2	-249.8	0.924	0.71
$CO + ½O_2 = CO_2$	1000	-195.4	-283.3	1.013	0.69
	1250	-173.2	-283.3	0.898	0.61
$CH_4 + 2O_2 = CO_2 + 2H_2O$	1000	-802.5	-800.4	1.039	1.00
	1250	-802.9	-801.2	1.039	1.00
$C + O_2 = CO_2$	1000	-396.6	-396.2	1.027	1.00
	1250	-396.6	-396.6	1.027	1.00

Fig. 2.2 Standard Gibbs free energy and enthalpy change, Nerst voltage and thermodynamic efficiency for some common reactions in a SOFC[4].

The effect of temperature and pressure on the reversible voltage can be shown by differentiating the reversible voltage from Eq. 2.11 with respect to temperature and pressure for a general (non-standard) state:

$$\left(\frac{\partial E}{\partial T}\right)_P = \frac{\Delta S}{nF} \tag{2.15}$$

$$\left(\frac{\partial E}{\partial P}\right)_T = -\frac{\Delta V}{nF} \tag{2.16}$$

Where ΔV is the change in volume. In case of hydrogen and carbon monoxide oxidation, $\Delta S < 0$ then an increase in temperature correspond to a decrease in E_r. Contrarily for the direct oxidation of methane, $\Delta H \approx \Delta G$ so that $\Delta S \sim 0$ and the reversible voltage is mostly independent of temperature and pressure (Fig. 2.3). In actuality direct electrochemical oxidation usually represent only a minor contribution to the oxidation of methane, which passes through a more complicated set of reactions when oxidized that will be indicated later in this chapter.

The value of E_r calculated in Eq. 2.9 is the voltage between the two electrodes when no current is flowing, also called the Open Circuit Voltage (OCV) and depends on the temperature, the type of fuel and reactions and the partial pressure of the reactants and products. The comparison of the theoretical value and the operating OCV allows for the verification that the partial pressure gradient between the two electrodes is maintained and there is not gas leakage through the electrolyte.

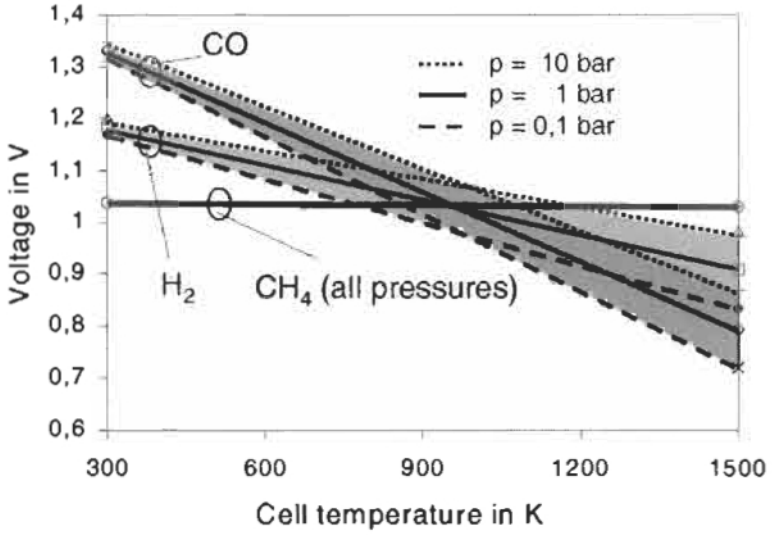

Fig. 2.3 Open circuit voltages as evaluated from the Nerst equation for the oxidation reactions of CO, H_2 and CH_4 as function of operating temperature and partial pressure of the reactants[4].

When the two electrodes are connected through a load and the electrons flow along the circuit, the voltage drops below its reversible value due to several irreversible effects. The efficiency of a stand-alone SOFC in operation cannot be fully understood with just the thermodynamic efficiency of the reaction but it may be written as products of several contributions:

$$\epsilon_{FC} = \epsilon_T \epsilon_V \epsilon_J \epsilon_H \tag{2.17}$$

Where the subscript T stands for the thermodynamic efficiency of the reaction, V for the voltage efficiency, J for the Faradaic or current efficiency and H for the heating value efficiency.
The voltage efficiency ϵ_V is defined as the ratio of the operating cell voltage under load to the reversible voltage:

$$\epsilon_V = \frac{E}{E_r} \tag{2.18}$$

The loss of voltage during operation depends on the current density and it is called polarization (or overpotential) η:

$$E = E_r - \eta \tag{2.19}$$

The total polarization of the cell can be expressed as the sum of four types of polarization: the activation polarization η_A, the concentration polarization η_D and the ohmic polarization η_Ω:

$$\eta = \eta_A + \eta_D + \eta_\Omega \qquad (2.20)$$

These contributions can be minimized by the careful choice of the materials used, cell design and temperature and pressure of operation.
The activation polarization η_A depends on the energy barrier, or the activation energy, that has to be overcome by the reagent to react (be oxidized or reduced). It is generally due to one or more rate limiting reactions among all the electrode reactions and in case of electrochemical reactions with $\eta_A \geq 50 - 100$ mV is approximated by the semi-empirical Tafel equation:

$$\eta_A = a \pm b \log j \qquad (2.21)$$

Where a and b are constants related to the electrode material, its catalytic activity and the type of the electrode reaction and j is the current density. Due to the typically high temperature of operation, the activation polarization of a SOFC is generally small.
The concentration polarization η_D is due to this insufficient velocity of reacting and reacted species to and away from the reaction sites as more current is drawn from the cell. As larger currents are drawn from the cell, the reactions become faster and the reacting species begin to be depleted in one or both of the electrodes. When the limiting reaction step is completely dominated by the diffusion of the species to and away from the electrodes, a limiting current j_L is reached which is a function of the diffusion coefficient D, the activity of the reacting ions a_M and the thickness of the diffusion layer δ as shown by the Fick's law:

$$j_L = \frac{nFDa_M}{\delta} \qquad (2.22)$$

For an electrode process with negligible activation polarization, the concentration polarization is expressed by:

$$\eta_D = \frac{RT}{nF} \ln\left(1 - \frac{j}{j_L}\right) \qquad (2.23)$$

This contribution to the total polarization becomes important as the current density j tends to its limiting value, which strongly depends not only on the temperature, pressure and concentration of the reacting species but also on the ease of access to the reacting sites at the electrodes. Therefore parameters such as electrodes thickness, porosity, pore size and pore morphology affect this type of polarization.
The ohmic polarization is the voltage drop due to the resistance of the cell, both for ionic conduction through the electrolyte and the electronic conduction in the

electrodes and the current collector. The ohmic polarization can be expressed by Ohm's law:

$$\eta_{\Omega} = jR_{tot} \tag{2.24}$$

Where R_{tot} is the total resistance of the cell. Although optimizing the electronic conductivity of the electrodes could diminish this contribution, it is mostly dependent on the ionic conductivity of the electrolyte. A careful selection of the electrolytic materials, temperature of operation and fabrication of thin and dense electrolytes may be helpful to decrease this type of polarization.
The current efficiency ϵ_J is the ratio of the actual current withdrawn and the current available from the complete conversion of the fuel. If some of the fuel is not consumed, the current density j is expressed by Faraday's law:

$$j = nF\left(\frac{df}{dt}\right)_{consumed} \tag{2.25}$$

Where df/dt is the molar flow rate of the fuel. The current efficiency is given by:

$$\epsilon_V = \frac{j}{j_F} \tag{2.26}$$

Where j_F is the current density available from the complete fuel oxidation.
The heating value efficiency ϵ_H may be considered in case the fuel is not pure but contains some electrochemically inactive species and is expressed as the ratio of the amount of heat of fuel species available to produce electricity to the total amount of heat energy contained in all the combustible species in the fuel gas. Considering all three types of polarization, the typical current-voltage plot of an operating fuel cell is shown in Fig. 2.4.
For low current densities, the major contribution to the voltage drop is attributed to the activation polarization. Increasing the current density, the voltage drops linearly, meaning that the ohmic losses are predominant in this range. When the current reaches high values, mass transport effects become important and the rapid voltage drop observed is attributed to the concentration polarization.

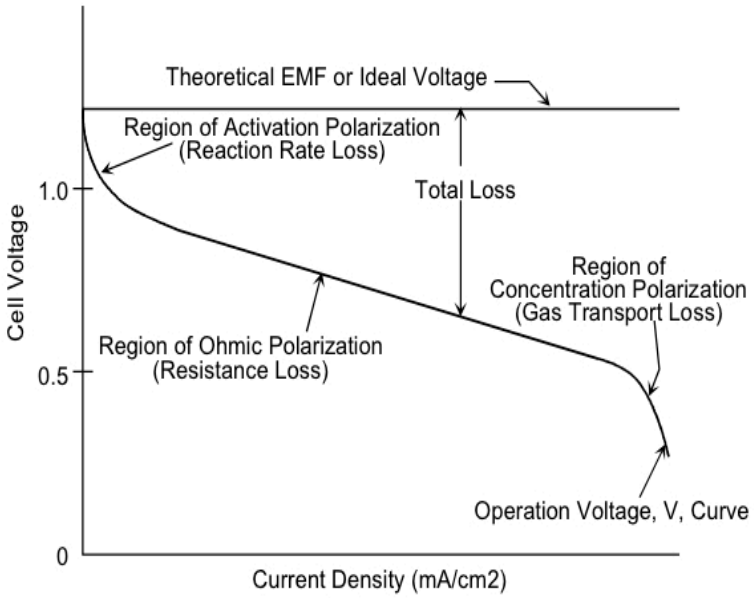

Fig. 2.4 Typical current-voltage plot of a SOFC. The different polarization contribution to the voltage drop are indicated[3].

The power output P_W of an operating cell is given by the product of the operating voltage E and the current I:

$$P_W = EI \tag{2.27}$$

Considering the effect of the overpotential on the operating voltage, the plot of the power output may be represented as in Fig. 2.5.

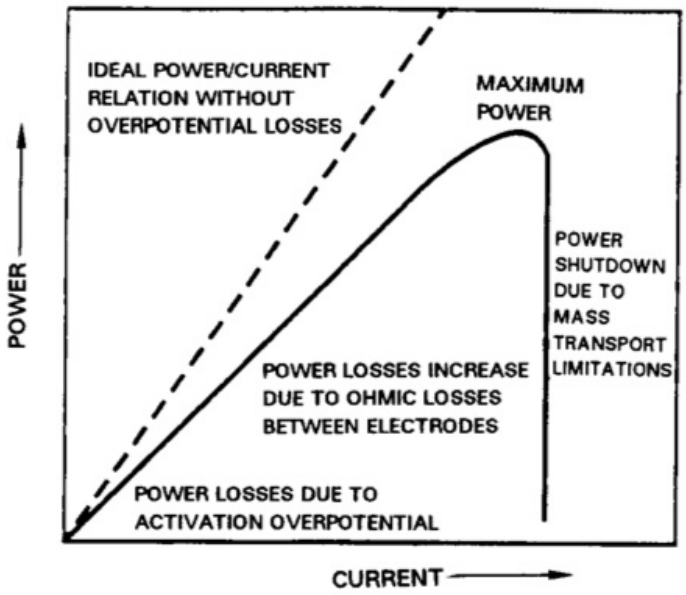

Fig. 2.5 Typical power-current plot of an operating SOFC compared to its ideal performance[3].

The power drops to zero for extreme values of current and has a maximum in betweeen. Considering that in first approximation the main contribution to the overpotential is ohmic, the relationship between voltage and current density tends to be linear and it can be written as:

$$E = E_r - \epsilon_\Omega = E_r - R_t I \tag{2.28}$$

This translates into a parabolic expression for power given by:

$$P_W = IE_r - I^2 R_t \tag{2.29}$$

In this case, the value of current relative to the maximum power is found by equating the derivative of Eq. 2.29 with respect to the current to zero:

$$\frac{dP_W}{dI} = 0 \tag{2.30}$$

$$I_{Pmax} = \frac{E_r}{2R_t} \tag{2.31}$$

Substituting the current from Eq. 2.31 in Eq. 2.28 gives the operating voltage relative to maximum power output:

$$E_{Pmax} = \frac{E_r}{2} \tag{2.32}$$

The maximum power is then achieved when the cell voltage is operated at one-half of the reversible voltage and in this case, the voltage efficiency ϵ_V is 50%. Therefore, A SOFC device can be operated in different regimes, depending on what is suitable for a certain type of application. For example, operation at low current densities is less affected by overpotentials and delivers low voltage with high efficiency. This type of operating parameters would be more suitable for stationary application, where the size of the cell stack is not a limiting factor and it can be increased to achieve higher power output. For a cell operated at high current densities, the power output is higher but the voltage and efficiency are lower. Mobile applications, where the size and weight of the stack are issues, need to achieve high power volumetric density and are preferably operated in this regime.

2.2 Materials and cell components.

A SOFC is essentially made by a series of solid layers one on top of the other with the dense electrolyte sandwiched between two porous electrodes. The selection of materials used for the different SOFC elements is constrained by many factors more than just their specific role in the device. The operating temperature, the architecture, choice of fabrication method and the selection of materials used for the other cell components are all parameters to consider carefully when designing a SOFC. Then, in addition to the ionic conductivity of the electrolyte and the electronic conductivity, porosity, resistance to high temperature in reducing and oxidizing environments and catalytic activity of the electrodes, the materials composing a SOFC have to be selected for their mechanical and chemical compatibility in every step of fabrication and operation. The layered structure of a SOFC, in fact, typically requires a high temperature treatment aimed to achieve a dense, and possibly thin, electrolytic layer to avoid gas leakage between the electrodes and to minimize the contribution of the ionic resistance. Depending on the fabrication procedure selected and on the cell configuration, more cell components may be subjected to the same heat treatment of the electrolyte, which usually requires the highest temperature and longest sintering cycle. Therefore, the materials employed have to be stable and compatible in both heating and cooling stages of sintering. The selection of materials and compositions based on similar behavior during sintering and matching coefficients of thermal expansion (CTE) during cooling is then an important phase of the design of a SOFC because it can avoid the onset of large residual stresses, fractures and debondings. In the following sections, general requirements of cell components are discussed and materials of interest are reviewed. Particular attention is devoted toward materials employed and issues encountered later in this work.

2.2.1 Electrolyte

The principal characteristic of the electrolyte layer in a SOFC is its ability to conduct ions without conducting electrons. The electric conduction in solid with crystalline structure, discovered in silver iodide (AgI) and doped zirconia in the early half of the 20th century, is due to the movement of cations or anions. Among the anionic conductors, the oxygen ion conductors represent one of the most extensively study classes of materials and they are the conventional choice for the electrolyte in for fuel cell application. The ionic conduction in solid electrolyte is primarily determined by the presence of lattice defects. These defects can be stoichiometric (Frenkel and Schottky) when the crystal composition is not modified, or non-stoichiometric (Koch-Wagner) when the

defects are appositely created by modification of the crystal composition. A Frenkel-type defect is spontaneously created as consequence of the random movement of one ion in a metastable interstitial position of the lattice. The oppositely charged vacancy created in this way, can be occupied by another ion. As result of this mechanism, the vacancy can be seen as a separate entity free to move around the crystal. Schottky-type defects consist of anions and cations pairs missing from their lattice sites, creating vacancies but maintaining both the electric and stoichiometry neutrality. This latter type of defects are created when anion and cation posses roughly the same ionic radius.

Being thermally activated processes, the concentration of stoichiometric defects manly depends on the temperature. The oxygen partial pressure P_{O_2} has also considerable relevance: for values superior to those required maintaining stoichiometry, the oxide becomes metal-deficient with excess of interstitial oxygen. The negative charge is balanced by electrons holes produced by the thermal activation of the electrons from the valence band to the conduction band. So in this regime, electrons holes are the main charge carrier with a concentration usually increasing with P_{O_2}, and the electrolyte loses functionality because the electrodes are short-circuited. Similarly, in the case of lower oxygen partial pressure respect to stoichiometric condition, the oxide is rich in oxygen vacancies and free electrons are the main defects[5]. In general, though, for every condition of temperature and partial pressure, the ionic conductivity of pure solid oxide is too low for be suitable for SOFC electrolyte application.

The defects, more than occur intrinsically in the solid, can also be created by substitution of atoms of the crystal with aliovalent atoms (Koch-Wagner type). For example, by dissolving a trivalent oxide as Y_2O_3 in quadravalent ZrO_2, the substitution of a Zr^{4+} with an ion Y^{3+} causes the production of a net negative charge. To maintain the electro neutrality, for every two negative charges, an O^{2-} ion is removed from the solid, creating an oxygen vacancy with valence (2+). The oxygen ions conduction occurs by diffusion of oxygen ions through these vacancies. Also in the case of extrinsic defects, there are different domains of main charge carriers based on the oxygen partial pressure. In addition to the two domains already introduced, for intermediate values of P_{O_2}, the vacancy concentration is almost completely determined by the dopant content. The ionic conductivity is by far larger than that produced by other charge carriers like electrons or holes and, inside the range, independent of the value of P_{O_2}.

Even if ionic conductivity was recently observed in many materials with perovskite, brownmillerite or hexagonal crystal lattices, the majority of the oxygen ion conductors have the cubic fluorite lattice. It is a rather open structure, characterized by a large number of interstitial voids, which allow improved ions diffusion compared to other lattices. Belonging to this category, Yttria stabilized zirconia (YSZ), belongs to this category, and was the first material ever employed as a solid electrolyte and is still the state of the art

material for high temperature SOFCs. But also other oxides such as thoria, bismuth trioxide and ceria, crystallize in this form. Fig. 2.6 and 2.7 show the ionic conductivity versus temperature for some of the most employed electrolytic materials for high (Fig. 2.6) and intermediate temperature (Fig. 2.7) ranges.

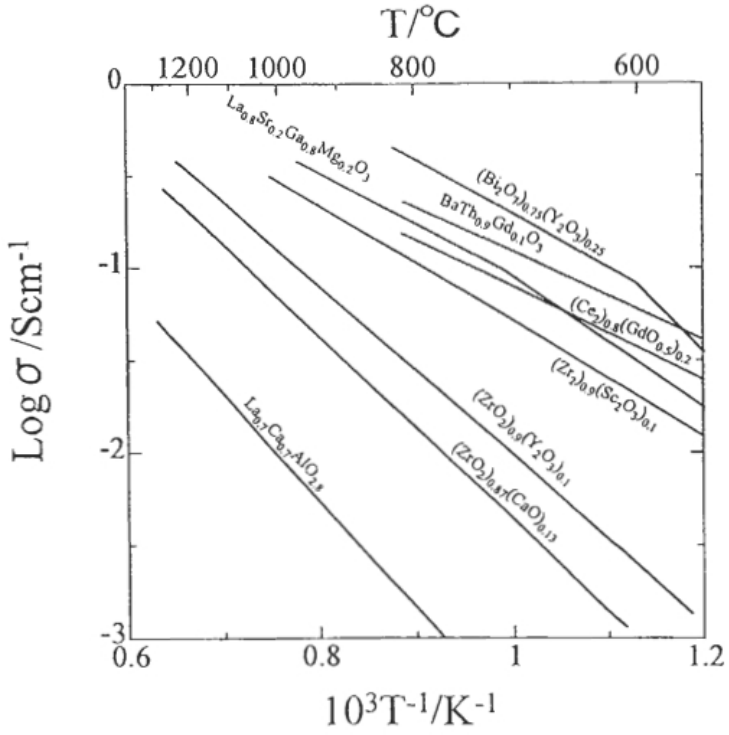

Fig. 2.6 Conductivity of some oxide ion conductors in high temperature range[6].

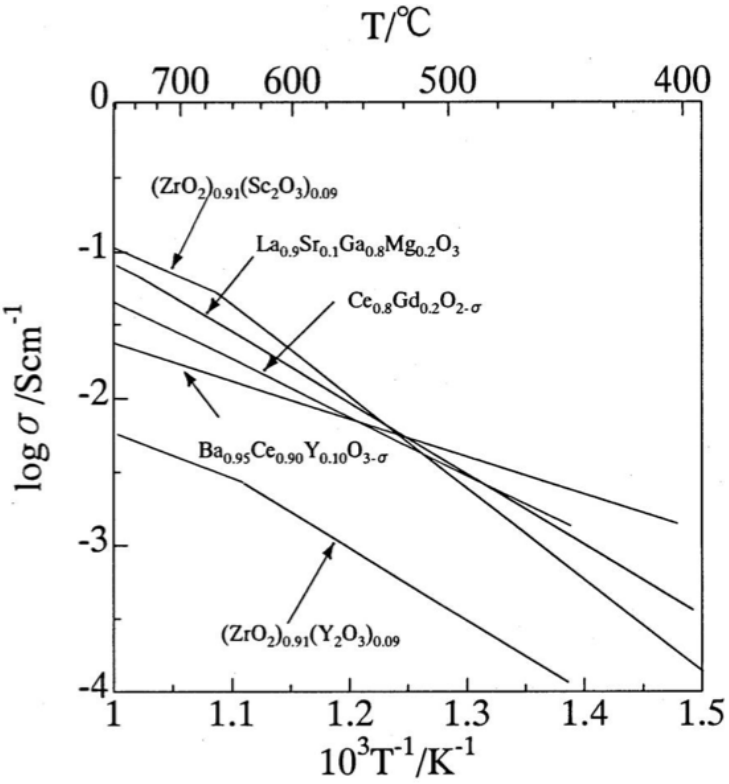

Fig. 2.7 Conductivity of some oxide ion conductors in intermediate temperature range[6].

Although it can be noticed that YSZ is not the best ionic conductors, the others materials typically share other issues such as cost, difficulty in processing and onset of electronic conduction for some conditions. At the present state YSZ is the state-of-the-art electrolyte for high temperature SOFC application. Considering its importance, a more detailed description about its properties is briefly given in the following section. Doped ceria is also discussed, considered its structural affinity with YSZ and its employment in the next experimental section.

2.2.1.1 Stabilized Zirconia

Pure zirconia exhibits three polymorphs: monoclinic at room temperature, tetragonal above 1170°C and fluorite cubic above 2370°C (Fig. 2.8). The fluorite structure is a face-centered cubic lattice of cations with anions occupying the tetragonal sites.

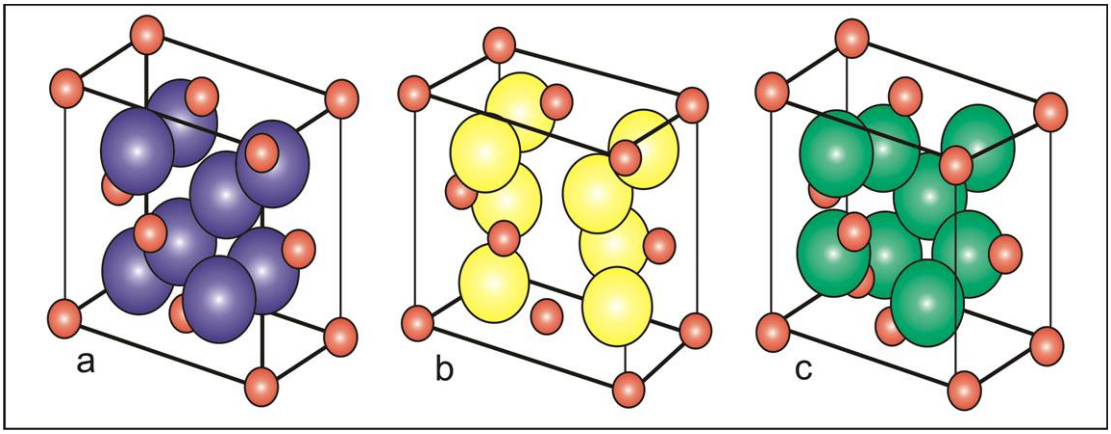

Fig. 2.8 The three polymorphs of zirconia: monoclinic (a), tetragonal (b) and cubic (c).

Due to its high temperature polymorphism, pure zirconia cannot be used at elevated temperatures because of the large volume change (3-5%) which occurs during cooling to the monoclinic phase at about 970°C. This change is sufficient to exceed the elastic and fracture limits, resulting in the failure of the material. However, the tetragonal and cubic phases can be stabilized at room temperature by substitution of the host cation Zr^{4+} with a divalent or trivalent cation of appropriate ionic radius such as Y^{3+}, Yb^{3+}, Er^{3+}, Gd^{3+} and Sc^{3+}. Doping also produces a negative net charge in the crystal and the electroneutrality is achieved by removal of oxygen ions. These oxygen vacancies not only stabilize the structure, but they also create the conduction path for the oxygen ions diffusion. Conductivity of stabilized zirconia depends on the dopant and on its concentration and it has a maximum for each dopant at a specific concentration

as shown in Fig. 2.9. Further increasing the dopant concentration causes a decrease in conductivity because of the electrostatic interaction of vacancies. The relation between the dopant concentration with the highest conductivity and dopant ionic radius is shown in Fig. 2.10. The content of dopant relative to the highest conductivity decreases with increasing radius of dopant ion. Dopants with much larger radius than zirconia have a maximum in conductivity for lower concentration while Sc^{3+}, with the nearest radius to Zr^{4+}, has the highest conductivity for the highest concentration. In fact, doping with ions with larger radius than the host, produces a distortion in the lattice, which negatively affects the diffusion in the lattice and then the conductivity[7]. If doping with an atom with similar size to the host, the substitution yields to a lower elastic strain in the lattice and lower energy is needed to overcome the potential barrier for diffusion and conductivity.

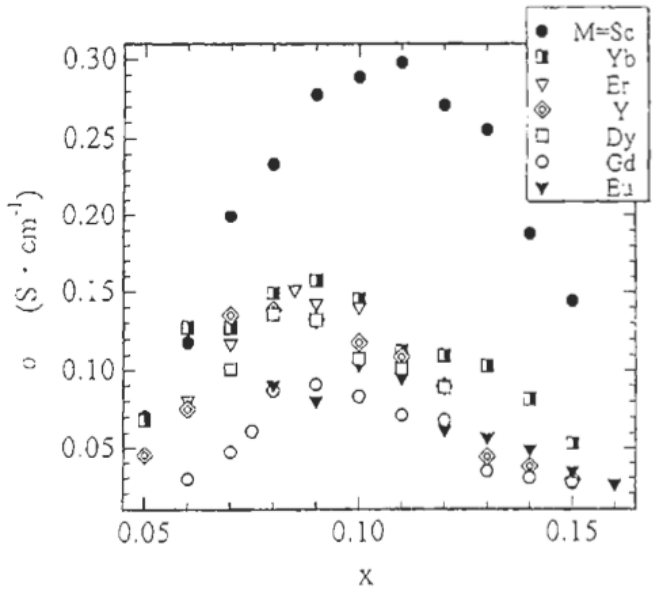

Fig. 2.9 Concentration dependence of the electrical conductivity at 1000°C for the doped zirconia system[4].

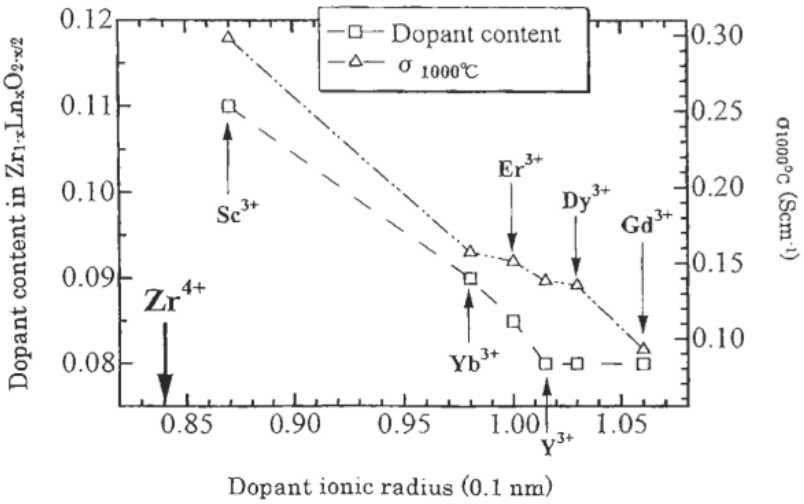

Fig. 2.10 Dopant concentration relative to the highest conductivity as function of its radius in the doped zirconia system[4].

2.2.1.2 Ceria-based electrolytes

Doped ceria is one of the most diffused electrolytes in SOFCs operating at intermediate temperatures[8]. Ceria shares the same cubic fluorite structure of zirconia but unlike it, it is stable from room temperature to the melting point without polymorphs. Pure Ce_2O has a negligible electronic conductivity and free mobile oxygen vacancies are introduced by substitution of Ce^{4+} with divalent or trivalent atoms such as La^{3+}, Y^{3+}, Sm^{3+}, Gd^{3+}, Ca^{2+} and Sr^{2+}. For a fixed doping concentration, the ionic conductivity of doped ceria increases with increasing dopant radius up to a maximum correspondent to Gd^{3+} and Sm^{3+} and then decreases with further increase of ionic radius[9]. Ionic conductivity is also strongly affected by the dopant concentration and has a maximum for a specific concentration for every doping atom. As the concentration is further increased, conductivity decreases as effect of attractive interactions between immobile doping ions and mobile oxygen vacancies[10]. Among all the studied system, 10mol% Gd_2O_3 doped ceria is the one exhibiting the highest conductivity closely followed by 10mol% Sm_2O_3 doped ceria[11,12]. In doped CeO_2, however, the Ce^{4+} ion has the tendency to reduce to Ce^{3+} at low oxygen partial pressure condition, compensating with the creation of a negative charge[13]. This leads to electronic conductivity that short-circuits the cell reducing the open circuit voltage and its efficiency[14]. In Fig. 2.11, the total electrical conductivity is shown as function of the oxygen partial pressure and the temperature. At 800°C, the minimum oxygen partial pressure to have predominant ionic conduction is $\sim 10^{-12}$ atm while in the typical anodic atmosphere it is around 10^{-20} atm. The temperature at which the electronic conduction is larger than the ionic is 600°C and this fixes the maximum temperature of operation for a SOFC using doped ceria as electrolyte.
Another problem related to the reduction of doped ceria at the anode side, is the resulting lattice expansion that can induce the formation of micro cracks and mechanical failure of the electrolyte[15]. Even if the electronic conductivity lowers the OCV, when current is drawn from the cell, the I-V curve turns to be similar to the one of a purely ionic conductor[16]. This happens because the anodic polarization stops the reduction process. The electronic conductivity then, causes a reduction of voltage only for very low current densities and for temperatures higher than 600°C.
Ceria based electrolyte have been used extensively in cells operating at 550°C and lower[17]. If higher temperature of operation is needed, the electronic conductivity can be severely suppressed by doping with other atoms, for example substituting 3mol% out of 20mol% of Gd_2O_3 with praseodymium. This substitution improves the electrolytic domain of the material by nearly two orders of magnitude without significantly affecting the ionic conductivity[18].

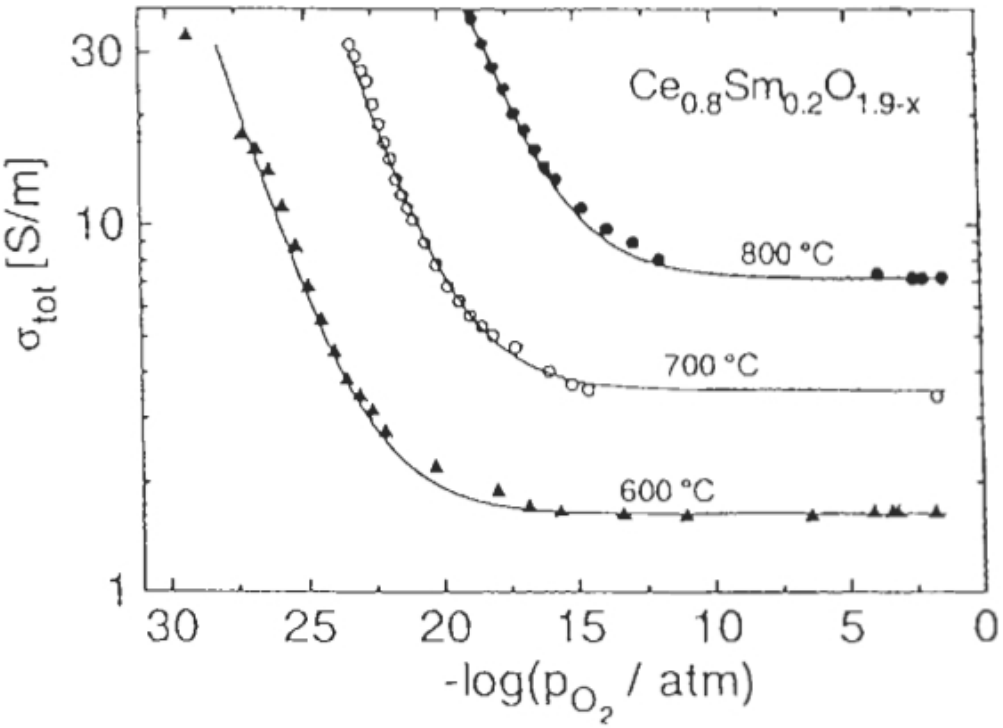

Fig. 2.11 Total electrical conductivity at different temperatures as function of oxygen partial pressure for the $Ce_{0.8}Sm_{0.2}O_{2-\delta}$ system[4].

Another approach to reduce the electronic conductivity is by coating the doped ceria electrolyte with a thin layer of YSZ on the anode side preventing the reduction of the ceria even if the reactivity at the interface could be an issue[19].
One of the most problematic aspects regarding the employment of doped ceria as a solid electrolyte is represented by the high temperatures required sintering it to full density[20]. In fact, sintering temperatures higher than 1500°C are necessary and this may preclude any possibility of co-firing doped ceria with other cell components because of instability or reactivity. In general, decreasing the particles size or doping with small addition of transition metals enhance the sinterability of doped ceria[21]. The decrease of the sintering temperature of doped ceria and the possibility to co-fire it to full density together with low-melting cermet anode, is extensively studied in the experimental section. A more detailed review of the sintering aids and their function is included in the next dedicated chapter*.

* *see Chapter 4*

2.2.2 Anode

The anode is where the electro-oxidation reactions of the fuel take place. In addition to a good catalytic activity for those reactions and resistance to strong reducing environment, other important requirements consist of a sufficient porosity to ease the gas transport to and away from the reaction sites and a high electronic conductivity (typically 100 $S \cdot cm^{-1}$) to ease the movement of electrons to the current collector. The anode is generally made of a cermet: a composite of ionically conductor ceramic material and a metal. The latter is typically introduced in form of oxide to be more resistant to high temperature oxidation and then reduced to its metallic form just before operation to provide the anode with electronic conductivity. The anodic sites where the ionic and electronic conductors meet with the open porosity are where the reactions are believed to take place and it is called triple phase boundary (TPB, Fig. 2.12). An improved distribution and contact of the three phases correspond to a larger TPB and so to a lower anodic overpotential. The most commonly used cermet material is Ni-YSZ due to the exceptional catalytic properties of nickel toward hydrogen oxidation. However, considering the effort in adapting the SOFC to be fed with hydrocarbons, this material encounters many problems and other compositions have been proposed. The following sections contain a brief review of the state of the art anode together with the reasons for its substitution and some details about the specific alternative pursued in the experimental section.

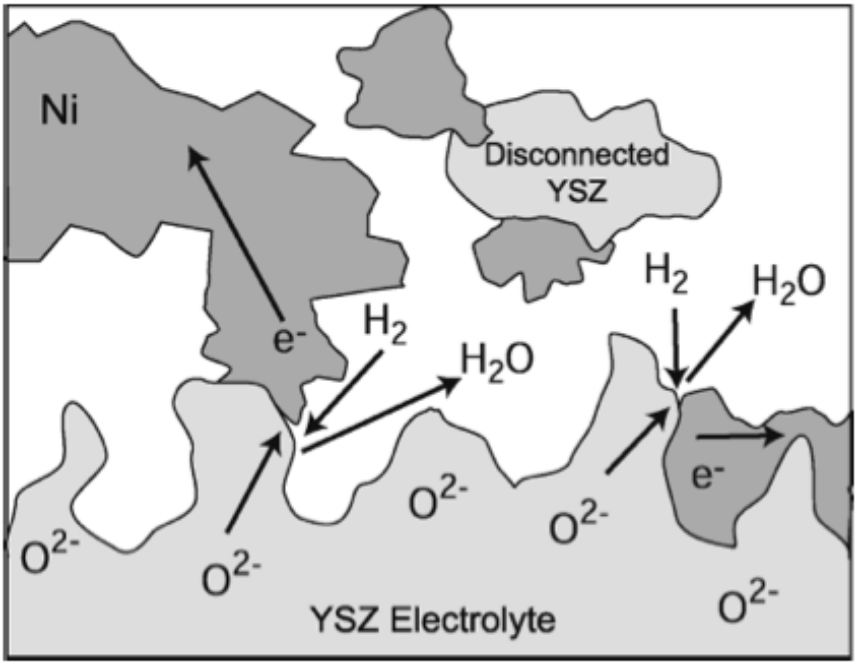

Fig. 2.12 The triple phase boundary in a state-of-the-art Ni-YSZ anode.

2.2.2.1 Ni-YSZ

The Ni-YSZ composite anode is the most common choice for SOFCs mainly because of its low cost, its chemical stability in reducing environment at high temperature, and its absence of interactions between YSZ and Ni[22]. Nickel is an excellent electro catalyst for electrochemical oxidation of hydrogen and methane steam reforming reactions and it is resistant to high temperature. Pure nickel has a melting point of 1453°C and NiO of 1955°C, allowing to process Ni in its oxidized form together with YSZ during sintering and reducing it to metal before operation.

The reduction procedure makes the anode conductive and also creates additional porosity, considering that the specific volume of metallic nickel is significantly smaller than its oxide. The total porosity after reduction depends linearly on the initial porosity contained in the sintered anode, with the factor of proportionality being dependent on the NiO content[23]. Additional porosity in the anode allows increasing the possible paths for fuel and decreasing the concentration polarization but causing a loss in the mechanical properties. If the porosity is large enough to make sure that concentration polarization is not the limiting mechanism, a theoretical analysis showed that the anode performance increases when the microstructure becomes finer because of a larger TPB area[24]. This means that also the ceramic phase of the cermet plays an important electrocatalytic role in the creation of additional reaction sites. The drop observed in the polarization resistance of a cermet anode with fine YSZ particles compared to pure Ni electrode is a further evidence[25]. So the role of YSZ in the anodic cermet is diversified: it allows the broadening of TPB, it ensures the structural resistance to the electrode and it avoids the coarsening and grain growth of Ni particles.

The ceramic phase of the anode also permits to match better matching between the coefficients of thermal expansion (CTE) of the anode and the electrolyte. By small modification of the proportion between NiO ($CTE=14.1\cdot10^{-6}/°C$) and YSZ ($CTE=10.3\cdot10^{-6}/°C$), it is possible to adjust the anode CTE and minimize the mismatch with the electrolyte, conventionally made of YSZ, without severely affecting the conduction properties[26]. However, NiO is also characterized by a peak in its CTE at ~260°C relative to an antiferromagnetic-to-paramagnetic transition[27]. The crystal structure changes during the same transition form rhombohedral to cubic. This anomaly is observed even for a composite containing 10vol% of NiO.

The electronic conductivity of the anode varies with the metal content and shows the characteristic S-shape[28]. It is necessary to have at least 30vol% of Ni to achieve sufficient conductivity[29]. This is in accordance with the percolation theory, which predicts that a third of volume is required to form an interconnected network in case of three co-existing phases. Below the threshold, conductivity is mainly ionic and due to the YSZ because the metallic phase is not

interconnected. The threshold value depends on many variables such as the porosity, pore size, size distribution, and size of raw powders as well as contiguity of each component[30]. Therefore it might also depend on the cermet fabrication technique[31] (Fig. 2.13). As consequence of a decrease in the total porosity and of a narrower pore distribution, the threshold value can be also lowered by increasing the sintering temperature[22] as shown in Fig. 2.14.

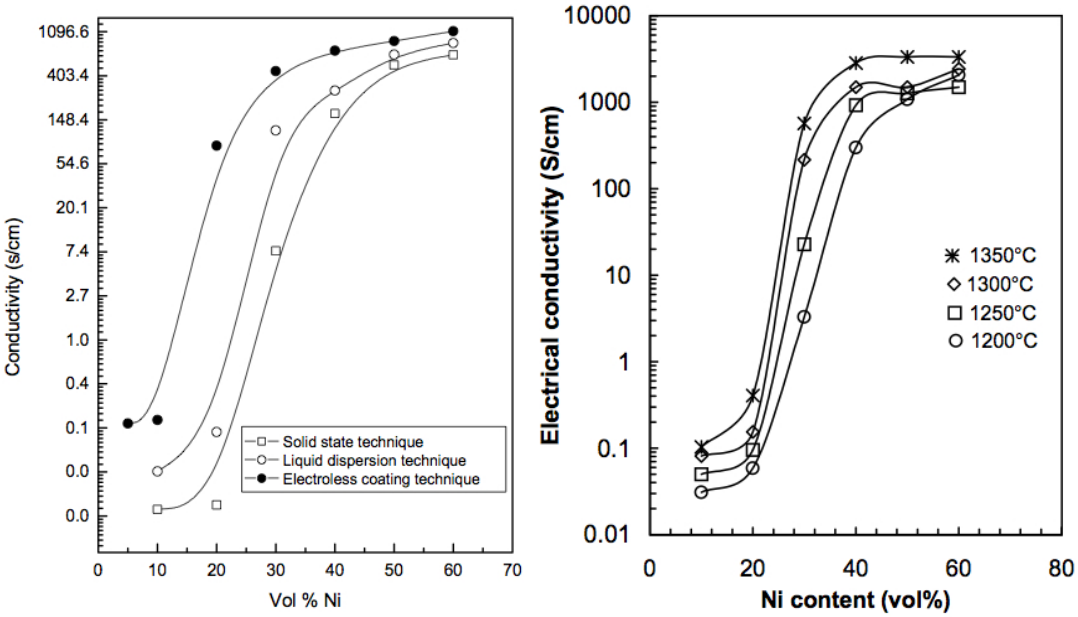

Fig. 2.13 (left) and 2.14 (right). S-shaped conductivity curves as function of the Ni content. Effect of the fabrication technique[31] (left) and the sintering temperature[22] (right).

Although a larger proportion of Ni would be beneficial in reducing the internal electronic resistance of the anode, it leads also to decrease the number of reaction sites along TPB[32]. This primarily affects the activation polarization that has a minimum at approximately 40vol% Ni as showed in Fig. 2.15.

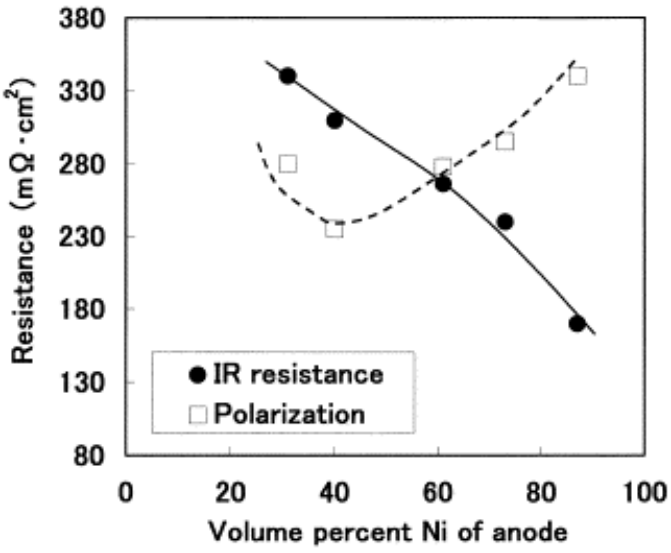

Fig. 2.15 Resistance and polarization of single cells as function of the Ni content in the anode[32].

2.2.2.2 Issues related to the employment of C-based fuels.

Although the state-of-the-art Ni-YSZ anode shows excellent performance and long-term stability for hydrogen, the same is not true when the SOFC is operated with carbon containing fuels. Hydrogen has the highest energy density per mass than any other fuels (Tab. 2.1) but the complete lack of distribution infrastructures and the numerous difficulties relative to its storage, represent serious issues against the real implementation of a hydrogen-based energy economy.

Tab. 2.1 Comparison of some energetic properties of hydrogen and methane.

	H_2	CH_4
Energy density [kWh/kg]	33.3	13.9
Density [g/l]	0.09	0.718
Energy density [kWh/l] *	0.5-2.4	2.6-3.4
Explosion range [vol.%]	4-72.5	5-13.5

Indeed, for hydrogen fuelled SOFCs, water is the only by-product but hydrogen is not available in nature as a single molecule but always bonded to other atoms. It has to be produced by water electrolysis, consuming previously produced energy, or by steam reforming and partial oxidation of naphtha and natural gas, moving the production of carbon monoxide and dioxide more upstream. Using natural gas, methane and other simple hydrocarbons directly in a SOFC, by direct oxidation or internal steam reforming could then constitute a valid, more economic and more ecologic alternative.
When a more complex molecule like methane is used to fuel a SOFC, the simple reaction of hydrogen oxidation is replaced with a more complex set of possible reactions. Similarly to the hydrogen oxidation, the direct oxidation of methane is one of the possible reactions:

$$CH_4+4O^{2-}\rightleftharpoons CO_2+2H_2O+6e^- \qquad (2.32)$$

However, this reaction is highly unlikely to directly occur, even in case of a simple hydrocarbon such as methane. Instead it is more probable to proceed as:

$$CH_4+O^{2-}\rightleftharpoons CH_3OH+2e^- \qquad (2.33)$$

$$CH_3OH+2O^{2-}\rightleftharpoons HCOOH+H_2O+4e^- \qquad (2.34)$$

$$HCOOH+O^{2-}\rightleftharpoons CO_2+H_2O+2e^- \qquad (2.35)$$

Other possible reactions are methane cracking followed by electrochemical oxidation of the cracking products:

$$CH_4 \rightleftharpoons C + 2H_2 \quad (2.36)$$

$$C + 2O^{2-} \rightleftharpoons CO_2 + 4e^- \quad (2.37)$$

$$H_2 + O^{2-} \rightleftharpoons H_2O + 2e^- \quad (2.38)$$

It is also possible that the oxidation might not be completed but proceeds only partially. In this case the reaction of partial oxidation would produce electrons and a mixture of CO and H_2, called syngas:

$$CH_4 + O^{2-} \rightleftharpoons CO + H_2 + 2e^- \quad (2.39)$$

The production of carbon monoxide can also lead to the Boudouard equilibrium reaction or to its electrochemical oxidation:

$$2CO \rightleftharpoons C + CO_2 \quad (2.40)$$

$$CO + O^{2-} \rightleftharpoons CO_2 + 2e^- \quad (2.41)$$

The reactions above, can take place by fuelling the cell only with dry methane and, in principle, no extra steam has to be added. Carbon, produced from reaction (2.36) and (2.40), can be formed in both gas phase or as a solid deposit on anodic surface. The formation of C is often a minor reaction of the overall set, but in the SOFC context is very important especially when it is in the form of solid coke. Depending on the catalytic material used, different types of coke can be formed.

The mechanism of formation starts with the deposition of a carbon source onto the metal surface. The carbon atoms then dissolve in and diffuse through the bulk of the metal particle, although some contribution of surface diffusion cannot be excluded. The final step is the precipitation of the carbon in the form of a nanofibre of graphite at the other side of the metal particle[33] (Fig. 2.16). Nickel in particular is an excellent catalyst for cracking of hydrocarbons and catalyzes this process so efficiently that it is used as catalyst for manufacture of carbon nanofibers[34]. The deposits grow with time, leading to the progressive deactivation of the reaction sites of TPB and, eventually, to the catastrophic failure of the whole cell due to the volume of C deposited.

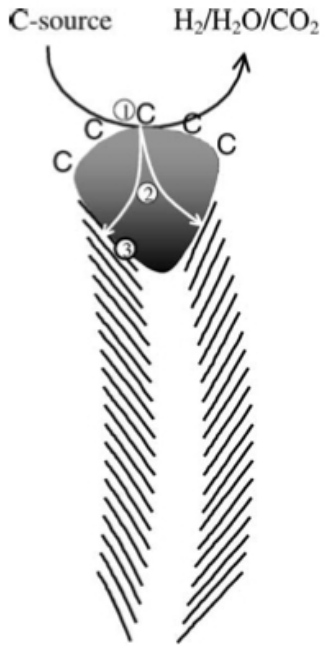

Fig. 2.16 Schematic representation of the catalytic growth of a carbon nanofibre using a gaseous carbon-containing gas. Step 1: decomposition of carbon-containing gases on the metal surface. Step 2: carbon atoms dissolve in and diffuse through the bulk of the metal. Step 3: precipitation of carbon in the form of a nanofibre consisting of graphite[34]*.*

Multiple approaches to avoid this effect are possible: e.g. move away from the thermodynamic conditions that favor the carbon formation, reforming of methane outside or inside the cell or the employment of materials that do not catalyze carbon formation and deposition.

Regarding the first approach, by minimization of the Gibbs free energy of formation of the possible species produced from reaction of dry methane, it is possible to forecast the thermodynamic conditions for which the formation of a specific product is favorable. Of course this is an indication of the possibility of finding that products but not of the kinetic of reaction that depends on other factors like the catalytic activity. However, considering the high temperature reached by a SOFC during operation, kinetics are fast and these predictions are reasonable indicators of the actual reaction products. These theoretical speculations[35] and experimental observations[36] showed that the carbon deposition is strongly related to the supply of oxygen ions through the electrolyte driven by an external current load, and it can be avoided by using high current densities. In Fig. 2.17 the equilibrium diagram shows that the carbon deposition is severe in case of open circuit, with almost all methane converted directly to carbon.

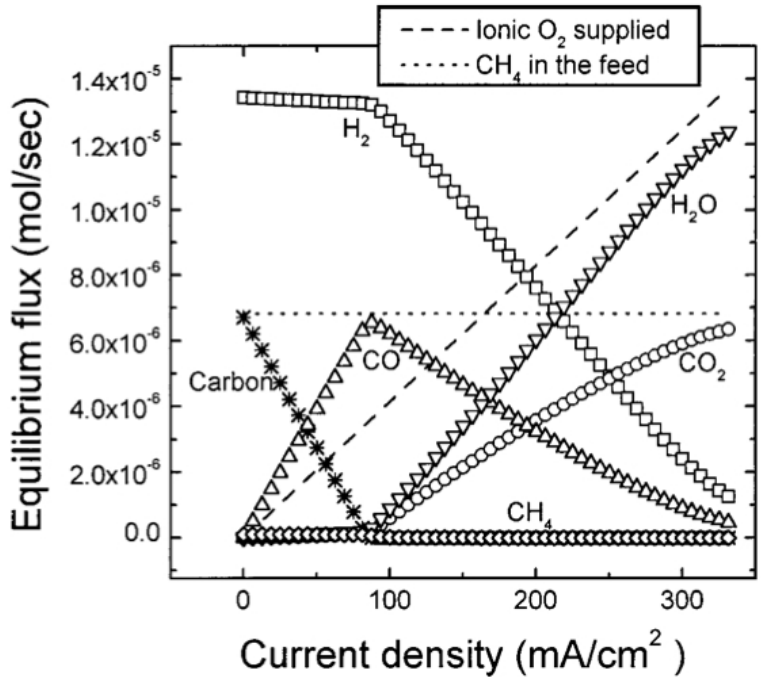

Fig. 2.17 Equilibrium diagram of carbon and gas species as a function of current density for a feed mixture of dry methane[35].

The carbon deposition rate decreases dramatically with increasing current density and stopped once a threshold value is reached. Above this current density value, an abrupt change in concentration of the other species is also observed, sign that the dominant reactions are changed. Without oxygen ions transported through the electrolyte, in open circuit condition, the most favorable reaction is methane cracking (2.36) that produces carbon and H_2 in gas phase. The hydrogen produced doubles in concentration the carbon deposited, as confirmed by the reaction stoichiometry. As the oxygen ions are supplied from the cathode, carbon tends to be oxidized, following reaction (2.37) and moving the equilibrium toward the formation of CO, which increases in concentration. Because this last reaction is considerably fast, the rate limiting reaction in this condition is the methane partial oxidation (2.38). Then, up to the threshold value of current density, the equilibrium behavior is governed by two reaction: for low current densities methane cracking is dominant and contributes to create a significant amount of carbon deposit while increasing the current, partial oxidation becomes dominant (Fig. 2.18). After reaching the threshold value, partial oxidation is favorable to the point that no carbon deposit are formed and syngas is produced. Above the threshold current, the consumption of H_2 and CO and the increase in concentration of CO_2 mean that partial oxidation is progressively hindered compared to the direct methane oxidation (2.32). At the maximum current, the ratio between H_2O and CO_2 is about 1.95, which is close to the stoichiometric ratio between the same by-products from the direct oxidation

reaction. These calculations, which confirm the experimental observations[37,38], show that for currents higher that a threshold, the oxygen ions flux through the electrolyte is large enough to decrease, if not completely avoid, the carbon deposition. However, this effect is limited to the zone of the anode where diffusion of oxygen ions is expected, which was showed to extend for not more few tents of microns from the electrolyte interface[39,40]. Then this approach, although useful to increase the knowledge of the various reactions, is not useful in case of thicker anodes and, in particular, in case of anode supported cells.

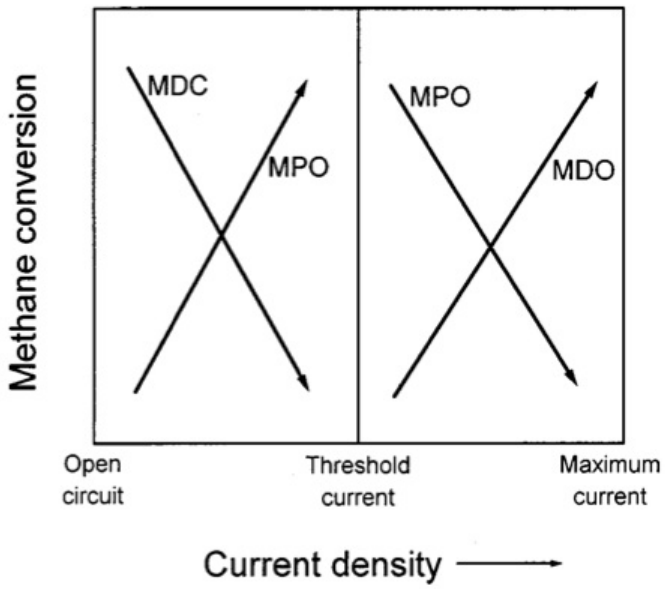

Fig. 2.18. Schematic equilibrium behavior under a low humid condition of the SOFC anode in terms of overall methane reactions: MDC is methane decomposition (2.36), MPO is methane partial oxidation (2.39), and MDO is methane direct oxidation (2.32)[35].

Another approach to solve the problem of carbon deposition on Ni surface consists in introducing steam into the methane flow. The reaction between methane and steam is a well-established industrial process and more than 50% of the worldwide produced hydrogen is generated by steam reforming of hydrocarbons. In the case of SOFC application, it can be performed before entering the cell (external), or directly inside the cell (internal). Steam reforming reaction (2.42) results in the formation of syngas and the CO produced can further react with steam in the water gas shift reaction (2.43) or be oxidized (2.40).

$$CH_4 + H_2O \rightleftharpoons CO + 3H_2 \qquad (2.42)$$

$$CO + H_2O \rightleftharpoons CO_2 + H_2 \qquad (2.43)$$

Fig. 2.19 shows the predicted fuel composition in function of temperature for different steam to methane ratios, based on thermodynamic stability calculation as described in the previous section. It can be appreciated that temperature and the steam content have a strong effect on the formation of carbon[17]. In case of dry operation (S:C=0:1), carbon formation becomes progressively dominant with increasing temperature, while for S:C=2, no carbon is formed for any temperature. For S:C=1, carbon deposition is localized only around 600°C.

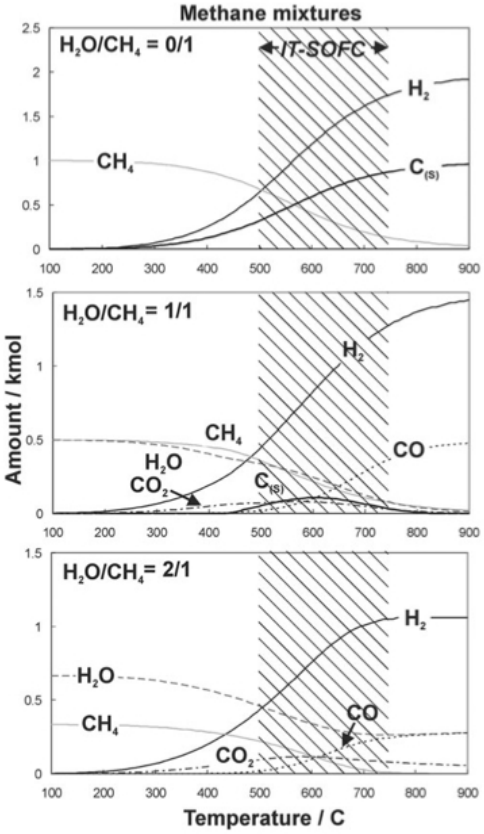

Fig. 2.19 Thermodynamic predictions of the equilibrium composition for methane fed at different temperatures and steam-to-carbon ratios[17].

The stability diagram for the reforming of n-octane fuel as function of temperature and S:C is reported in Fig. 2.20 and shows that the higher is the temperature, the lower is the S:C ratio required to avoid carbon formation[3]. Again, these are thermodynamic stability calculations while kinetics, not considered here, are primarily responsible for stability and strongly depend on the catalytic activity of the material used. In practice on a Ni-YSZ anode, a steam to carbon ratio superior to 3 is required to safely avoid carbon deposition[17]. Diluting the fuel would also increase the oxygen partial pressure of the gas, decreasing the Nerst voltage of the cell and so its efficiency. In addition to this, the reforming reaction (2.42) is strongly endothermic (ΔH=206 kJ/mol) leading to the formation of cold spots and the development of local residual stresses.

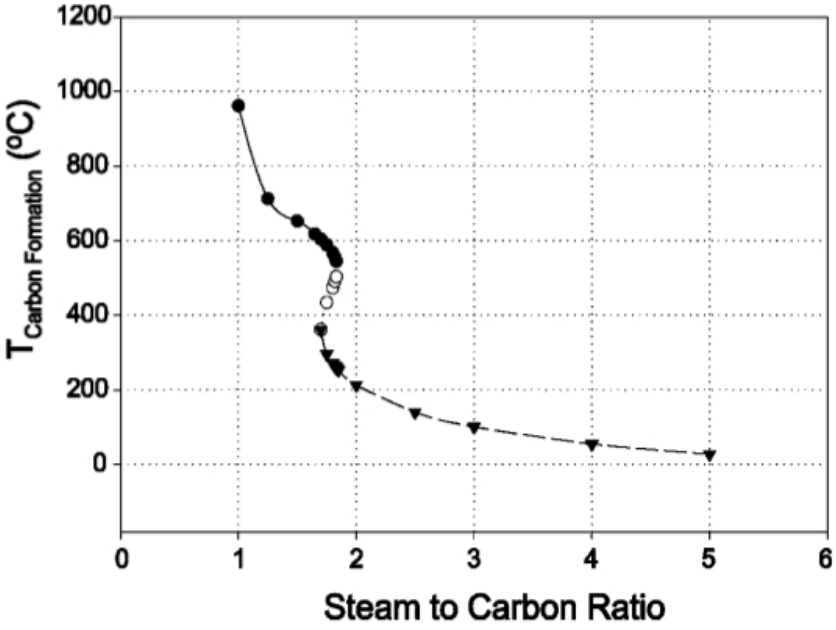

Fig. 2.20 Stability diagram for the formation of carbon as function of the S:C and the operating temperature[3].

A third strategy, and the approach used in this work, consists of using alternative anode materials that do not catalyze carbon formation. Considering that the fuel is methane with steam, the most immediate option would be to substitute partially or completely nickel with another good reforming metal catalyst. Iron and cobalt have been considered as options but unfortunately the same properties that make these metals good reforming catalyst also make them excellent catalyst for the formation of carbon. Even decreasing the catalyst content by partially substituting it with an electronic conductor, like copper, slightly increased the stability period but without resolving the long-term carbon deposition issue[41]. Fig. 2.21 shows photographs of cell anodes containing a Cu-Ni alloy in different proportion after 90min of exposition to dry methane. Even for the 10vol% Ni alloy, deposition is evident and irreversible.

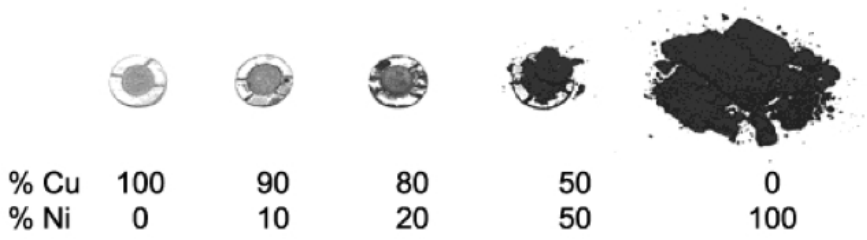

Fig. 2.21 Carbon deposition on Cu-Ni alloys after 90min of exposition to dry methane[41].

Then it might be better to look for a material without strong activity for reforming but only for methane oxidation under low humidity condition. Some ceramic materials show good catalytic activity for the C-H bond cleavage without affinity for carbon deposition, high melting temperature, resistance to redox cycles and mixed electronic-ionic conductivity. In particular, a mixed conductivity means that the TPB area for reaction can be extended to the whole anodic surface. By employing materials with this characteristic, the realization of an all-ceramic anode instead of the conventional cermet can be attainable. The high temperature resistance of these ceramics and the absence of a second phase would ease the fabrication and eliminate eventual problems of metal coarsening or migration during operation. Ceria, particularly when doped with Gd_2O_3 (GDC) or Sm_2O_3, has show potentials for direct operation with hydrocarbons without carbon deposition[42]. The catalytic activity of ceria toward hydrocarbon conversion and carbon oxidation is well-known and ceria based oxides are widely used in application as promoters of the automotive three-way catalyst or as catalyst in self cleaning ovens[43]. Some authors do not agree on the catalytic activity of the stand-alone ceria that has to be improved to achieve sufficient performances by adding precious metals catalyst at dopant level[44]. In general the principal problem with an all GDC or SDC anode is the insufficient electronic conductivity, required to complete the connection with the current collector. Higher electronic conductivity can be obtained in ceramics having perovskites structure ABO_3[45] (Fig. 2.22).

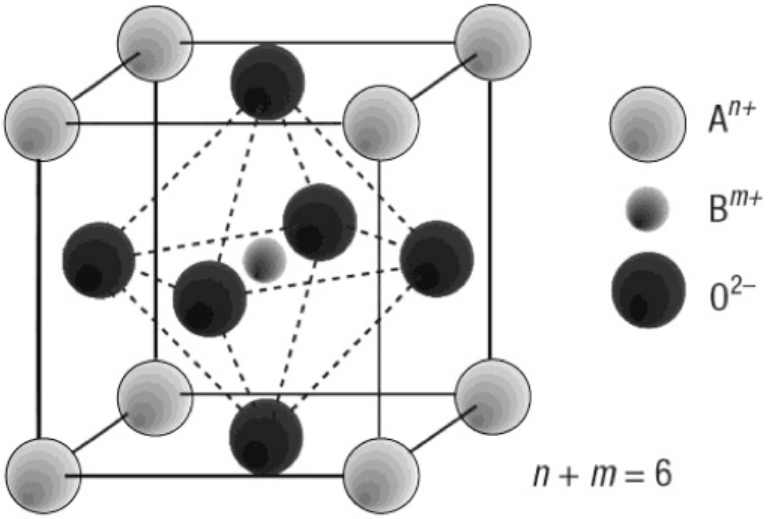

Fig. 2.22 The ideal face centered cubic perovskite lattice.

Many materials used as cathodes belong to this category. Although the requirements for anode and cathode are substantially different, due mostly to the extremes values for oxygen partial pressures to which each is exposed, the perovskites structure has the advantage that it can accommodate a considerable

amount of doping ions that allow the fine tuning of properties like the catalytic activity or the mixed ionic electronic conductivity. Several materials belonging to this category have been proposed such as $La_{0.75}Sr_{0.25}Cr_{0.5}Fe_{0.5}O_3$[46], $La_{0.75}Sr_{0.25}Cr_{0.5}Mn_{0.5}O_3$[47], $La_{0.33}Sr_{0.66}Fe_{0.66}Cr_{0.33}O_3$[48], $La_{0.4}Sr_{0.6}Ti_{1-x}Mn_xO_{3-\delta}$[49] and the double perovskite $Sr_2Mg_{1-x}Mn_xMoO_{6-\delta}$[50]. While much progresses have been made in the study of these materials as potential anodes, they have been hampered by their still insufficient electrochemical activity toward methane oxidation[51], the poor anodic structure and by the still inadequate electronic conductivity[52]. Finally, a number of other mixed oxides that do not have the perovskite structure have also been examined such as yttrium doped $SrTiO_3$[53], niobium titanates with the rutile structure[54], yittria-titania zirconates[55,56]. These too suffer from the similar shortcomings as the perovskite materials.

In summary, a broad variety of materials and combinations have been proposed and tested for SOFC anode application. So far none of these alternatives materials have achieved a comparable electrochemical performance as the Ni-YSZ anode. The insufficient electronic conductivity of the all-ceramic anodes still has to be enhanced by adding a highly conductive second phase. Until the issues in the all ceramic option are resolved, cermet anode can then be considered as the most realistic option. Selecting a highly conductive second phase, the choice is restricted to elements of the groups IB and VIIIB because less noble metal would oxidize too easily in presence of steam. Fe and Co catalyze carbon while Pt, Rh and Pd have also excellent catalytic activity and resistance to cooking but they are too expensive to be feasible. Au and Ag have excellent conductivity but the former is still too expensive while the latter has practical problems due to its low melting point (920°C).

After silver, copper is the most conductive metal existing ($5.96 \cdot 10^5$ $S \cdot cm^{-1}$), is inert toward the C-H bond cleavage and carbon deposition and is also cheap relative to the other metals. It is also safer to work with than carcinogenic NiO. The disadvantages of Cu are mainly related to its low melting temperature (1083°C) and low melting temperature of the oxides. Copper forms two oxides: tenorite (CuO) and cuprite (Cu_2O). Tenorite is the stable oxide in standard condition but it reduces to cuprite by heating above 1026°C and melts incongruently at about 1152°C. Cuprite is unstable in air and tend to form a CuO layer when exposed to humid condition[57]. When heated in low oxygen partial pressure atmosphere, it melts at 1230°C. In Fig. 2.23, the phase stability diagram of copper and its oxides are reported in function of temperature and oxygen partial pressure. The partial pressures of oxygen in air and in high-purity argon are indicated.

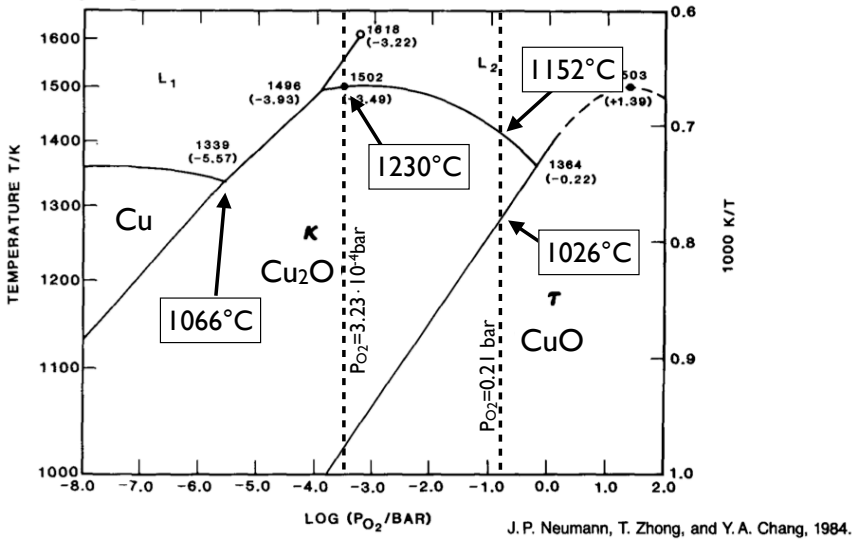

Fig. 2.23 The Cu-O stability diagram[57]. Oxygen partial pressures for air and argon gas used in this study are indicated.

These melting temperatures constitute serious issues for which concern both operation and fabrication. Firstly, high operating temperatures required for sintering would be too close to the Cu metal melting point. This means that for a SOFC with a Cu-based anode, the selection of the electrolyte has to be oriented toward better ionic conductors in intermediate temperature range (500-600°C). Usually GDC or SDC are employed (see section "Electrolytes"). Secondly, the usual procedure of high temperature sintering of the composite cermet with the copper oxide cannot easily be applied in this case. Generally, ceramic and metal oxide are formed and heated up to a temperature that is sufficient to sinter the ceramic phase and create a mechanically stable, well-connected structure. These treatments require much higher temperature than those allowed by copper or its oxides. For lower sintering temperature, it is likely that the ceramic powder of the anode does not become connected, either to itself or to the electrolyte, creating anodes that lose mechanical stability upon reduction of copper oxide to metal[58].

Approaches to solve this incompatibility are mainly based on including the conductive copper in the previously sintered anodic ceramic structure[59]. By using pore formers (like PMMA or graphite), highly porous ceramic scaffolds were realized and repeatedly infiltrated with aqueous solution of copper nitrate. By calcination of the nitrate followed by the reduction of the resulting oxide, a copper metal network is formed inside the porous structure. Another approach based on the same method, to create a finer porosity and increase the mechanical resistance of the anode, Ni of a standard Ni-YSZ anode was leached out using boiling nitric acid[60]. Then the procedure of infiltration was performed. It is claimed that one of the most positive aspects of this methodology consists in

a lower copper content limit for conductivity compared to the percolation limit, because the deposition on the structure surface is not random. Already for 26vol% of Cu, the measured conductivity is about 10^4 S·cm^{-1} (Fig. 2.24).

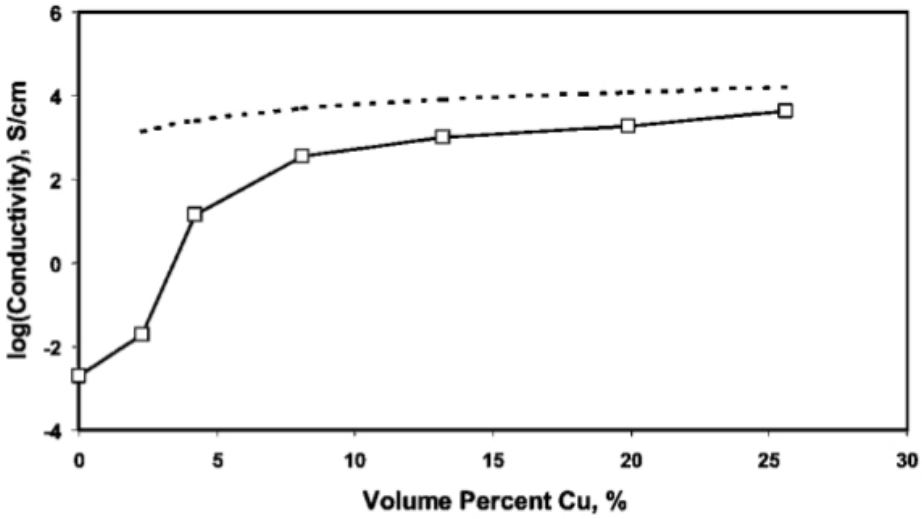

Fig. 2.24 Conductivity of the anode produced by infiltration of copper nitrate in the pre-sintered ceramic scaffold as function of the copper deposited[61].

However, it is undoubtedly a time consuming and wasteful procedure because several infiltration/drying steps are needed to achieve a sufficient deposition of copper. Then, some more doubts about the effective mechanical resistance of such porous structures still hold.

2.2.3 Cathode

The cathode, or air electrode, is where the electrochemical reduction of oxygen occurs. Hence, in order to function properly, the cathode material must fulfill several roles such as reduction of molecular oxygen, transport of ions to the electrolyte interface and distribution of the electrical current associated with the oxygen reduction reaction. Then, in addition to an excellent catalytic activity and an adequate electronic conductivity, the cathodic material must be stable in strongly oxidizing atmosphere and compatible, both chemically and mechanically, with the other cell components. The majority of the materials used for the fabrication of this electrode have perovskite structure. For conventional high-temperature operating cells (800-100°C), the state-of-the-art cathode is usually made of a mixture of lanthanum strontium manganite (LSM) and YSZ. The electronic conductivity of LSM depends strongly on the strontium doping,

increasing linearly up to 50mol% Sr concentration[62]. On the other side, it lacks of ionic conductivity and the addition of an oxide ion conductor, like YSZ, is important for extending the surface of the TPB beyond just the cathode/electrolyte interface. Other cathode materials, more suitable for intermediate operating temperature, are lanthanum strontium cobaltite (LSC) and lanthanum strontium/cobalt ferrite (LSF/LSCF). Compared to LSM, these two are mixed electronic ionic conductors (MIEC) and in principle can be employed as a single-phase cathode. Respect to a composite material, a mixed conductor has the benefit of extending the area of reaction to the whole electrode surface area, resulting in a lower cathode polarization resistance. Appropriate addition of electrolyte materials is usually necessary to obtain a better match of CTEs and avoid cracking and delamination. Usually cobalt-based perovskites display higher ionic and electronic conductivity than any other cathode materials. However, a large amount of cobalt, results in an increased thermal expansion coefficient (>$20 \cdot 10^{-6}$/°C), due to the formation of oxygen vacancies, spin-state transition associated with Co^{3+}, and the relative weak Co-O bond[63]. The large CTE of LSC can be reduced by substituting some Co with Fe. LSCF-type perovskites are generally incompatible with YSZ because of the formation of low conductive compounds negatively affecting the electrochemical performance. Therefore, a protective barrier made of GDC is usually introduced between the two to reduce the undesirable diffusion of atoms[64,65]. Another problem related to the employment of LSCF is the diffusion of strontium out of the structure, which has great influence on the cell degradation during operation[66]. LSF cathode have shown promising performance and optimal stability in the intermediate temperature range[67]. In the iron-based perovskites, both issues of reactivity with YSZ and matching of CTEs are significantly reduced. The thermal expansion coefficient of $La_{0.7}Sr_{0.25}FeO$ closely matches with GDC and this cathode shows no sign of degradation after 500h[68] of operation, identifying it as a very promising cathode for IT-SOFC.

2.3 Architectures and Fabrication Techniques.

The two most common architectures for the fabrication of a SOFC are planar and tubular and both can be designed with different configurations depending on the thicker component that provides them with mechanical support. The possible configurations are classified in self-supported and external-supported cell (Fig. 2.25).

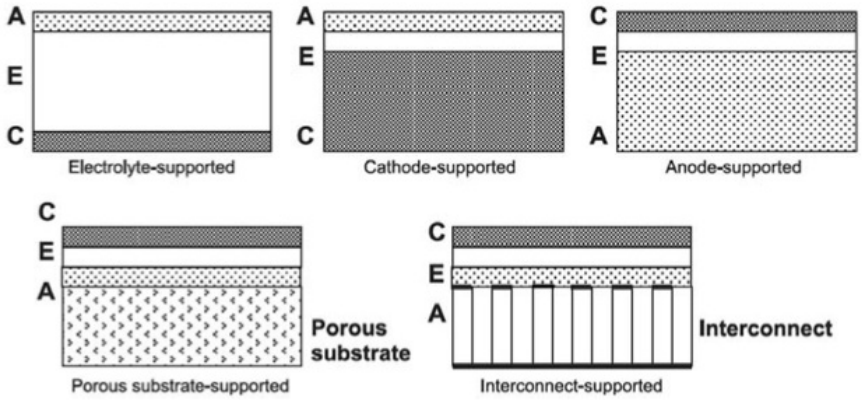

Fig. 2.25 Different fabrication configuration of SOFCs. Self-supported (up) and external-supported (down) cells.

In the case of self-supported cells, one of the functional layers has to provide the mechanical resistance of the whole device. The electrolyte, required to be fully dense, usually has a higher mechanical resistance compared to the electrodes and is often employed as the supporting layer.

The electrolyte-supported configuration is very versatile because it allows firing the electrodes directly on the previously sintered electrolyte, thus leaving considerable options for the electrodes composition and thermal treatments. However the minimum thickness of the electrolyte to mechanically support the cell is relatively high (from 100μm to 1mm) and, although it reduces the problems related to the gas-tightness, it also increases considerably the ionic resistance contribution to the ohmic overpotential and high operating temperatures are thus required.

The anode-supported and cathode-supported configurations are the most commonly used and permit the deposition of very thin electrolyte layers (<50μm). As a result, the operation temperature of the cell can be lowered. The advantages of reduced-temperature operation for the SOFC include a wider choice of materials (especially low-cost metallic materials for the interconnect), longer cell life, reduced thermal stress, improved reliability, and potentially reduced cell cost. In this instance, to reach an optimal densification of the electrolyte, it has to be co-sintered on the supporting electrode, subjecting the

anodic/cathodic materials to the highest temperature of the process. This requires a perfect match of dimensional behavior during heating and cooling, which can be obtained by accurate selection of the materials and their proportions.

In an external-supported cell, the three thin layers are deposited on a thick and robust support without electrochemical activity. The support may also act as current collector. In both cases, it is made by a less expensive material then the other active cell components, reducing the use of expensive ceramics and the overall cost of the cell. Lately, particular attention is being devoted to the fabrication of metal-supported cells[69]. In this configuration the porous metallic support acts also as current collector and it is usually made of Ni or Fe alloys, resistant to reduction and able to creep to accommodate the residual stresses created by dimensional mismatches at high temperature. However, the CTE of the support is usually very different from the CTE of the cell ceramic component and the mismatch is severe especially in the high temperature range, hindering the development of this type of configuration. The metal support can be substituted with electronic conductive ceramics for high temperature operation but the ohmic losses due to the electronic resistance is considerably high. Independently from the configuration, the selection of the cell architecture depends mainly on its end-use and application.

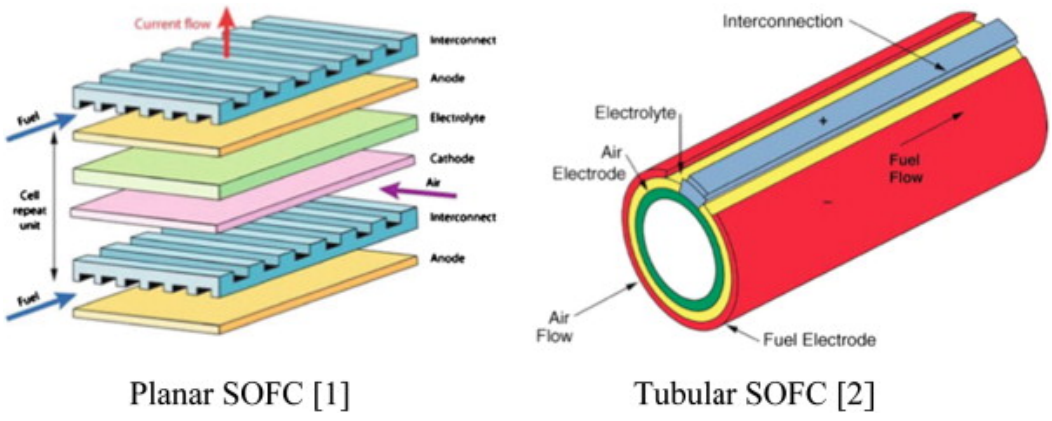

Fig. 2.26 SOFCs most common architectures[4]

Cells with planar architecture are constituted by plane layers stacked on top of the other. They can assume circular shape, fed with fuel from the central axis, or rectangular shape, fed from the edges. Circular cells with small diameters (button cells) are usually fabricated for small scale tests on the performance and durability of the materials used. Rectangular planar cells are produced in larger sizes and are the easiest to stack to obtain high power densities. In the stack, the single cells are separated by a metal interconnect in contact with the same

electrode on both sides. Metal interconnects are employed for temperatures lower than 800°C while for higher temperature application (900-1000°C), ceramic interconnects are used. The interconnects in the stack work also as gas manifold for the fuel and the oxidant (Fig. 2.26). The selection of a particular flow configuration has significant effects on temperature and current distribution within the stack, depending on the precise stack design. Various flow patterns can be implemented in the different flow configurations including Z-flow, serpentine, radial, and spiral patterns. Planar cells benefit from a lower cost of fabrication because cheap techniques can be applied to produce flat ceramic layer. The most commons are tape casting and tape calendering[70]. The planar cell architecture offers high area and volumetric power densities but currently has a number of significant issues such as requiring high-temperature gas seals at the edges of the cell components and between the interconnects and the external gas manifold to isolate oxidant from fuel. Also, although a larger surface area translates into higher currents, some parts of the stack may be subjected to differential heating and cooling rates, decreasing the thermal stability of the system.

In the tubular designs, a cylindrical structure acts as mechanical support for the deposition of the remaining cell layers. As in the planar design, the supporting layer can be constituted by one of the cell components or by a porous support with no electrochemical role. Depending on which electrode is facing the inside of the cell, the fuel or the oxidant flows inside the tube, allowing for a better gas containment and less risk of crossover. One of the most immediate advantages of this architecture compared to the planar is the easier sealing, which however turns to be more of an issue in case of stack design. Also, the tubular structure is more resistant to stresses caused by internal pressures or differential dimensional changes of the layers. For this reason it is the only design can be used in pressurized fuel condition[71], increasing the cell operating voltage and performance. It also allows for shorter start-up and shutdown times and it is more resistant to thermal shock[72].

Several methods such as isostatic pressing, powder pressing and paste extrusion can be used to fabricate the tubular support. Isostatic pressing offers a good pressure distribution and a uniform green density but has a very low output rate. Powder pressing is faster but the product density is likely non-uniform along the tube length. In extrusion, a cohesive plastic material is forced through an orifice of a rigid die to form a shape with constant section, arbitrary length and uniform density. The high extrusion pressure that can be reached during the process permits the formulation of pastes with high solid loading, increasing the strength of the green body and reducing the shrinkages during drying[73]. Additionally this technique is fast and cost effective and is currently the most widely used for realization of the supporting layer. The shortcomings associated with this production technique are mostly related to the optimization of the extrusion process and the extruder itself. The design of the die and the spider to obtain

hollow structures is particularly important to minimize the pressure gradients at the output and avoid warping and rupture of the soft extrudate. Also, the air bubbles formed during the paste preparation step, if not properly eliminated, may affect the integrity of the layer or create defects that can act as stress concentrations during drying or sintering. The other functional layers are deposited on the green or pre-fired support using cheap deposition techniques such as dip-coating[74], spray-coating[75] and brush-painting[76]. More functional layers can be co-extruded at the same time, further shortening the production period but increasing notably the complexity of the extruder design and requiring the unification of the paste rheologies[77,78].

2.4 Performances of SOFCs

At the present moment, the highest power densities recorded for tubular cells running with H_2 are 1.29 W/cm^2 at 600°C, for cells with 1.6mm internal diameter[79,80] and 1.31 W/cm^2 at 550°C, for 1.2mm internal diameter[81,82]. Both cells used thin GDC electrolyte co-sintered on Ni-GDC supporting anode and LSCF-GDC cathode. Although there are other examples of tubular cells employing YSZ instead of GDC and LSM instead of LSCF, there is not any evidence of tubular cells avoiding Ni in the anodic composition (Fig. 2.27).

Indeed, copper has been already employed in SOFC anodes with planar configurations to substitute Ni. However, the low melting temperature of CuO was recognized to be a major limitation during processing and several approaches have been explored to avoid subjecting the copper phase to the high sintering temperatures. The most important and widely published is based on the infiltration of a copper nitrate solution in a pre-sintered scaffold[83]. With this technique, the YSZ ceramic backbone consisting in a porous supporting anode and a dense electrolyte is fired at high temperature. By repeated infiltration followed by calcination, the porous structure is filled with metallic copper until the required loading is reached. Many advantages have been claimed about this approach such as the flexibility of anode composition, the ability of forming a non-random anodic structure, the matching of anode and electrolyte CETs and the conductivity below the 30vol% threshold. The most remarkable results for performance and durability with CH_4 were obtained using this approach. The maximum power density at 800°C for Cu/YSZ anode and 230 um thick YSZ electrolyte was ~40 mW/cm^2 in H_2. By feeding with CH_4 the performance was too poor to be reported because of the lack of catalytic activity of copper toward the methane oxidation. Adding the catalyst CeO_2 to the porous anode, still by

impregnation, led to an improvement of the power densities for both fuels, recording 140 mW/cm^2 in H_2 and 32 mW/cm^2 in CH_4 at 800°C with the same cell architecture. Most importantly, the cell operated for more than 3 days without evidence of carbon deposition[84]. It has to be said, however, that the impregnation is a time-consuming process and the uniformity and quality of the Cu deposit is clearly conditioned by the geometry of the pore network of the anode[85]. Also, the adhesion of the Cu deposit to the YSZ was generally weak and this caused slow deactivation when operated at temperatures above 700°C[86].

A more recent approach consisted in fabricate cathode supported cells. In one study, a tri-layer YSZ structure composed by highly porous thick support, less porous thin interlayer and dense thin film was sintered at high temperature and infiltrated with LSF. Then, a slurry composed by CuO and SDC was applied on top of the electrolyte and sintered at 900°C. The cell exhibited good fuel flexibility, running at 800°C with hydrogen (0.62 W/cm^2), propane (0.40 W/cm^2), dodecane (0.37 W/cm^2) and low sulfur diesel (0.36 W/cm^2) without showing C deposition. However, the infiltration process was claimed to be an issue because of the intensive repetitions and calcination to achieve a sufficient loading of the cathode material, thus making this approach less attractive for commercial application[87].
Another study described the fabrication of a bi-layer composed by a thick LSM-YSZ supporting cathode and YSZ dense electrolyte laminated by tape casting and isostatically pressed to obtain the half-cell. Once sintered at 1275°C, the CuO-YSZ slurry was deposited by screen-printing and fired at 900°C, recording 0.26 W/cm^2 in hydrogen and 0.17 W/cm^2 in propane at 800°C. The performance was slightly increased by substituting YSZ with SDC in the anodic slurry and it reached 0.35 W/cm^2 in hydrogen and 0.22 W/cm^2 in propane, still at 800°C[88].
The cathode-supported configuration allows sintering the copper-containing anode at lower temperature, thus avoiding risk of melting of the conductive phase, but the adhesion with the electrolyte is far from optimal and the thick cathode caused high cathodic polarization resistance.

Finally, a study revealed the possibility of producing an YSZ-Cu cermet by sintering above the Cu melting temperature (1300°C) in reducing atmosphere. The molten metal was stated to wet the YSZ and produce a well-connected and fine structure with excellent conductivity. The power density was 0.27 W/cm^2 and the OCV above 1 V[89]. It is not clear though, how the high temperature treatment did not produce the leaking of the molten metal out from the structure or, at least, its migration.

Any examples of copper cermet anode-supported tubular cell have never been recorded in literature[90] (Fig. 2.27).

Year	Support design	Support fabrication technique	Anode	Electrolyte	Cathode	Cell diameter (mm)	Fuel stream	Temp. (°C)	OCV (V)	Max. power density (W cm^{-2})
2006	Anode-supported	Plastic mass ram extrusion	Ni–CGO	CGO	LSCF–CGO	1.60	Humidified H_2–N_2	570	0.84	0.35
2006	Anode-supported	Plastic mass ram extrusion	Ni–CGO	CGO	LSCF–CGO	0.80	Humidified H_2–N_2	550	0.85	0.35
2007	Anode-supported	Plastic mass ram extrusion	Ni–CGO	CGO	LSCF–CGO	1.48	Humidified H_2–N_2	550	0.78	0.4
2007	Anode-supported	Plastic mass ram extrusion	Ni–ScSZ	ScSZ	LSCF–CGO–Ag	1.80	Humidified H_2–Argon	650	1.06	1.06
2007	Cathode-supported	Plastic mass ram extrusion	Ni–CGO	CGO	LSCF–CGO	2.26	Humidified H_2–Argon	600	0.70	0.16
2008	Cathode-supported	Plastic mass ram extrusion	Ni–CGO	ScSZ	LSM	1.60	Humidified H_2	800	>1.0	0.31
2008	Anode-supported	Supplied by Adaptive Materials Inc. USA	Ni–YSZ	YSZ	LSM–YSZ	2.55	CH_4–air (single chamber)	750	NA	0.6 (at 0.5 V)
2008	Cathode-supported	Plastic mass ram extrusion	Ni–CGO	ScSZ	LSM–CGO	1.63	Humidified H_2	750	1.06	0.45
2008	Anode-supported	Plastic mass ram extrusion	Ni–CGO	CGO	LSCF–CGO	0.40	Humidified H_2	550	0.76	0.3
2009	Anode-supported	Plastic mass ram extrusion	Ni–CGO	CGO	LSCF–CGO	0.80	Humidified H_2	600	0.80	1.29
2009	Anode-supported	Supplied by Adaptive Materials Inc. USA	Ni–YSZ	YSZ	LSM	2.00	CH_4 (single chamber)	750	1.05	0.12
2009	Anode-supported	Plastic mass ram extrusion	Ni–CGO	CGO	LSCF–CGO	1.80	Humidified H_2	450	0.90	0.3
2009	Anode-supported	Cold isostatic pressing	Ni–YSZ	YSZ	LSM–YSZ	2.90	Humidified H_2	850	1.05	0.65
2010	Anode-supported	Plastic mass ram extrusion	Ni–CGO	CGO	LSCF–CGO	1.60	Humidified H_2	550	0.83	1.31
2010	Anode-supported	Supplied by Adaptive Materials Inc. USA	Ni–YSZ	YSZ	LSM	2.00	CH_4 (single chamber)	750	0.92	0.036
2010	Anode-supported	Plastic mass ram extrusion	Ni–YSZ	YSZ	LSCF–CGO	1.70	Humidified H_2	600	1.00	0.39
2011	Anode-supported	Cold isostatic pressing	Ni–CGO	CGO	LSCF–CGO	3.00	Pure H_2	450	0.78	0.066
2011	Anode-supported	Plastic mass ram extrusion	Ni–CGO	CGO	LSCF–CGO	1.80	Humidified CO–H_2	550	0.76	0.63
2011	Anode-supported	Supplied by Adaptive Materials Inc. USA	Ni–YSZ	YSZ	LSCF–CGO	2.00	CH_4 (single chamber)	700	1.20	0.12
2011	Anode-supported	NA	Ni–CGO	CGO	LSCF–CGO	1.80	Humidified H_2	550	0.93	0.34 (at 0.7 V)
2011	Anode-supported	Plastic mass ram extrusion	Ni–YSZ	ScSZ–CGO	LSCF–CGO	NA	Pure H_2	700	1.08	0.57
2012	Anode-supported	Plastic mass ram extrusion	Ni–YSZ	CGO	LSCF	1.80	NA	NA	NA	NA
2012	Anode-supported	Plastic mass ram extrusion	Ni–YSZ	YSZ–CGO	LSCF–CGO	1.80	Humidified H_2–N_2	650	0.4	0.73
2013	Anode-supported	Plastic mass ram extrusion	Ni–CGO	CGO	LSCF–CGO	2.00	Diluted H_2	542	>0.9	0.6
2013	Anode-supported	Plastic mass ram extrusion	Ni–YSZ	YSZ–CGO	LSCF–CGO	1.8	Humidified H_2–N_2	697	0.4	1.2

Fig. 2.27 Recent development of single tubular SOFCs using conventional extrusion[90]

References

1. Nernst, W. Zur Theorie der elektrischen Reizung. *Nachrichten von der Gesellschaft der Wissenschaften …* (1899).
2. Baur, E. & Preis, H. Brennstoff-Ketten mit Festleitern. *Zeitschrift für Elektrochemie und angewandte …* (1938).
3. DoE, U. *Fuel cell handbook*. (EG&G Services Inc.: 2000).
4. Singhal, S. *High temperature solid oxide fuel cells: fundamentals, design, and applications*. (2003).
5. Subbarao, E. Solid electrolytes with oxygen ion conduction. *Solid State Ionics* (1984).
6. Yamamoto, O. Solid oxide fuel cells: fundamental aspects and prospects. *Electrochimica Acta* (2000).
7. Wang, D., PARK, D., GRIFFITH, J. & NOWICK, A. Oxygen-Ion Conductivity and Defect Interactions in Yttria-Doped Ceria. *Solid State Ionics* **2**, 95–105 (1981).
8. Tuller, H. Doped ceria as a solid oxide electrolyte. *J Electrochem Soc* (1975).
9. Minh, N. *Science and technology of ceramic fuel cells*. (1995).
10. Kilner, J. The effects of dopant cation-oxygen vacancy complexes on the anion transport properties of non-stoichiometric fluorite oxides. *Solid State Ionics* (1982).
11. Gerhardt-Anderson, R. Ionic conductivity of CeO2 with trivalent dopants of different ionic radii. *Solid State Ionics* (1981).
12. Kuharuangrong, S. Ionic conductivity of Sm, Gd, Dy and Er-doped ceria. *Journal of Power Sources* (2007).
13. Atkinson, A., Baron, S. & Brandon, N. AC impedance spectra arising from mixed ionic electronic solid electrolytes. *J Electrochem Soc* **151**, E186–E193 (2004).
14. Ramesh, S. & Reddy, C. V. Electrical properties of co-doped Ce0. 8− xGd0. 2SrxO2− δ electrolyte. *Acta Physica Polonica A* **115**, 909–913 (2009).
15. Inaba, H. Ceria-based solid electrolytes. *Solid State Ionics* (1996).
16. Kharton, V., Marques, F. & Atkinson, A. Transport properties of solid oxide electrolyte ceramics: a brief review. *Solid State Ionics* **174**, 135–149 (2004).
17. Brett, D. J. L., Atkinson, A., Brandon, N. P. & Skinner, S. J. Intermediate temperature solid oxide fuel cells. *Chem. Soc. Rev.* **37**, 1568 (2008).
18. Maricle, D., Swarr, T. & Karavolis, S. Enhanced ceria—a low-temperature SOFC electrolyte. *Solid State Ionics* (1992).
19. Ji, S. *et al.* Fabrication of low-temperature solid oxide fuel cells with a nanothin protective layer by atomic layer deposition. *Nanoscale research Letters* (2013).
20. Inaba, H., Nakajima, T. & Tagawa, H. Sintering behaviors of ceria and gadolinia-doped ceria. *Solid State Ionics* **106**, 263–268 (1998).
21. NICHOLAS, J. & DEJONGHE, L. Prediction and evaluation of sintering aids for Cerium Gadolinium Oxide. *Solid State Ionics* **178**, 1187–1194 (2007).
22. Zhu, W. Z. & Deevi, S. C. A review on the status of anode materials for solid oxide fuel cells. *Materials Science and Engineering: A* **362**, 228–239 (2003).
23. Radovic, M. & Lara-Curzio, E. Mechanical properties of tape cast nickel-

based anode materials for solid oxide fuel cells before and after reduction in hydrogen. *Acta Materialia* **52**, 5747–5756 (2004).
24. Tanner, C. W., Fung, K.-Z. & Virkar, A. V. The effect of porous composite electrode structure on solid oxide fuel cell performance I. Theoretical analysis. *J Electrochem Soc* **144**, 21–30 (1997).
25. De Boer, B., Gonzalez, M., Bouwmeester, H. & Verweij, H. The effect of the presence of fine YSZ particles on the performance of porous nickel electrodes. *Solid State Ionics* **127**, 269–276 (2000).
26. Mori, M., Yamamoto, T., Itoh, H., Inaba, H. & Tagawa, H. Thermal Expansion of Nickel-Zirconia Anodes in Solid Oxide Fuel Cells during Fabrication and Operation. *J Electrochem Soc* **145**, 1374–1381 (1998).
27. Nkosi, S. S. *et al.* Antiferromagnetic–paramagnetic state transition of NiO synthesized by pulsed laser deposition. *Applied Surface Science* **265**, 860–864
28. He, C., Chen, T. & Wang, W. G. The mechanical and electrical properties of Ni/YSZ anode support for solid oxide fuel cells. (2006).
29. Dees, D., Claar, T. D., Easler, T., Fee, D. & Mrazek, F. Conductivity of Porous Ni/ZrO2-Y 2 O 3 Cermets. *J Electrochem Soc* **134**, 2141–2146 (1987).
30. Itoh, H. *et al.* Configurational and electrical behavior of Ni-YSZ cermet with novel microstructure for solid oxide fuel cell anodes. *J Electrochem Soc* **144**, 641–646 (1997).
31. Pratihar, S. K., Dassharma, A. & Maiti, H. S. Processing microstructure property correlation of porous Ni–YSZ cermets anode for SOFC application. *Materials research bulletin* **40**, 1936–1944 (2005).
32. Koide, H., Someya, Y., Yoshida, T. & Maruyama, T. Properties of Ni/YSZ cermet as anode for SOFC. *Solid State Ionics* **132**, 253–260 (2000).
33. Finnerty, C., Coe, N., Cunningham, R. & Ormerod, R. Carbon formation on and deactivation of nickel-based/zirconia anodes in solid oxide fuel cells running on methane. *Catal Today* **46**, 137–145 (1998).
34. Toebes, M. L., Bitter, J. H., Van Dillen, A. J. & de Jong, K. P. Impact of the structure and reactivity of nickel particles on the catalytic growth of carbon nanofibers. *Catalysis today* **76**, 33–42 (2002).
35. Koh, J.-H., Kang, B.-S., Lim, H. C. & Yoo, Y.-S. Thermodynamic Analysis of Carbon Deposition and Electrochemical Oxidation of Methane for SOFC Anodes. *Electrochem Solid St* **4**, A12 (2001).
36. Horita, T., Sakai, N., Kawada, T., Yokokawa, H. & Dokiya, M. Oxidation and steam reforming of CH 4 on Ni and Fe anodes under low humidity conditions in solid oxide fuel cells. *J Electrochem Soc* **143**, 1161–1168 (1996).
37. Ihara, M., Abudula, A., Komiyama, H. & Yamada, K. Anodic reaction mechanism determining the threshold current density for the CO2 production in SOFC with dry methane fuel. *Proc. of 2nd European Solid Oxide Fuel Cell Forum* 637–646 (1996).
38. Abudula, A., Ihara, M. & Komiyama, H. Direct Oxidation of Methane on Anode of Solid Oxide Fuel Cell. *Proc. of 4nd European Solid Oxide Fuel Cell Forum* (1995).
39. Zhu, W., Ding, D. & Xia, C. Enhancement in three-phase boundary of SOFC electrodes by an ion impregnation method: a modeling comparison. *Electrochem Solid St* (2008).

40. Janardhanan, V. & Heuveline, V. Three-phase boundary length in solid-oxide fuel cells: A mathematical model. *Journal of Power Sources* (2008).
41. KIM, H., LU, C., Worrell, W., Vohs, J. & Gorte, R. Cu-Ni cermet anodes for direct oxidation of methane in solid-oxide fuel cells. *J Electrochem Soc* **149**, A247–A250 (2002).
42. Steele, B. C. H., Middleton, P. H. & Rudkin, R. A. Material science aspects of SOFC technology with special reference to anode development. *Solid State Ionics* **40–41, Part 1**, 388–393
43. MOGENSEN, M. & Sammes, N. Physical, chemical and electrochemical properties of pure and doped ceria. *Solid State Ionics* (2000).
44. Marina, O., Bagger, C., Primdahl, S. & MOGENSEN, M. A solid oxide fuel cell with a gadolinia-doped ceria anode: preparation and performance. *Solid State Ionics* **123**, 199–208 (1999).
45. Ishihara, T. *Perovskite oxide for solid oxide fuel cells*. (2009).
46. Tao & Irvine, J. T. S. Catalytic Properties of the Perovskite Oxide La 0.75Sr 0.25Cr 0.5Fe 0.5O 3-δin Relation to Its Potential as a Solid Oxide Fuel Cell Anode Material. *Chem. Mater.* **16**, 4116–4121 (2004).
47. Peña-Martínez, J. *et al.* Anodic Performance and Intermediate Temperature Fuel Cell Testing of La 0.75Sr 0.25Cr 0.5Mn 0.5O 3-δat Lanthanum Gallate Electrolytes. *Chem. Mater.* **18**, 1001–1006 (2006).
48. Haag, J. M., Madsen, B. D., Barnett, S. A. & Poeppelmeier, K. R. Application of LaSr[sub 2]Fe[sub 2]CrO[sub 9−δ] in Solid Oxide Fuel Cell Anodes. *Electrochem Solid St* **11**, B51 (2008).
49. Fu, Q., Tietz, F. & Stöver, D. La0. 4Sr0. 6Ti1− x Mn x O3− δ Perovskites as Anode Materials for Solid Oxide Fuel Cells. *J Electrochem Soc* (2006).
50. Huang, Y.-H., Dass, R. I., Denyszyn, J. C. & Goodenough, J. B. Synthesis and Characterization of Sr[sub 2]MgMoO[sub 6−δ]. *J Electrochem Soc* **153**, A1266 (2006).
51. Alifanti, M. *et al.* Activity in methane combustion and sensitivity to sulfur poisoning of La 1− x Ce x Mn 1− y Co y O 3 perovskite oxides. *Applied Catalysis B: Environmental* **41**, 71–81 (2003).
52. Marina, O., Canfield, N. & Stevenson, J. Thermal, electrical, and electrocatalytical properties of lanthanum-doped strontium titanate. *Solid State Ionics* (2002).
53. Hui, S. & Petric, A. Evaluation of yttrium-doped SrTiO 3 as an anode for solid oxide fuel cells. *Journal of the European Ceramic Society* (2002).
54. Reich, C., Kaiser, A. & Irvine, J. Niobia based rutile materials as SOFC anodes. *Fuel Cells* (2001).
55. Kelaidopoulou, A., Siddle, A., Dicks, A. & Kaiser, A. Anodic Behaviour of Y0. 20Ti0. 18 Zr0. 62O1. 90 Towards Hydrogen Electro-Oxidation in a High Temperature Solid Oxide Fuel Cell. *Fuel* (2001).
56. Kelaidopoulou, A., Siddle, A., Dicks, A. & Kaiser, A. Methane Electro-Oxidation on a Y0. 20Ti0. 18Zr0. 62O1. 90 Anode in a High Temperature Solid Oxide Fuel Cell. *Fuel* (2001).
57. Neumann, J., Zhong, T. & Chang, Y. The Cu− O (Copper-Oxygen) system. *Journal of Phase Equilibria* **5**, 136–140 (1984).
58. Kiratzis, N. E., Connor, P. & Irvine, J. T. S. Preparation and characterization of copper based cermet anodes for use in solid oxide fuel cells at intermediate temperatures. *J Electroceram* **24**, 270–287 (2010).

59. Vohs, J. M. & Gorte, R. J. High-Performance SOFC Cathodes Prepared by Infiltration. *Adv. Mater.* **21**, 943–956 (2009).
60. Kim, H., Rosa, C., Boaro, M., Vohs, J. M. & Gorte, R. J. Fabrication of Highly Porous Yttria-Stabilized Zirconia by Acid Leaching Nickel from a Nickel-Yttria-Stabilized Zirconia Cermet. *J Am Ceram Soc* **85**, 1473–1476 (2002).
61. McIntosh, S. Direct hydrocarbon solid oxide fuel cells. *Chem. Rev.* (2004).
62. Sun, C., Hui, R. & Roller, J. Cathode materials for solid oxide fuel cells: a review. *J Solid State Electrochem* **14**, 1125–1144 (2010).
63. Huang, K. Sr- and Ni-Doped LaCoO[sub 3] and LaFeO[sub 3] Perovskites. *J Electrochem Soc* **145**, 3220 (1998).
64. Assenmacher, W., Uhlenbruck, S. & Haanappel, V. Ce 0.8 Gd 0.2 O 2− δ protecting layers manufactured by physical vapor deposition for IT-SOFC. *Solid State Ionics* (2008).
65. Jordan, N., Sebold, D., Buchkremer, H. & Haanappel, V. Thin film coating technologies of (Ce, Gd) O 2-δ interlayers for application in ceramic high-temperature fuel cells. *Thin Solid Films* (2007).
66. Mai, A., HAANAPPEL, V., Uhlenbruck, S., Tietz, F. & Stöver, D. Ferrite-based perovskites as cathode materials for anode-supported solid oxide fuel cells☆Part I. Variation of composition. *Solid State Ionics* **176**, 1341–1350 (2005).
67. Wang, W., Huang, Y., Jung, S., Vohs, J. M. & Gorte, R. J. A comparison of LSM, LSF, and LSCo for solid oxide electrolyzer anodes. *J Electrochem Soc* **153**, A2066–A2070 (2006).
68. Janardhanan, V. M., Heuveline, V. & Deutschmann, O. Performance analysis of a SOFC under direct internal reforming conditions. *Journal of Power Sources* **172**, 296–307 (2007).
69. Brandon, N. P. *et al.* Development of Metal Supported Solid Oxide Fuel Cells for Operation at 500-600 °C. *Journal of Materials Engineering and Performance* **13**, 253–256 (2004).
70. Mistler, R. E. & Twiname, E. R. *Tape Casting: theory and practice*. (The American Ceramic Society: 2000).
71. Hashimoto, S. *et al.* Power Generation Properties of Microtubular Solid Oxide Fuel Cell Bundle Under Pressurized Conditions. *J Fuel Cell Sci Tech* **8**, – (2011).
72. Howe, K. S., Thompson, G. J. & Kendall, K. Micro-tubular solid oxide fuel cells and stacks. *Journal of Power Sources* **196**, 1677–1686 (2011).
73. Händle, F. *Extrusion in ceramics*. (2007).
74. Hsieh, W.-S., Lin, P. & Wang, S.-F. Fabrication of electrolyte supported micro-tubular SOFCs using extrusion and dip-coating. *Int J Hydrogen Energ* **38**, 2859–2867 (2013).
75. Ding, J., Liu, J., Yuan, W. & Zhang, Y. Slip casting combined with colloidal spray coating in fabrication of tubular anode-supported solid oxide fuel cells. *Journal of the European Ceramic Society* **28**, 3113–3117 (2008).
76. Soderberg, J. N., Sun, L., Sarkar, P. & Birss, V. I. Oxygen Reduction at LSM–YSZ Cathodes Deposited on Anode-Supported Microtubular Solid Oxide Fuel Cells. *J Electrochem Soc* **156**, B721 (2009).
77. POWELL, J. The unification of paste rheologies for the co-extrusion of solid oxide fuel cells. *Journal of the European Ceramic Society* (2009).
78. POWELL, J. Co-extrusion of multilayered ceramic micro-tubes for use as

solid oxide fuel cells. *Journal of the European Ceramic Society* (2010).
79. Suzuki, T., Yamaguchi, T., Fujishiro, Y. & Awano, M. Fabrication and characterization of micro tubular SOFCs for operation in the intermediate temperature. *Journal of Power Sources* **160**, 73–77 (2006).
80. Suzuki, T., Funahashi, Y., Yamaguchi, T., Fujishiro, Y. & Awano, M. Design and fabrication of lightweight, submillimeter tubular solid oxide fuel cells. *Electrochem Solid St* **10**, A177–A179 (2007).
81. Sin, Y.-W. *et al.* The properties and performance of micro-tubular (less than 2.0 mm OD) anode suported solid oxide fuel cell (SOFC). *Int J Hydrogen Energ* **36**, 1882–1889 (2011).
82. Calise, F., Restucccia, G. & Sammes, N. Experimental analysis of performance degradation of micro-tubular solid oxide fuel cells fed by different fuel mixtures. *Journal of Power Sources* **196**, 301–312 (2011).
83. Gross, M. D., Vohs, J. M. & Gorte, R. J. Recent progress in SOFC anodes for direct utilization of hydrocarbons. *Journal of Materials Chemistry* **17**, 3071–3077 (2007).
84. Park, S., Vohs, J. & Gorte, R. Direct oxidation of hydrocarbons in a solid-oxide fuel cell. *Nature* **404**, 265–267 (2000).
85. Jung, S. *et al.* Influence of composition and Cu impregnation method on the performance of Cu/CeO2/YSZ SOFC anodes. *Journal of Power Sources* **154**, 42–50 (2006).
86. Gorte, R. J. & Vohs, J. M. Nanostructured anodes for solid oxide fuel cells. *Curr Opin Colloid in* **14**, 236–244 (2009).
87. Zhao, L., Ye, X. & Zhan, Z. High-performance cathode-supported solid oxide fuel cells with copper cermet anodes. *Journal of Power Sources* **196**, 6201–6204 (2011).
88. Zhan, Z. & Lee, S. I. Thin film solid oxide fuel cells with copper cermet anodes. *Journal of Power Sources* **195**, 3494–3497 (2010).
89. Tucker, M. C., Lau, G. Y., Jacobson, C. P., Visco, S. J. & De Jonghe, L. C. Cu–YSZ cermet solid oxide fuel cell anode prepared by high-temperature sintering. *Journal of Power Sources* **195**, 3119–3123 (2010).
90. Jamil, S. M. *et al.* Recent fabrication techniques for micro-tubular solid oxide fuel cell support: A review. *Journal of the European Ceramic Society* **35**, 1–22 (2015).

3. Study and optimization of the extrusion process for ceramic pastes*

Abstract

Gadolinia-doped ceria ceramic pastes were formulated with different solid loadings and extruded using lab scale equipment. The force to maintain a constant ram speed of 10 mm/min was recorded. The radial shrinkage after drying was proportional to the solid loading and this allowed the determination of the maximum solid loading by an extrapolation procedure. In order to obtain the apparent viscosity of the pastes, a novel approach based on the analysis of the slope of the extrusion pressure plot versus the distance covered by the ram was formulated for the direct determination of the shear stress upon extrusion. The agreement of the determined maximum solid loading with values calculated by two existing models confirms that the proposed approach is an alternative and reliable method to identify the upper limit of the solid loading range for the formulation of extrudable ceramic pastes.

Keywords: Ceramic Extrusion; Maximum solid loading; Drying shrinkage; Rheology.

3.1 Introduction

Extrusion is a fast and reliable forming technique for the fabrication of long objects with constant cross section. It allows for high production rates while maintaining dimensional accuracy and an optimal surface finish[1-4]. Though extrusion has mostly been developed for polymeric and metallic materials, it has also found numerous applications for technical ceramic products. It is currently used in the ceramic industry for the manufacturing of different shapes ranging from the very simple, such as clay bricks, to very complicated articles, such as ceramic honeycomb matrices used in a car exhaust system to control and limit pollutants emissions. Nevertheless, the process of ceramic extrusion still lacks of a systematic operating knowledge and the literature regarding this field is relatively scarce.

An extrusion paste is generally composed of a solid and a liquid phase. For the extrusion of ceramic objects, the solid phase is composed by ceramic powder

* *Part of this chapter was published elsewhere*[5].

with particle sizes ranging typically between 0.1 and 100 μm. The liquid phase has the role of surrounding and separating particles from each other and facilitating their mutual sliding. Also, the capillary force generated by liquid bridges between the particles in a deflocculated system is believed to be the main component of the cohesive force that keeps the particles together in a coherent plastic mass[6]. Water alone is not sufficient to formulate an extrudable paste if the solid phase is not clay. In fact, the liquid phase must possess non-Newtonian behavior of visco-plastic type, that is, being characterized by the existence of a threshold stress (called yield stress or apparent yield stress), which must be exceeded for the fluid to deform and flow. This behavior can be achieved by adding thermoplastic polymers or other organics like, for example, cellulose in water[7-10]. The organic agents allow for close control of the paste viscosity and act as a binder in the green extrudate once the water has been removed by drying, imparting the necessary resistance for handling and avoiding the breakage of the green body. The ratio between the volume of the solid phase and the total volume of the paste is defined as the solid loading and is the main characteristic that influences the flow behavior and the extrudability of the paste.

From a quantitative point of view, it is important to define the solid loading corresponding to the exact liquid volume required to fill the interparticle volume in a loose packed configuration, which is typically called the critical volume fraction or maximum solid loading (ϕ_m). Only when the solid loading is lower than ϕ_m, the paste can be extruded because the liquid layer surrounding the solid particles is thick enough to allow their sliding. However, if the solid loading is too low, the paste will behave like a viscous suspension and will not be able to retain the extruded shape. Conversely, for solid loadings increasing and tending to ϕ_m, the liquid phase is not adequate to allow for easy particle sliding. This is responsible for large frictional force resulting in a rapid increase of the extrusion pressure that can quickly exceed equipment limit. If ϕ_m is eventually attained or exceeded, the paste loses its ability to flow and the viscosity tends to infinity[11]. If the solid loading is optimized, the paste is soft enough to be formed with moderate extrusion pressure but also sufficiently strong to minimize deformations of the extruded green shape. An accurate experimental determination of ϕ_m is important for a successful formulation of the ceramic paste and several methods have been proposed in literature[12-15].

After extrusion, most of the liquid phase is removed during successive drying; therefore, the solid loading has a considerable influence not only on the flow properties of the paste but also on the drying shrinkage and, consequently, on the green and sintered densities of the extrudate[16]. The present work was developed as part of a larger project for the fabrication of Solid Oxide Fuel Cells (SOFC) anodes. With the aim of tuning the extrusion procedure and reducing defects and excessive warping during drying and sintering, it was necessary to look for a value of the solid loading as high as possible, to reach high green and

sintered density, compatibly with maintaining good flow properties and moderate extrusion pressures. Therefore the influence of solid loading on the shrinkage upon drying and on the green and sintered density of extruded gadolinia-doped ceria is investigated, and a novel procedure for the determination of the maximum solid loading is proposed.

3.2 Experimental

The preparation of an extrusion paste typically follows several successive stages, which aim to the optimal mixing of the components and the production of a homogeneous distribution of the two phases (e.g. liquid and solid)[17]. In the present work, the ceramic powder used was commercially available (Treibacher Industries, Austria) gadolinia 10mol% doped ceria (GDC10) (d_{50}=0.27 μm, BET=9.10 m^2/g). Hydroxypropil methyl-cellulose (HPMC, Sigma Aldrich, MW~22 kDa) was used as binder and thickening agent as 2wt% based off of the liquid phase for each solid loading value studied. The solid components were dry-mixed together in a planetary mixer for 3h. The mixed powder was than slowly added to bi-distilled water to reach the requested solid loading, which was evaluated as:

$$\phi = \frac{m/\rho_{th}}{m/\rho_{th}+V} \qquad (3.1)$$

Where m is the mass of the powder, ρ_{th} its theoretical density and V the volume of the liquid phase, provisionally ranging between 40 and 50vol%. The latter step (i.e. wet mixing) was carried on using a kneading hook mounted on a vertical shaft mixer for 5min ca. until all the water was completely absorbed and the paste was homogeneous. The paste was then extruded through a flat die with several small holes of 4mm diameter. This high shear-mixing step contributed to further homogenize the paste and break any remaining agglomerates. The paste was then placed in a sealed plastic bag and stored overnight in humidified vessel at room temperature to avoid any change in the water content.

The extrusion procedure was performed by an in-house built aluminum ram extruder (Fig. 3.1). It is constituted of a barrel with an internal diameter of 23 mm and a loading capacity of 60 cm^3 inside of which a ram slides. An o-ring placed on the final part of the ram ensured a sufficient seal with the barrel wall. The internal surface of the cylinder was carefully polished to mirror finishing with diamond paste to reduce the friction with the piston. The squared die used in this work was 23.13 mm long and a diameter of 5.1 mm. The upper part of the

piston was fitted to a 100 kN load cell on a universal mechanical testing machine (MTS, mod. 810) that allowed the recording of the load required to keep the ram speed constant at 10 mm/min during the whole process. The extruded samples were collected within the grooves of a sample holder specifically realized in polyurethane sponge to avoid differential water evaporation and warping upon drying. The green samples were dried slowly for the first hour in a humid environment (relative humidity of 86%) and then overnight in presence of silica salts at room temperature. The remaining drying was carried out in oven at 110°C for 4 h. The bulk densities of the green samples were evaluated subtracting the net weight of the binder. The dried samples were heated at 2°C/min up to a de-binding temperature of 500°C, maintained for one hour, and then at 5°C/min up to the sintering temperature of 1550°C that was kept for 2h. The bulk densities were measured by the Archimedes method. The densification behavior of the green sample was measured by dilatometry (Linseis L75) from room temperature to 1550°C with a constant heating rate of 5°C/min. The dilatometric shrinkage data were then converted into densification curves[18]. Microstructure examination was performed by scanning electron microscopy (SEM, Jeol, JSM5500) on manually produced fracture surfaces.

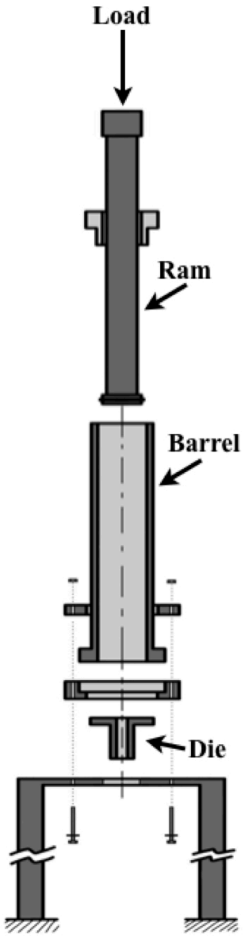

Fig. 3.1. Schematic drawing of the ram extruder.

3.3 Results and discussion

3.3.1 Influence of solid loading on the extrusion pressure

During extrusion, the force on the load cell was monitored as a function of the distance travelled by the ram. The force can be decomposed into a shaping component, associated to the deformation of the plastic mass through the die, and a friction component, related to the slip of the paste on the barrel and die internal walls during flow. Supposing that the rheological characteristics of the paste do not change during the whole extrusion process, the shaping component, which is related to the plastic yield stress of the paste, and the die friction component remain constant while the barrel friction component decreases as the ram advances and the wetted barrel surface decreases.

The typical plot of an extrusion process, accordingly, shows an initial zone of slow pressure increase due to the flattening of the paste in the barrel, followed by an abrupt increase due to the die filling. The pressure plot flattens as soon as the paste starts to be extruded and, depending on the value of friction between paste and barrel, decreases as the less of the barrel surface wetted by the paste, eventually reaching a minimum. The Benbow-Bridgewater model well indicates the dependence of the minimum value of the extrusion pressure from the geometrical characteristics of the extruder and some rheological parameters of the paste as shown by Eq. 3.2:

$$P = P_e + P_l = 2(\sigma_0 + \alpha V^n)\ln\left(\frac{D_0}{D}\right) + (\tau_0 + \beta V^m)4\left(\frac{L}{D}\right) \qquad (3.2)$$

where α is a velocity-dependent factor for the convergent flow, β is the velocity-dependent factor for parallel flow, n and m are the exponents of the extrudate velocity, σ_0 is the paste bulk yield value, τ_0 is the paste shear yield stress, D_0 and D are diameters of the barrel and the die respectively, L is the die-land length and V is the extrudate velocity. In Eq. 3.2, the pressure is obtained as the sum of two contributions: one from the die-entry (P_e) and one from the die-land (P_l).

The subsequent pressure increase is recorded when the ram is about to enter the static zone near the die. The paste located in the bottom portion of the barrel around the die, also called dead zone, can hardly flow due to sharp corners. This usually causes a steep rise in pressure toward the end of the process. Fig. 3.2 shows the plots corresponding to the extrusion of two pastes with solid loading of 44vol%, one of them having been subjected to the high shear mixing procedure before extrusion. The process steps described above are clearly shown. The plot corresponding to the highly shear mixed paste (paste A) exhibits a reduction of the extrusion pressure of about 30%. Moreover, the surface finish was considerably better in this case, this indicating that the high shear mixing

contributes to further homogenize the paste and to break down any agglomerate created during the wet mixing phase.

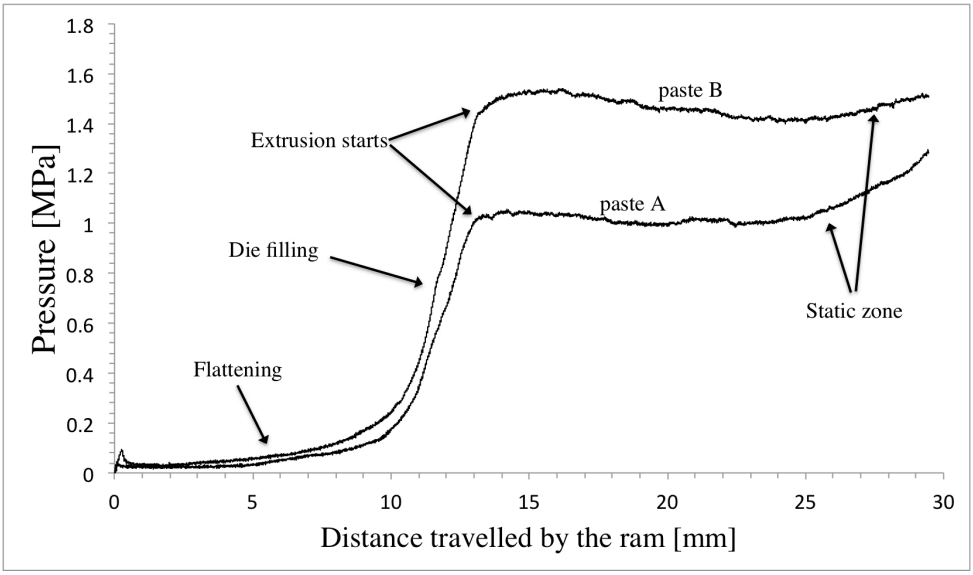

Fig. 3.2 Extrusion pressure as a function of the distance travelled by the ram for two pastes with 44vol% solid loading. Paste A was subjected to high shear mixing before extrusion.

When the pressure gradients during the extrusion are large, typically because of high plastic yield stress, liquid phase migration phenomena can occur and the rheological characteristic of the paste can locally change with time[19]. If this is the case, the paste inside the barrel is drier than the extruded one. This causes a further consolidation of the paste and the quick rise of both the shaping and the friction components of the extrusion force[20].

The liquid phase migration and the corresponding paste consolidation result to be also dependent on the extrusion velocity and modify substantially the flow typology. The effect of the liquid migration can be observed in Fig. 3.3 which shows the extrusion pressure for pastes prepared with solid loading ranging between 40 and 50vol%. When the solid loading is increased, the liquid volume available for the mutual flow of the particles is lower and this leads to a higher plastic yield stress and a higher value of pressure required to activate the extrusion process. For 40vol% solid loading, the pressure is approximately constant and thus, the friction with the barrel can be considered negligible. Therefore, the only contribution for this paste comes from the shaping and the die friction forces that are constant, assuming that no liquid migration is clearly observed. For solid loadings of 42 - 46vol% a slight decrease in pressure is shown in the stable operation step until the pressure rises for effect of the static zone. The 48vol% solid loading paste exhibits a noisier signal as result of a considerable friction with the extruder walls. The liquid phase is too scarce and does not allow an efficient flow of the paste. The higher pressure required for the extrusion causes the migration of the liquid phase as indicated by the early and steep rise of the final part of the signal.

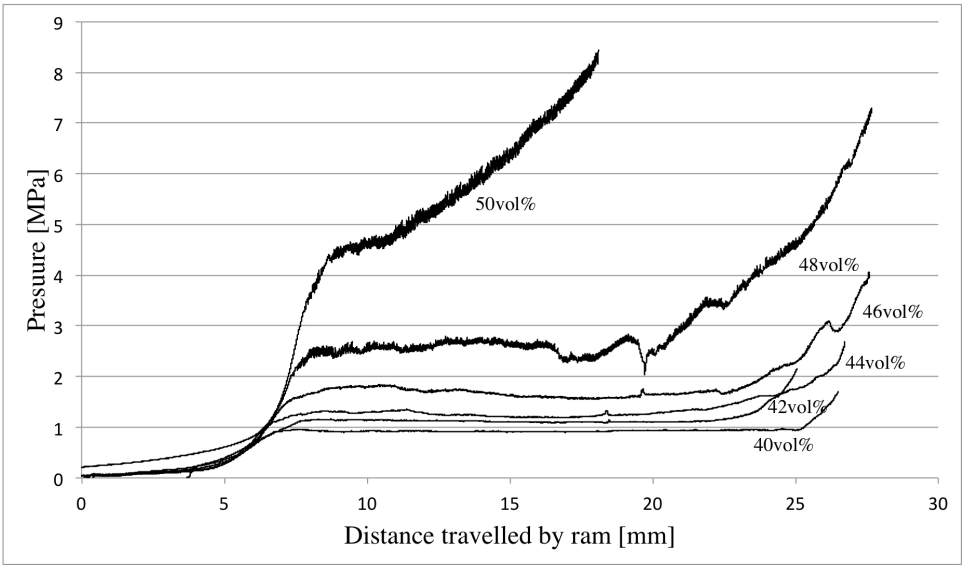

Fig. 3.3 Extrusion pressure as a function of the distance travelled by the ram for pastes of various solid loading.

This dewatering effect is even more significant for the paste with 50vol% solid loading. It does not show any plateau of stable operation but a continual increase of pressure up to the extruder pressure limit set at 8.5 MPa. Considering the extrusion pressure as the minimum value assumed by the pressure during the stable operation, its dependence on solid loading is represented in Fig. 3.4. For the 50vol% paste, seen the absence of a minimum, the extrusion pressure can be considered equal to the minimum value assumed by the pressure from the moment the paste is extruded.

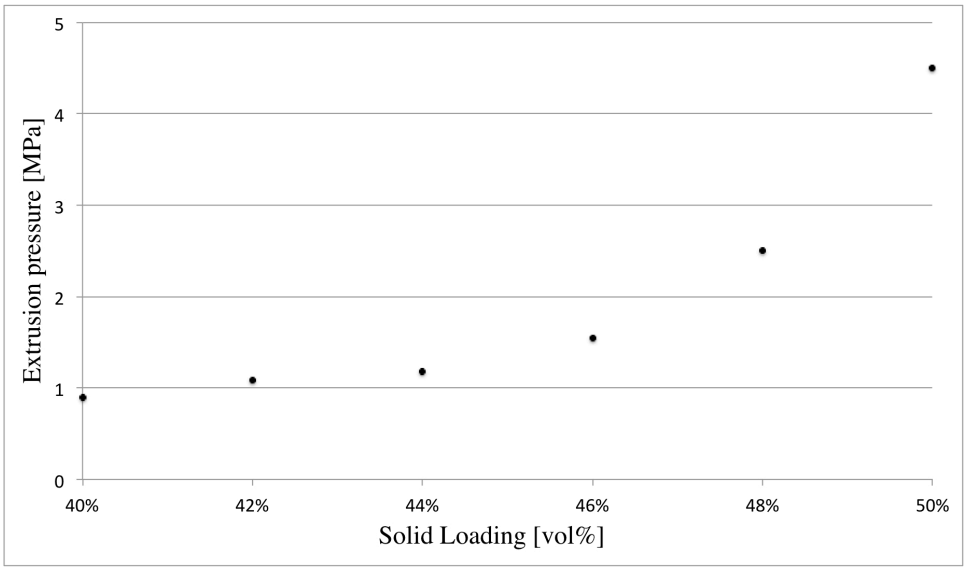

Fig. 3.4 Evolution of the extrusion pressure with solid loading.

3.3.2 Drying shrinkage and green density

During drying, the liquid phase is removed from the extrudate and the powder particles pack together. The mechanism is very similar to that proposed for the initial stage of liquid-phase sintering[15] and leads to an overall shrinkage of the samples and an increase of the green density[21]. Generally, drying proceeds through two main steps. During the first one, liquid flows through the pores from the interior to the sample surface and there evaporates. The water loss is linear in time with rate depending on the sample geometry, the vapor pressure and the temperature. As the meniscus radius decreases, the pores start to shrink and the density of the green body increases correspondingly until the powder particles touch each other. During the following drying step, the drying rate slows down: the liquid-vapor meniscus starts to retreat inside the pores and the transport of liquid to the surface is the rate-limiting mechanism. The liquid that cannot reach the surface has to evaporate within the pores, further decreasing the drying rate[22,23]. Higher liquid content corresponds to larger shrinkage. In the analyzed range, the radial shrinkage during drying depends linearly on the solid loading as shown in Fig. 3.5.

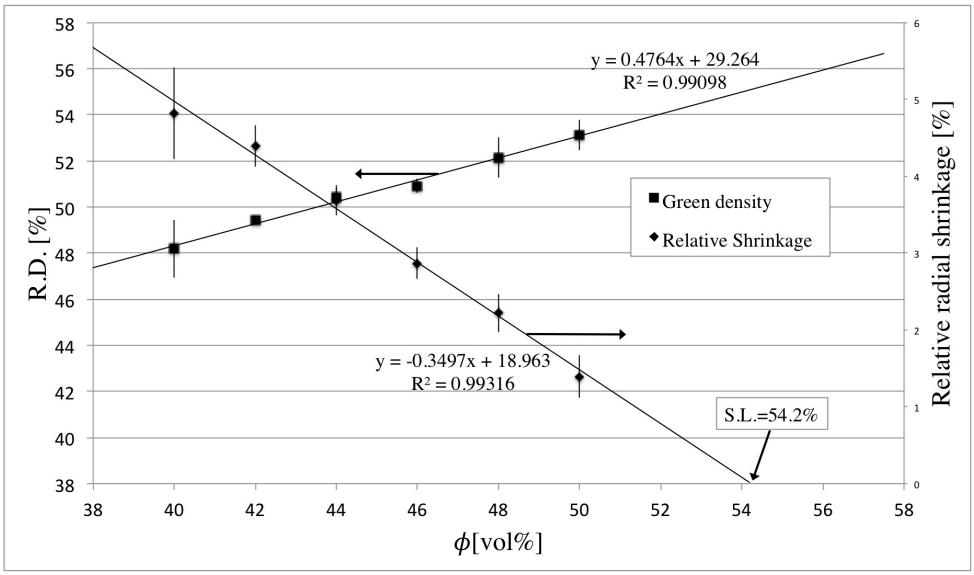

Fig. 3.5 Relative bulk density of the extrudate and radial shrinkage for dried sample as a function of the solid loading; the standard deviation is also shown. Continuous lines correspond to linear fitting of the experimental average data (fitting equations and correlation coefficient are shown). The graphical construction used to determine the maximum solid loading is also shown.

The average relative bulk density of the dried extrudate, represented in the same Fig. 3.5, also follows a linear relationship with respect to the solid loading[16]. It is evident that a larger shrinkage leads to a larger difference between the dried

green density and the initial solid loading of the paste. The samples formulated with 40vol% solid loading became ~8% denser upon drying while samples with 50vol% solid loading increased their density of ~3%. Although the shrinkage during drying does not bring every sample to the achievement of the same final bulk density: the larger is the shrinkage, the smaller is the density achieved by the dried green sample. Also, the packing resulting from large shrinkage is lower than the one relative to small shrinkage. In other words, the drying mechanism appears to have worst efficiency for lower solid loadings, resulting in a lower green density. This is confirmed also by microstructural SEM analyses reported in Fig. 3.6 where samples at 40 and 50vol% are compared, indicating that lower packing efficiency corresponds to the presence of unfilled macroporosity during drying.

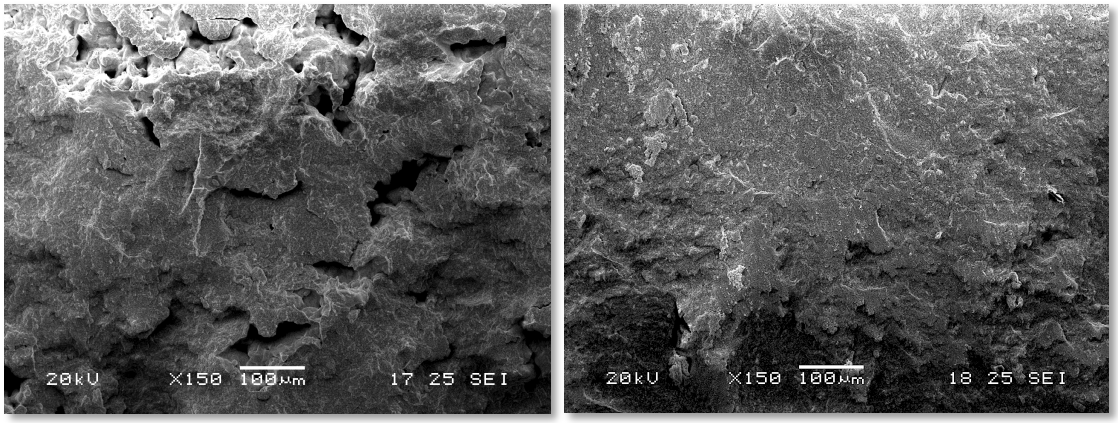

Fig. 3.6 SEM micrographs of fracture surface for green samples with 40 vol% (left) and 50 vol% (right) solid loading.

It can be interesting to observe that the extrapolation of the shrinkage linear trend intersects the x-axis relative to no shrinkage effect (Fig. 3.5) at a value of 54.2 vol% of solid loading. Such value can be associated to the solid loading of a paste that is not subjected to density increase during drying and therefore to the maximum solid loading, ϕ_m, suitable for the specific powder.

3.3.3 Sintered density and densification rates

The densification curves were recorded for samples formulated with different solid loadings and they showed very similar trend Fig. 3.7. The final density reached after the heating cycle depends primarily on the bulk density of the dried green body, as already observed in literature also for samples obtained by other production techniques[24-26]. The densification kinetic is also function of the green density: the maximum densification rate is slightly faster for higher

solid loadings although the overall difference is negligible considering that the values ranged between 0.82 and 0.87%·min^{-1} (Fig. 3.8). Even for what concerns the temperature of maximum densification, it appears to be the same for every analyzed sample, around 1380°C.

The relative bulk density obtained after sintering at 1550°C for 2h and calculated as $\rho_r = \rho_b/\rho_{th}$, where ρ_b is the measured bulk density and ρ_{th} is the theoretical density of GDC10 (7.22g·cm^{-3}) is reported in Tab. 3.1. The samples with solid loading higher than 42vol% achieved relative density higher than 97% and can be considered as fully dense. These observations confirm the influence of the presence of residual porosity in the green extrudate (Fig. 3.6) on the final microstructure.

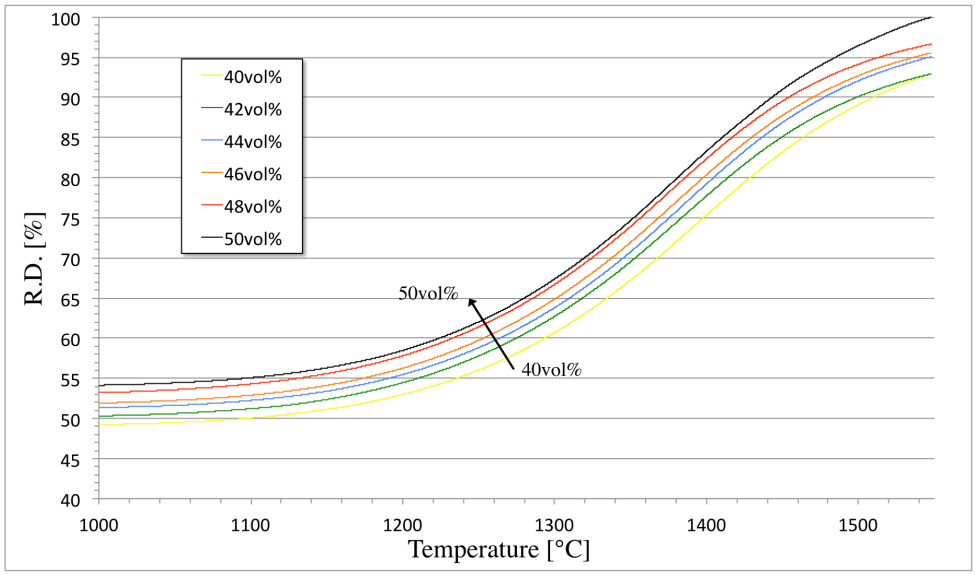

Fig. 3.7 Densification of green extrudates upon heating for solid loadings between 40 and 50vol%.

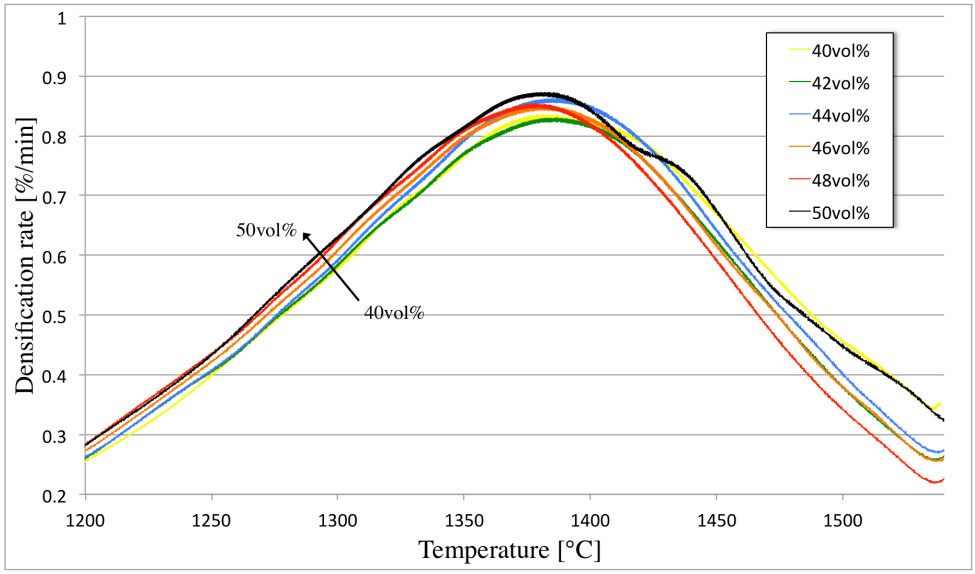

Fig. 3.8 Densification rate of green extrudates upon heating for solid loading between 40 and 50vol%.

Tab. 3.1. Relative density after sintering as a function of the initial solid loading.

ϕ	0.40	0.42	0.44	0.46	0.48	0.50
ρ_r[%]	94.6	96.3	97.5	98.5	99.3	99.1

From the previous observations, a criterion for the experimental determination of the correct solid loading for the extrusion of ceramic bodies can be obtained. If an high solid loading paste allows to obtain samples experiencing small shrinkages and with less possibilities of damaging during drying, its extrusion leads to the onset of large extrusion pressures that are often associated with de-watering effects. Contrarily, a paste with low solid loading minimizes the extrusion pressure, avoiding dewatering and damaging of the extruder but it is also associated to large drying shrinkages and lower green/sintered densities.

3.3.4 Prediction of viscosity of extrusion pastes

The maximum solid loading, ϕ_m, previously obtained from the linear extrapolation of the drying shrinkage is here compared with the values that can be calculated from the analysis of the pastes viscosity on the basis of previous reported studies. There are numerous semi-empirical models that allow predicting the viscosity of highly concentrated ceramic suspensions[1]. In the present analysis two of them are considered: the most widely used Krieger-Dougherty equation[27]:

$$\eta = \eta_0 \left[1 - \left(\frac{\phi}{\phi_m}\right)\right]^{-[\eta]\phi_m} \qquad (3.3)$$

and the Reddy equation[28], based on the rule of mixtures:

$$\eta = \eta_0 \left(\frac{\phi_m}{\phi_m - \phi}\right) \qquad (3.4)$$

Where η_0 is the viscosity of the pure liquid medium and $[\eta]$ is an empirically derived hydrodynamic crowding factor defined as intrinsic viscosity.
The parameters η_0, $[\eta]$ and ϕ_m are typically obtained by fitting procedure of the experimental data. The apparent viscosity of ceramic pastes, considered to be

non-Newtonian fluids, is given by the ratio between the true shear stress and the apparent shear strain at the die wall:

$$\eta_a = \frac{\tau_w}{\dot{\gamma}_a} \tag{3.5}$$

The shear stress for a circular die depends on the geometry and on the pressure gradient along it. It can be calculated considering the sum of the forces acting on a cylindrical element subjected to steady laminar flow[29]:

$$\tau_w = \frac{R}{2}\left(\frac{\partial P}{\partial z}\right) = \frac{R}{2}\frac{\Delta P}{L} \tag{3.6}$$

Where ΔP is the pressure variation along the extremes of the die of length L and radius R and the right term is obtained by integrating the pressure gradient, considered linear, along the die. Nonetheless, as pointed out before, the pressure recorded by the load cell above the piston includes also contributions due to the friction with the barrel and the shaping force needed to modify the section of the paste from the barrel to the die.

To isolate the contribution to the pressure gradient due to the flow along the die only, the Bagley correction is usually applied[30]. It allows estimating the pressure drop at the die entrance and exit by linear extrapolation of the steady state pressure readings for dies of different lengths. The pressure drop extrapolated for die length equal to zero is then subtracted to any other pressure readings to obtain the value of the true shear stress. Nevertheless, in addition to the requirement of several measurements, this correction is not always immediate since the obtained values can hardly be fitted linearly[31]. A further problem concerns the identification of the exact value of the extrusion pressure. As a matter of fact, often the pressure trend does not allow distinguishing univocally the steady state plateau, especially in case of very tough pastes and liquid migration (Fig. 3.3). Therefore, in the case of the measurements reported above, a more reliable reading of the pressure gradient along the die can be obtained from the analysis of the first stage of the extrusion plot, before the maximum pressure corresponding to the paste coming out from the die is reached. This phase is reported in Fig. 3.9 for extrusions of 40 and 50 vol% solid loading pastes.

As the plot clearly shows, the initial stage of extrusion is composed by three steps corresponding to three specific physical processes: a first phase of slow increase due to the flattening of the paste, a more steep increase due to the transfer of the paste to the die land and, eventually, a steady rise corresponding to the flow of the paste within the die.

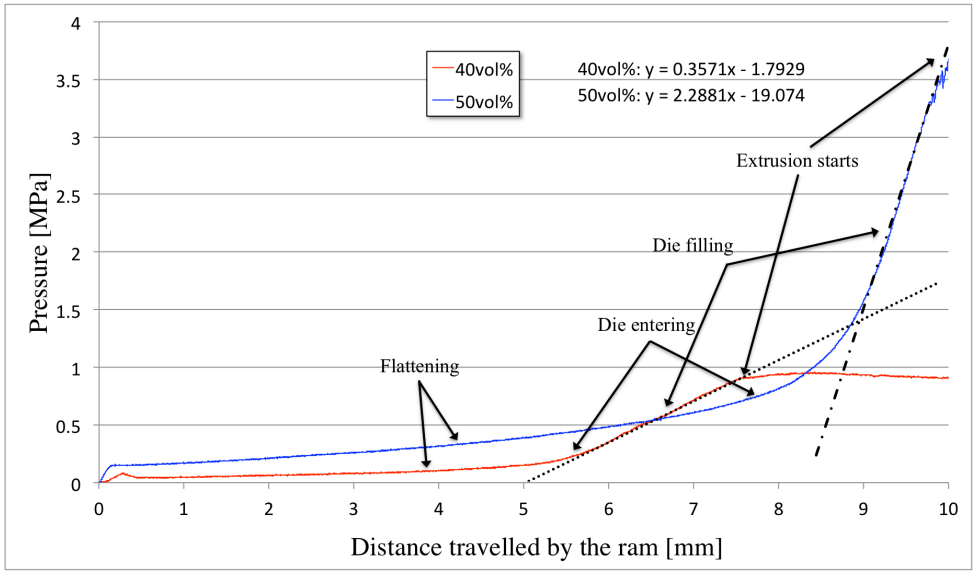

Fig. 3.9 Pressure recorded by the load cell during the initiation of extrusion process as a function of the movement of the ram for 40 and 50 vol% solid loading pastes. In both cases, the steady rise corresponding to the flow within the die is well approximated by the reported linear equation.

In order to obtain the pressure gradient required in Eq. 3.6, it is sufficient to identify the slope of the line fitting the third phase and to convert it into the die coordinates. Considering the ceramic paste as incompressible, the ram and the extrudate velocities are connected by the equation for volume conservation:

$$v_{extr} = \frac{A_0}{A} v_{ram} \tag{3.7}$$

Where A_0 and A are the barrel and the die sections, respectively. Indicating with z_{ram} the ram displacement and with z_{extr} the paste displacement inside the die, the pressure gradient becomes:

$$\frac{\partial P}{\partial z_{extr}} = \frac{\partial P}{\partial z_{ram}} \frac{\dot{z}_{ram}}{\dot{z}_{extr}} = \frac{\partial P}{\partial z_{ram}} \frac{v_{ram}}{v_{extr}} = \frac{\partial P}{\partial z_{ram}} \frac{A}{A_0} \tag{3.8}$$

That, inserted in Eq. 3.6, allows for the evaluation of the true die wall shear stress. The values obtained with this approach are reported in Fig. 3.10 for variable solid loadings. The apparent shear rate can be evaluated as[29]:

$$\dot{\gamma}_a = \left(\frac{4Q}{\pi R^3}\right) \tag{3.9}$$

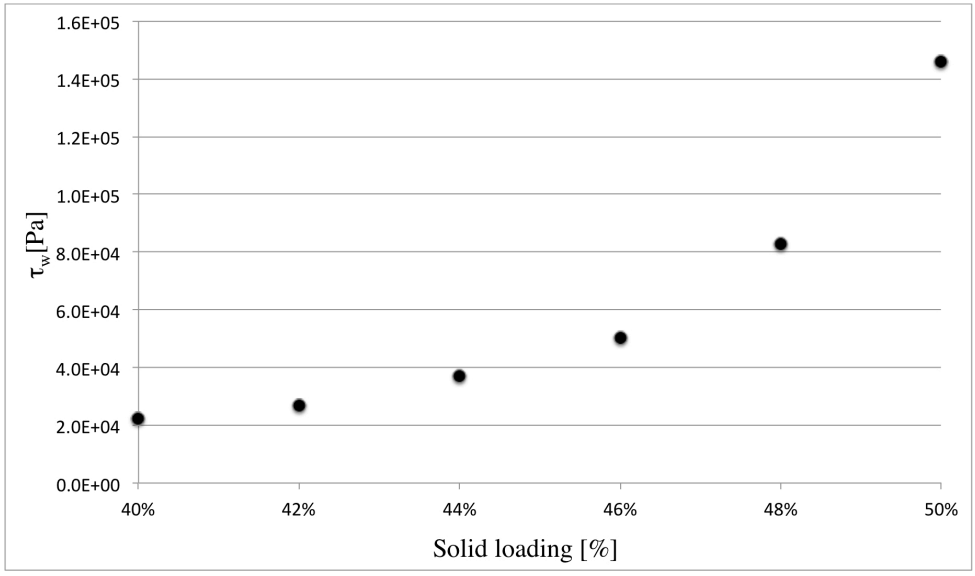

Fig. 3.10 True die wall shear stress for variable solid loading.

Where Q is the flow rate through the die of radius R. The apparent viscosity of the pastes is given by Eq. 3.4 and well agree with viscosities of extrusion pastes obtained by similar capillary rheometry measurement[28,29,32,33]. The apparent viscosity for different solid loadings is used for the determination of the best fit parameters for Eq. 3.2 and 3.3, linearized as follows:

Krieger-Dougherty : $$\ln \eta = -[\eta]\phi_m \ln\left(1 - \frac{\phi}{\phi_m}\right) + \ln \eta_0 \qquad (3.10)$$

Reddy et al. : $$\eta\phi = \eta\phi_m - \eta_0\phi_m \qquad (3.11)$$

The values for ϕ_m, η_0 and $[\eta]$ are obtained by linear fit of Eqs. 3.10 and 3.11 as shown in Figs. 3.11a and 3.11b, and are reported in Tab. 3.2. A detailed description about the non-linear optimization of the parameters for the Krieger-Dougherty and other models, can be found elsewhere in literature[34].

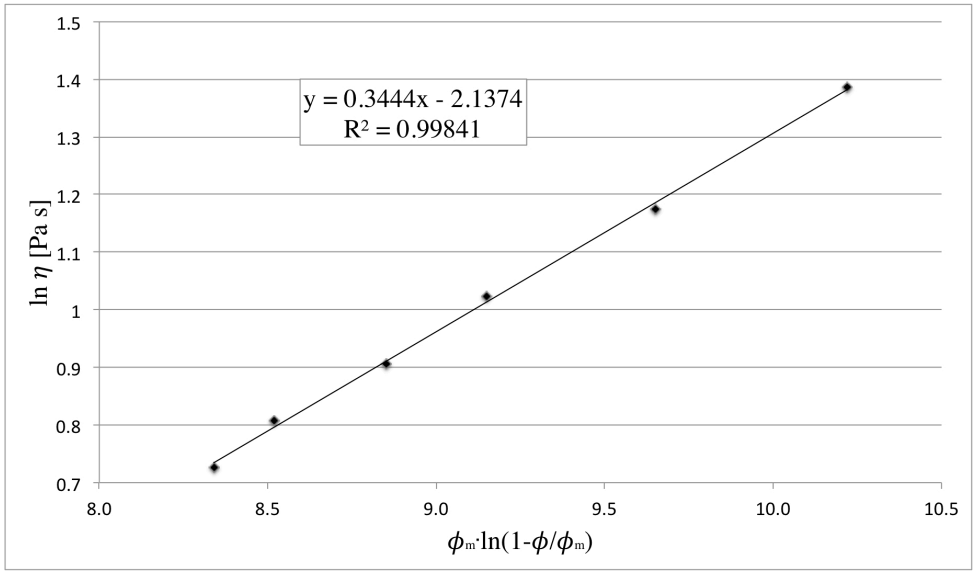

Fig. 3.11a. Linearization and fit of Krieger-Dougherty model. Fitting line equation and correlation factor are reported.

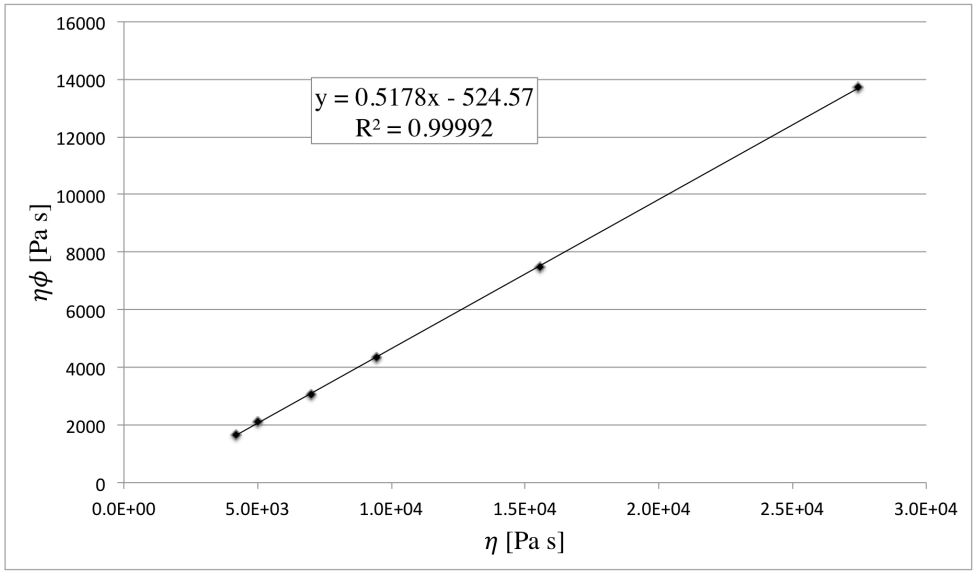

Fig. 3.11 Linearization and fit of Reddy et al. model. Fitting line equation and correlation factor are reported.

Tab. 3.2 Fitting parameters estimated from Figs. 3.11a and 3.11b for the two analyzed models.

	[η]	η0[Pa·s]	ϕm
Krieger-Dougherty	2.90	498.4	0.54
Reddy et al.	-	1013.1	0.52

As shown in Fig. 3.12, Eqs. 3.2 and 3.3 fit considerably well the apparent viscosity experimental values obtained here although the Krieger-Dougherty model seems to predict the relationship between η_a and ϕ slightly better in the analyzed range. The ϕ_m values obtained from the two different fits are substantially similar to that calculated from the linear extrapolation of the drying shrinkage to zero previously reported (0.542) (Fig. 3.5), thus confirming the goodness of the approach proposed in the present study.

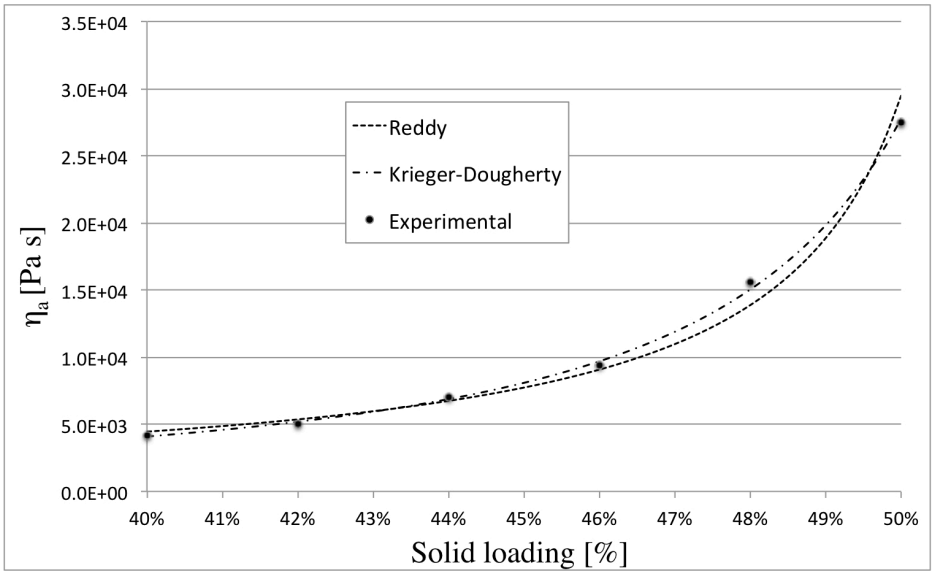

Fig. 3.12 Experimental apparent viscosity and trends calculated on the basis of Eqs. 3.2 and 3.3 with the parameters reported in Tab. 3.2.

3.4 Conclusions

In the formulation of a ceramic extrusion paste, the identification of the optimal range of solid loading has a great importance. Larger amount of powder causes high friction and liquid phase migration, while lower solid loadings correspond to very soft pastes unable to maintain the extruded shape. The upper limit of the range is defined as the maximum solid loading and corresponds to the minimum volume occupied by the specific powder in a close compact configuration. From its knowledge, the minimum volume of liquid phase necessary for the formulation of a ceramic phase was derived. The addition of further liquid in the paste formulation produces the formation of a layer between the powder particles, which allows for their mutual sliding. The optimal volume of additional liquid phase that permits to limit the extrusion pressure and the wear of the apparatus, depends on the specific extruder architecture and can be empirically derived.

In the present work, the maximum solid loading in gadolinia-doped ceria pastes was determined by the extrapolation down to zero of the drying shrinkage of green extrudates formulated with variable solid loadings. The obtained value was compared to the analogous results determined by using two semi-empirical equations (Krieger-Dougherty and Reddy equations) describing the viscosity of high concentrated ceramic suspension as a function of the solid loading. The die wall shear stress, necessary for the evaluation of the viscosity, was also acquired, without need of any correction, by a novel method based on the analysis of the slope of the first stage of extrusion plot, corresponding to the flow of the paste trough the die. The viscosities obtained by this approach are comparable to literature data reported for ceramic pastes with similar solid loading.

Thanks to this preliminary study, the know-how on the ceramic paste formulation, the paste preparation steps and the effect of the liquid phase on the rheology and extrusion pressure was developed. It also allowed for the tuning of the extruder design and of the extrusion procedure. The acquired knowledge was implemented on the formulation of pastes composed by two solid phases (ceramic and metal oxide powder) and on the extrusion of cermet tubular supports that will be used in the rest of this work.

References

1. Senapati, P. K., Panda, D. & Parida, A. Predicting viscosity of limestone–water slurry. *Journal of Minerals & Materials Characterization & Engineering* **8**, 203–221 (2009).
2. Händle, F. *Extrusion in ceramics*. (2007).
3. Sigmund, W. M., Bell, N. S. & Bergström, L. Novel Powder-Processing Methods for Advanced Ceramics. *J Am Ceram Soc* **83**, 1557–1574 (2000).
4. Vongeheur, H. Fundamentals of Extrusion. *Manufacturing Confectioner* (2008).
5. Azzolini, A., Sglavo, V. & Downs, J. Novel method for the identification of the maximum solid loading suitable for optimal extrusion of ceramic pastes. *J Adv Ceram* (2014).
6. Chen, Z., Ikeda, K., Murakami, T. & Takeda, T. Effect of particle packing on extrusion behavior of pastes. *J Mater Sci* **35**, 5301–5307 (2000).
7. August, C. & Haber, R. Benbow analysis of extruded alumina pastes. *Whitewares and Materials: Ceramic Engineering and Science Proceedings* (2009).
8. KAYA, C. Extrusion of ceramic tubes with complex structures of non-uniform curvatures made from nano-powders. *Journal of the European Ceramic Society* **24**, 3663–3670 (2004).
9. Benbow, J., Jazayeri, S. & Bridgwater, J. The flow of pastes through dies of complicated geometry. *Powder Technology* (1991).

10. Khan, A. U., Briscoe, B. J. & Luckham, P. F. Evaluation of slip in capillary extrusion of ceramic pastes. *Journal of the European Ceramic Society* **21**, 483–491 (2001).
11. Pabst, W. Fundamental considerations on suspension rheology. *CERAMICS SILIKATY.* **48**, 6–13 (2004).
12. Reddy, J. J., Vijayakumar, M., Mohan, T. & Ramakrishnan, P. Loading of solids in a liquid medium: Determination of CBVC by torque rheometry. *Journal of the European Ceramic Society* **16**, 567–574 (1996).
13. Liu, F. & Chou, K. Determining critical ceramic powder volume concentration from viscosity measurements. *Ceram Int* **26**, 159–164 (2000).
14. Reddy, J. J. Novel method for assessment of critical powder packing during powder forming. *Powder metallurgy* **39**, 281–285 (1996).
15. Wright, J. K., Edirisinghe, M. J., Zhang, J. G. & Evans, J. R. G. Particle Packing in Ceramic Injection Molding. *J Am Ceram Soc* **73**, 2653–2658 (1990).
16. Liu, D. M. & Tseng, W. J. Influence of solids loading on the green microstructure and sintering behaviour of ceramic injection mouldings. *J Mater Sci* **32**, 6475–6481 (1997).
17. Benbow, J. & Oxley, E. The extrusion mechanics of pastes--the influence of paste formulation on extrusion parameters. *Chemical Engineering Science* (1987).
18. Maca, K., Pouchly, V. & Boccaccini, A. R. Sintering densification curve: A practical approach for its construction from dilatometric shrinkage data. *Sci Sintering* **40**, 117–122 (2008).
19. Liu, H., Liu, J., Leu, M. C., Landers, R. & Huang, T. Factors influencing paste extrusion pressure and liquid content of extrudate in freeze-form extrusion fabrication. *Int J Adv Manuf Technol* (2012).doi:10.1007/s00170-012-4534-0
20. Perrot, A., Lanos, C., Estellé, P. & Melinge, Y. Ram extrusion force for a frictional plastic material: model prediction and application to cement paste. *Rheol Acta* **45**, 457–467 (2006).
21. Shaw, H. M. & Edirisinghe, M. J. Shrinkage and particle packing during removal of organic vehicle from ceramic injection mouldings. *Journal of the European Ceramic Society* **15**, 109–116 (1995).
22. Chotard, T., Quet, A., Ersen, A. & Smith, A. Application of the acoustic emission technique to characterise liquid transfer in a porous ceramic during drying. *Journal of the European Ceramic Society* **26**, 1075–1084 (2006).
23. Scherer, G. Theory of Drying. *J Am Ceram Soc* **73**, 3–14 (1990).
24. Rahaman, M. & Jonghe, L. Effect of Green Density on Densification and Creep During Sintering. *J Am Ceram Soc* **74**, 514–519 (1991).
25. Özkan, N. & Briscoe, B. J. Overall shape of sintered alumina compacts. *Ceram Int* **23**, 521–536 (1997).
26. Mukherjee, A., Maiti, B., Sharma, Das, A., Basu, R. N. & Maiti, H. S. Correlation between slurry rheology, green density and sintered density of tape cast yttria stabilised zirconia. *Ceram Int* **27**, 731–739 (2001).
27. Bergström, L. Colloidal Processing of ceramics. *Handbook of Applied Surface and Colloidal Chemistry* (2001).
28. Reddy, J., Ravi, N. & Vijayakumar, M. Simple model for viscosity of powder

injection moulding mixes with binder content above powder critical binder volume concentration. *Journal of the European Ceramic Society* **20**, 2183–2190 (2000).
29. Son, Y. Determination of shear viscosity and shear rate from pressure drop and flow rate relationship in a rectangular channel. *Polymer* **48**, 632–637 (2007).
30. Draper, O., BLACKBURN, S., Dolman, G., Smalley, K. & Griffiths, A. A comparison of paste rheology and extrudate strength with respect to binder formulation and forming technique. *J Mater Process Tech* **93**, 141–146 (1999).
31. Alfani, R. Rheological test methods for the characterization of extrudable cement-based materials - A review. *Mater. Struct.* **38**, 239–247 (2005).
32. Yilmaz, Z., Dogan, M. & Alkan, M. Rheological and wall slip properties of kaolinite-silicon oil pastes during extrusion. *Journal of Ceramic Processing Research* **11**, 752–759 (2010).
33. Alfani, R., Grizzuti, N., Guerrini, G. L. & Lezzi, G. The use of the capillary rheometer for the rheological evaluation of extrudable cement-based materials. *Rheol Acta* **46**, 703–709 (2007).
34. Hurysz, K. & Cochran, J. The application of models for high solids content suspensions to pastes. *Journal of the European Ceramic Society* **23**, 2047–2052 (2003).

4. Sintering aids for the low-temperature densification of GDC10

Abstract

The addition of small amounts of transition metal oxides (TMOs) can increase the sinterability of GDC10, decreasing the sintering temperature required for its full densification. In this chapter, the effect of various sintering aids is studied by means of dilatometry measurement. The most promising sintering aid for GDC10 is identified and the influence of its concentration examined. Some mechanisms of activated sintering proposed in literature are also discussed with particular reference to the materials used in this study.

Keywords: Sintering aids, Activated sintering, Vegard's Slope.

4.1 Introduction

Several issues arise when substituting Ni with Cu as the electronically conductive phase in SOFC anodes, mostly related to its low melting temperature (1083°C). This means that the cell operating temperature must be limited to prevent the coarsening of the Cu phase which would result in decreasing the cell performance. Due to this, Cu-based anodes are suitable for operations at temperatures lower than 700°C. Decreasing the operating temperature is beneficial in several aspects, such as easing the heat management system, enhancing the stability of the cells and enabling the use of cost-effective gas sealing or interconnecting materials[1]. But it also decreases the ionic conductivity of the electrolyte, causing high resistive losses in the cell. To overcome this problem there are two possible approaches.

The first one regards the employment of an electrolytic material with superior ionic conduction properties in the intermediate temperature range where the material used for the state of the art electrolyte, yttria stabilized zirconia (YSZ), does not have a satisfactory ionic conductivity. Gadolinia doped ceria (GDC10) is a very promising electrolytic material for intermediate temperature fuel cells (IT-SOFCs) because of its high ionic conductivity between 500 and 700°C[2-4].

The second approach concerns the reduction of the electrolyte thickness. One method to achieve this is to use an anode-supported configuration, where the electrolyte is deposited as thin film on the green anodic substrate and the two layers are co-sintered together. Then both anode and electrolyte have to be subjected to the temperature treatment required for the full densification of the electrolyte (>95% r.d.). In the case of a GDC10 electrolyte this temperature can be over 1500°C[5]. The metallic phase is usually included in the anode before the sintering in form of oxide, more resistant to oxidation and high temperatures than the metal. In the case of copper, both oxides are characterized by a considerably low melting temperature. If copper (II) oxide (CuO) is employed, the maximum temperature for the co-sintering in air has to be lower than 1026°C, where reduction takes place before incongruent melting at 1091°C. In the case of copper (I) oxide (Cu_2O), the melting temperature in high-purity Ar (99.5%) is 1230°C [6]. Then, regardless the oxide and the atmosphere used during sintering, these temperatures are incompatible with the sintering temperature of GDC10.

The employment of a few mol% of transition metal oxides (TMOs) as sintering aids, allows for the reduction of sintering temperature and the increase of densification rate of GDC10. Several sintering aids for GDC10 have been identified[7,8] depending on the value of their "Vegard's Slope". In this chapter the effect of 1mol% doping of several oxides on the densification of GDC10 is analyzed. In particular, the effect of different concentrations of Li_2O is studied, considering its superior performance compared to the others. A discussion on the mechanisms promoted by the sintering aids with reference to the existing literature is also given.

4.2 Experimental

The ceramic powder used in this study was 10 mol% gadolinia doped ceria (GDC10) sub-micron powder (Treibacher Industrie AG, d_{50}=0.27µm, d_{90}=0.40µm and SSA=9.10m^2/g). $Co(NO_3)_2 \cdot 6H_2O$, $Fe(NO_3)_3 \cdot 9H_2O$, $Mn(NO_3)_2 \cdot 4H_2O$ and Li_2O were purchased from Sigma Aldrich.

Thermogravimetric analysis (TG/DTA, Netzsch thermobalance STA 409) was performed on the pure hydrated nitrates to identify their decomposition temperature by heating at 10°C·min^{-1} in Argon flux.

Doping of GDC10 was accomplished by dissolving the nitrate in ethanol and adding the appropriate amount of GDC10. The dispersion was kept stirring on a hot plate at 90°C until complete evaporation of the ethanol. The Co, Fe and Mn containing powder were calcined at 400°C for 3h and the weight loss was compared to the expected value to confirm the complete decomposition of the nitrates. The Li containing powder was not calcined but dried at 100°C

overnight. The powders were then ground and sieved (mesh size 425µm) to eliminate the largest agglomerates. Cylindrical samples were formed by uniaxial pressing at 100MPa without need of binders.
The sintering behaviors of cylindrical samples with different dopings were measured by dilatometry (Linseis L75 Platinum Series, Linseis Instrument) using an alumina support tube and a constant heating rate of 10°C·min^{-1} to 1300°C in air and argon flux.
The samples were sintered in a tubular furnace at constant heating rate of 10°C·min^{-1} with different holding time and different sintering temperature. The relative densities were measured by Archimedes method and microstructure examination was performed by scanning electron microscopy (SEM, Jeol, JSM5500) on manually produced fracture surfaces.

4.3 Results

To identify the suitable calcination temperature for each doped powder, the decomposition of the various nitrates was studied by means of thermogravimetric analysis (Fig. 4.1).

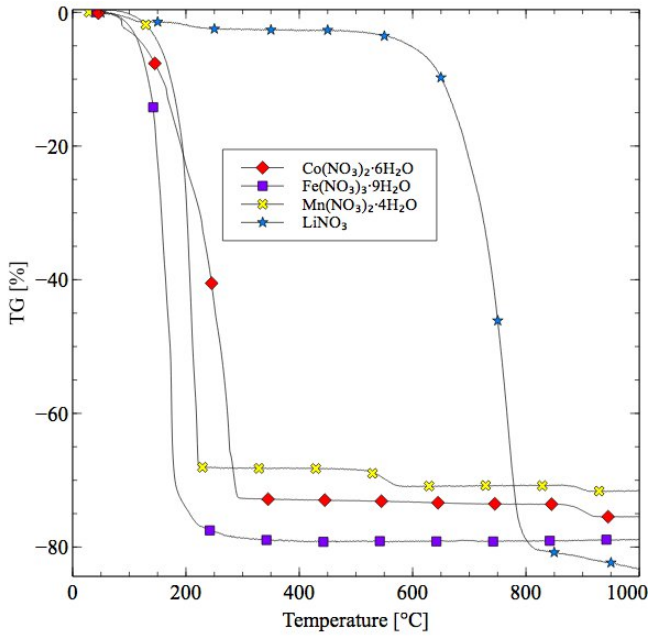

Fig.4.1 Thermogravimetric analysis of decomposition of the nitrates used in this study measured at 10°C · min^{-1} in Ar atmosphere.

The TG curves of $Co(NO_3)_2 \cdot 6H_2O$, $Fe(NO_3)_3 \cdot 9H_2O$ and $Mn(NO_3)_2 \cdot 4H_2O$ shows a continuous reduction in weight due to elimination of hydrated water that occurred in the very first stage of heating overlapping the main nitrate decomposition step. $Co(NO_3)_2$ completed the decomposition to Co_3O_4 below

300°C. The weight loss step at ~900°C was identified as the further reduction of the oxide to CoO. $Fe(NO_3)_3$ decomposed completely to Fe_2O_3 in one single step below 300°C. $Mn(NO_3)_2$ decomposition was completed to Mn_2O below ~250°C. This oxide was further reduced following the transitions:

$$Mn_2O \xrightarrow{520°C} Mn_2O_3 \xrightarrow{926°C} Mn_3O_4$$

$LiNO_3$ was the most stable nitrate tested. It started to form Li_2O at ~600°C and after a main step below 800°C, the decomposition continued up to the maximum temperature reached during the measurement. Calcination of Li doped powder at temperatures higher than 800°C caused an advanced stage of sintering, modifying considerably the powder granulometry. This could constitute an additional problem in the perspective of employing the Li doped powder in the successive ceramic forming steps. Then, the Mn, Fe, and Co doped powders were employed after calcination while the Li doped was used directly after drying, without the need of a calcination step.

The effect of the different sintering aids on the shrinkage and shrinkage rate of GDC10 was studied for a fixed concentration of 1mol% of the oxides formed after calcination and it is shown in Fig. 4.2.

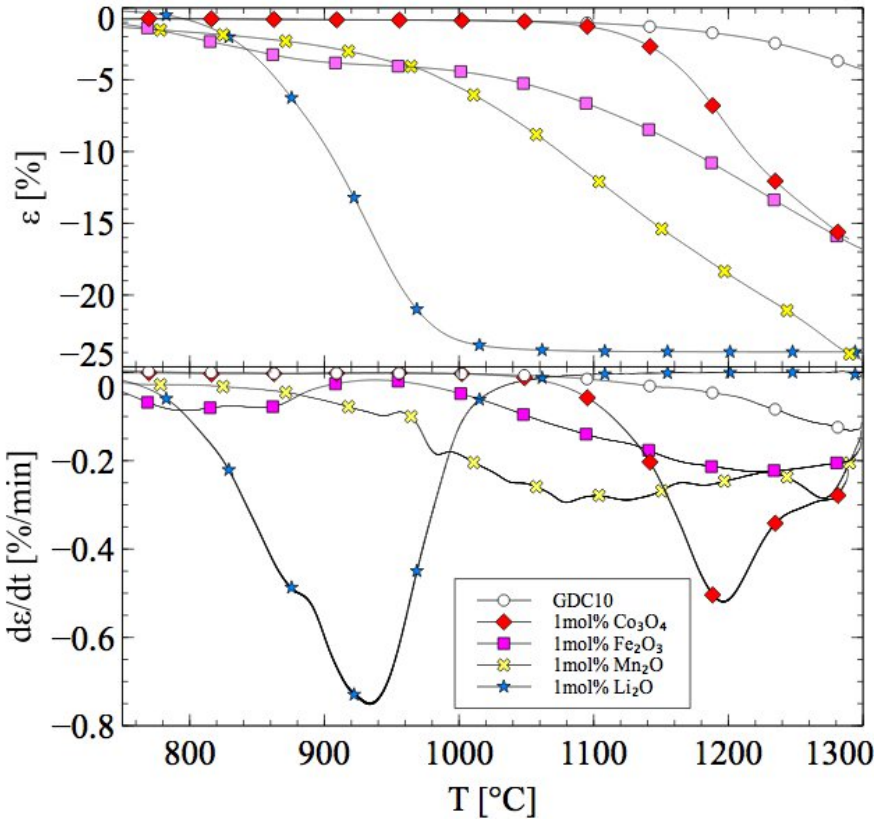

Fig. 4.2 Effect of different dopings at 1mol% concentration on the sintering curve and shrinkage rate of GDC10, measured at 10°C · min^{-1} in Ar atmosphere.

Each dopant employed shows an influence on reducing the onset temperature of sintering compared to the undoped sample, which at 1300°C shrank less than 5%, barely sintering at all. The Fe and Mn-doped samples were characterized by a very slow shrinkage, achieving a maximum shrinkage rate respectively of 0.25%·min^{-1} at 1240°C and 0.3%·min^{-1} at 1100°C. Compared to Fe, the Mn-doped sample kept shrinking with an approximately constant rate between 1100 and 1300°C, recording a total shrinkage of 25% at the maximum temperature. The sample Co-doped, although started to shrink at the highest temperature (1100°C), shows a more sharp behavior, recording a maximum shrinkage rate of about 0.55%·min^{-1} at 1200°C. However, the effect of Co-doping at this concentration is considerably weak and caused a final shrinkage slightly higher than 15% at the maximum temperature reached. Among the dopants selected, Li-doping surely showed the most dramatic behavior. Sintering started at 800°C, reaching full densification below 1150°C with a shrinkage of 24% that is kept constant up to 1300°C, sign that full densification was reached. The maximum shrinkage rate was higher than for the other dopings, recording a value of 0.75%·min^{-1} at 940°C. SEM micrographs of the fracture surface of samples 1mol% Co, Fe and Mn doped after sintering for 3h at different temperatures are reported in Fig. 3.33 and compared to the pure GDC10.

From the observation of the fracture surfaces, the improved densification caused by the different dopings is clear, especially when compared to the pure sample that confirmed its difficulty to sinter[9]. The higher efficiency of the Co-doping is evident already at 1000°C and the structure shows a far more advanced stage of sintering compared to the Fe and Mn-doping, which was already observed[10]. The grain boundaries are already formed and the porosity is isolated and located at the grain corners, sign that the sintering is already in the final stage. Increasing the temperature, the Co doped powder shows mostly grain growth and the spherical pores increased in size but decreased in number.

Also the Fe and Mn-doping produced a fully dense structure after treatment at 1200°C, with large grains and few pores. Among the two, Fe performed slightly better at 1000°C, enhancing the creation of necks between the particles while for Mn at the same temperature the structure is not that far from the undoped GDC10. However, at 1100°C the Mn doped sample shows a very good densification with fine porosity which is almost completely eliminated.

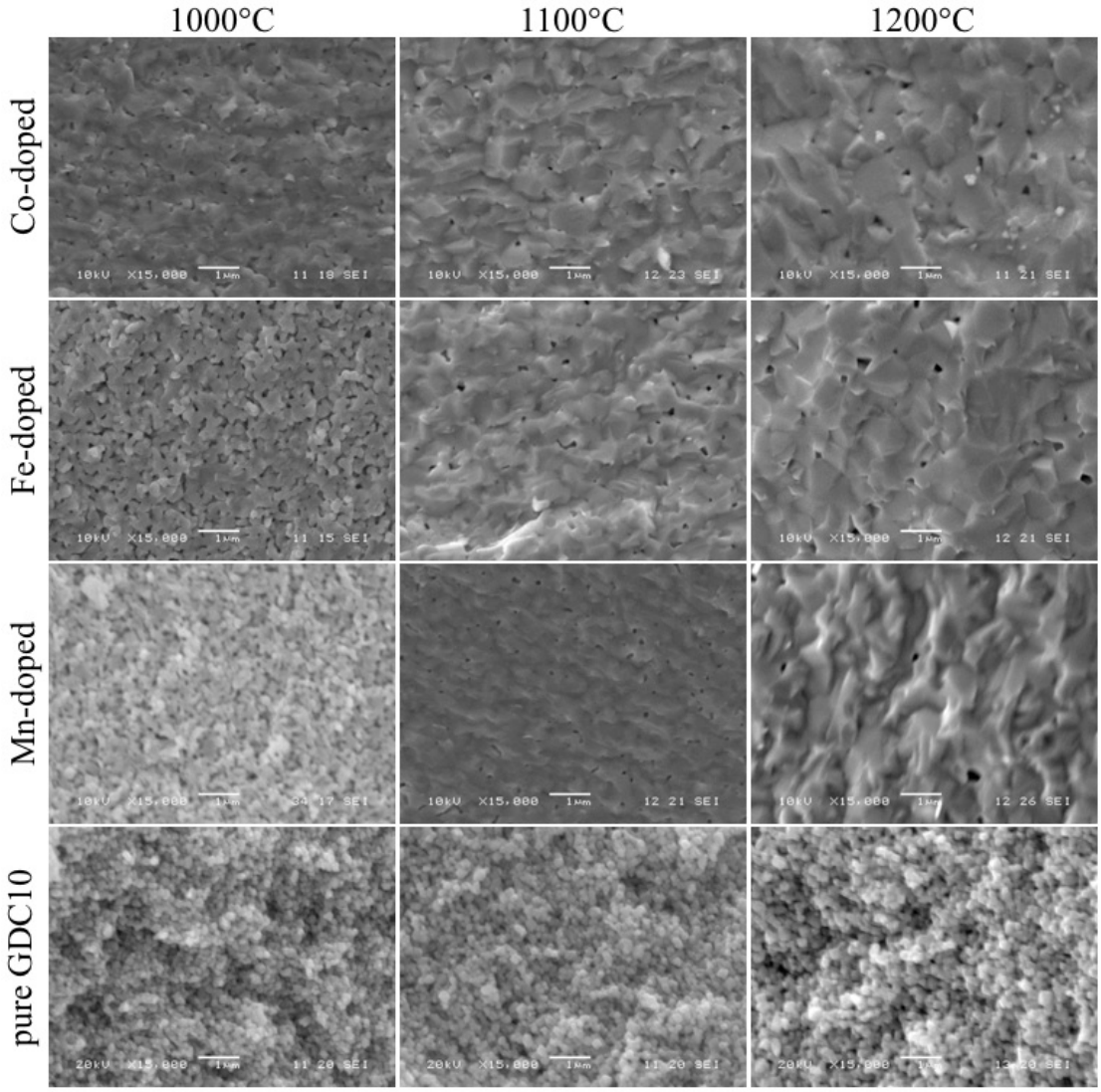

Fig. 3. Fracture surfaces of doped and undoped samples after 3h sintering in Ar atmosphere.

Although every doping analyzed, allowed reaching a high densification at reduced temperature, the effect of Li was considered more interesting because it caused a faster densification at lower temperature with a smooth and sharp curve. Then the effect of different concentration of Li_2O was studied and is reported in Fig. 4.4.

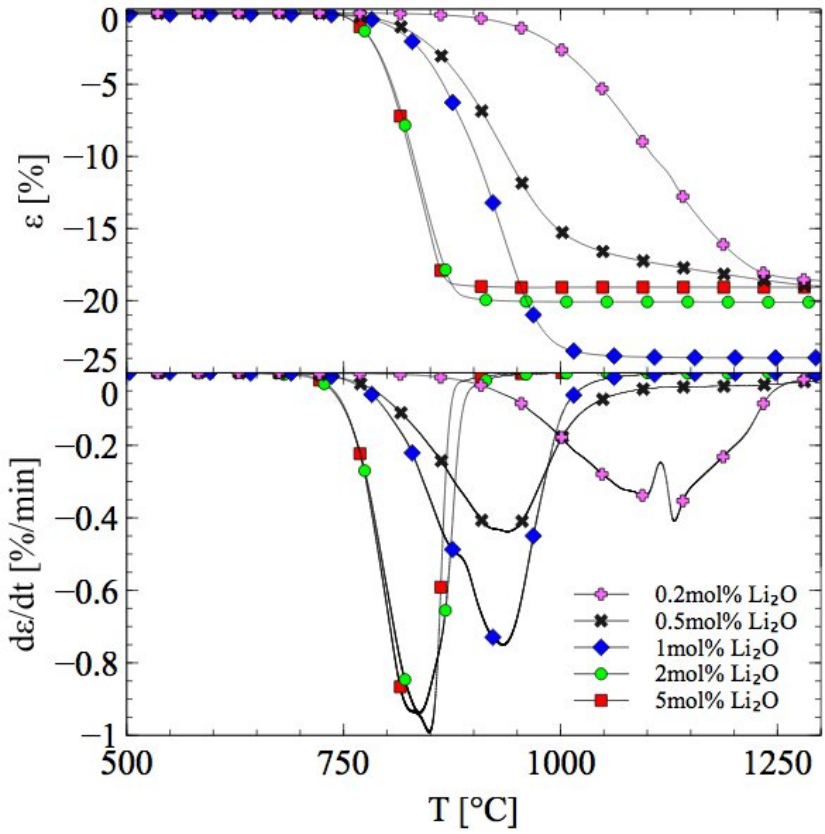

Fig. 4.4 Effect of different concentration of Li_2O-doping on the sintering curve and shrinkage rate of GDC10, measured at 10°C · min^{-1} in Ar atmosphere.

The doping concentration had an evident influence on both the maximum shrinkage rate and the temperature at which it occurred. For every doping higher than 0.2mol%, the onset of sintering is located between 750 and 800°C and every sampled reached maximum densification below 1250°C. Doping with 2 and 5mol% was very effective, completing the sintering below 900°C, almost 600°C below the sintering temperature of pure GDC10 and confirming the extreme usefulness of lithium as sintering aid. Increasing the doping concentration caused also a progressively faster sintering, reaching values down to 0.9%·min^{-1} and 1%·min^{-1} respectively for 2 and 5mol% Li-doping. Temperatures relative to the maximum shrinkage rates were also decreased by increasing the doping concentration, passing from 1120°C for the 0.2mol% to 850°C for the 2 and 5mol%. The curves relative to 2 and 5mol%, except from a slightly faster densification for the latter, are almost overlapping, sign that the effect of doping reached saturation for 2mol% and can be hardly further improved. The maximum shrinkage rates are reported in Fig. 4.5 together with the relative densities reached by the doped samples after 1h sintering at 900°C.

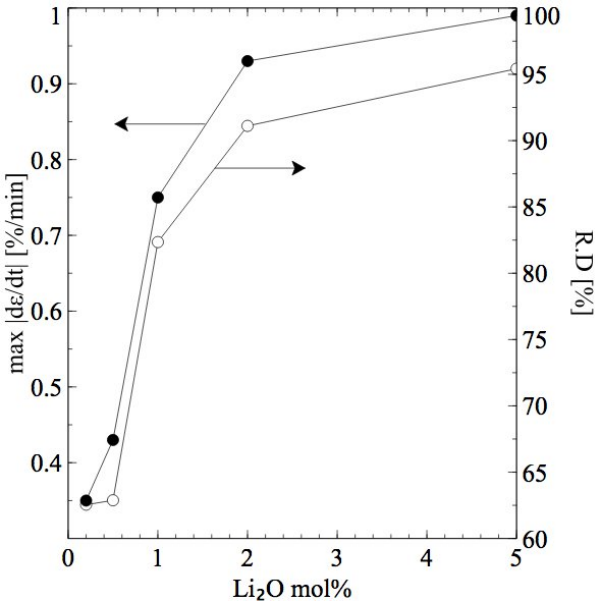

Fig. 4.5 Maximum shrinkage rates from Fig. 4 and relative density of Li_2O doped samples sintered 1h at 900°C in Ar atmosphere.

Both the maximum shrinkage rate and the final relative density after sintering, follow the same trend, experiencing the largest variation between 0.5 and 2mol% doping. A fully dense material with relative density superior to 95% was obtained by doping with 5mol% Li_2O and sintering at 600°C below than the conventional sintering temperature for GDC10. The saturation for dopings higher than 2mol% is evident in both plots. In particular for the relative density, an increase from 2 to 5mol% increased the relative density of just 5%. The SEM micrographs of the fracture surface of samples doped with 0.5, 1 and 2mol% Li_2O and sintered at 900°C for 3h are reported in Fig. 4.6. The undoped sample sintered for 3h at 1500°C is given for comparison.

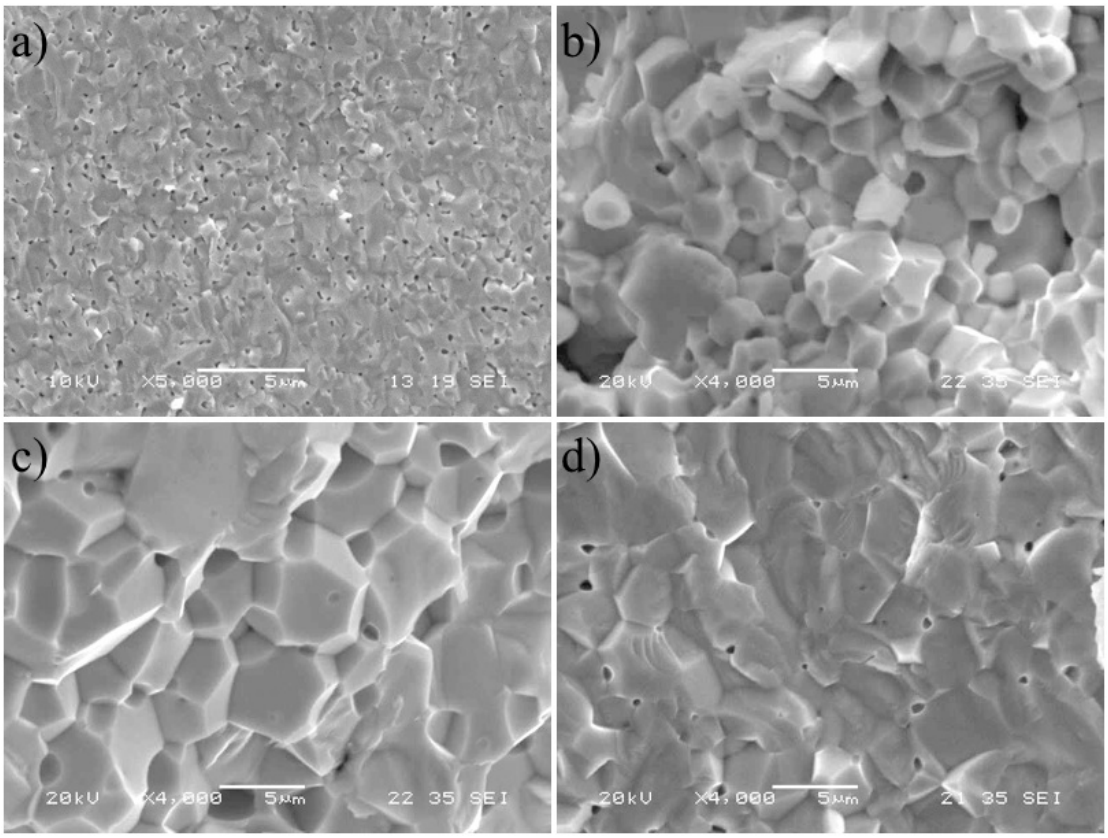

Fig. 4.6. Fracture surfaces of pure GDC10 sintered at 1500°C for 3h (a). Lithium doped GDC10 with 0.5mol% (b), 1mol% (c) and 2mol% (d) Li_2O sintered at 900°C for 3h.

Considered that the Li doped samples reported in Fig. 4.6 were sintered at 100°C below than the minimum sintering temperature for the other dopants and 600°C below than the sintering temperature of the undoped GDC10, the effect of lithium as sintering aid is surely remarkable. At 1500°C GDC10 reached almost complete densification, with small grains and fine and diffuse spherical porosity. The Li-doping at 0.5mol% was already sufficient to induce a large growth of the GDC10 grains. The porosity is closed and isolated at the corners of the grains characterized by tetrakaidecahedral shape, sign that the densification is completed and the sintering is in its intermediate stage[11]. Increasing the doping concentration, the porosity is progressively removed and the grains became bigger. For the 2mol% doped sample, the pores are almost completely filled and the structure reached maximum density.

Considering the possibility of employing Cu_2O as precursor oxide for the metallic phase, and the requirement of sintering in non-oxidative atmosphere to avoid its further oxidation, every analysis performed so far was accomplished using high-purity Ar flux. However, the effect of the atmosphere on the behavior induced by the doping with Li_2O was further investigated and the results are reported in Fig. 4.7.

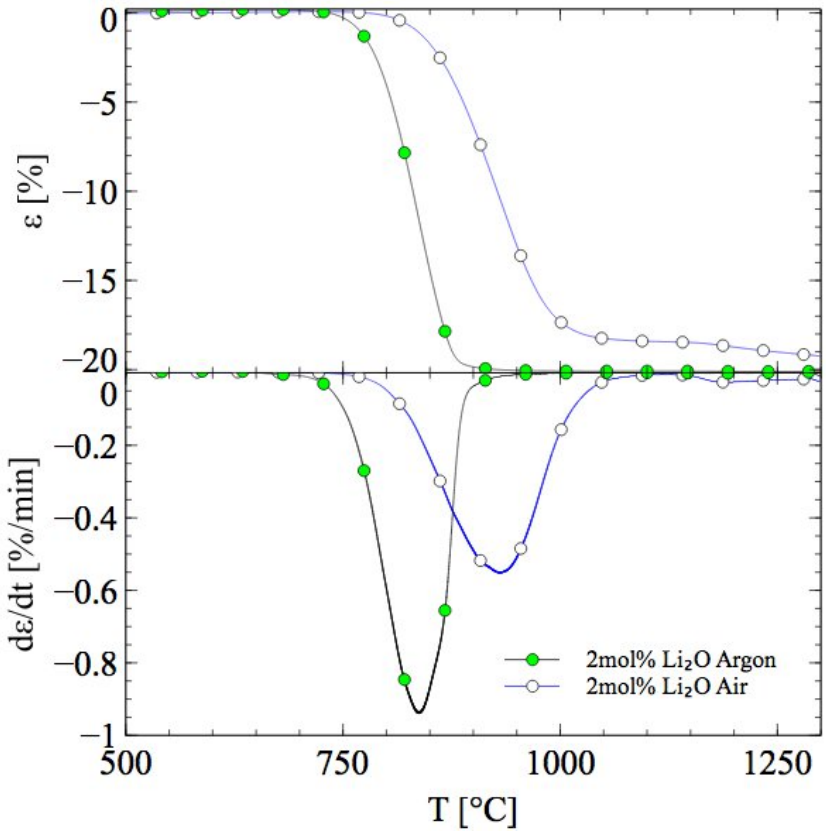

Fig. 4.7 Influence of the sintering atmosphere on the shrinkage and shrinkage rate for 2mol% Li-doped samples, measured at 10°C · min^{-1}.

The influence of the atmosphere is considerable. Additionally from decreasing by almost 100°C the beginning of densification, sintering in Ar is clearly more rapid. The maximum shrinkage rate is lower in Ar by 0.35%·min^{-1}. Also the temperature at which the maximum rate decreased significantly, recoding a reduction of more than 100°C when sintering in non-oxidative atmosphere. This behavior, and the effects promoted by doping with sintering aids cannot be further clarified without a discussion about the mechanism of activated sintering proposed in literature.

4.4 Discussion

The effect of the sintering aids and the reason for which only certain elements can enhance the sinterability for a specific material, is not completely clarified in literature. Sintering of nanometric powders occurs through a flux of atoms diffusing primarily along grain-boundary (g.b.) instead of across the lattice[12]. Then to understand the effect of the sintering aids, it is appropriate to analyze their influence on the flux of atom along the grain boundary:

$$J = MC\nabla\mu \qquad (4.1)$$

Where J is the flux, M is the atomic mobility and C is the vacancy concentration. $\nabla\mu$ is the gradient in chemical potential between the particle necks and their free surface, i.e. the driving force for sintering[11].

The sintering aids increase the sinterability of a material by altering one or more of these terms[7]. The mechanisms recognized in literature for which this happens can be several. For example, the formation of a liquid phase at the grain boundary, other than allowing for a more efficient packing of powder during the initial step of sintering, increases the driving force for sintering due to capillary effects[13].

The dopant substitution in the near g.b., could have an influence both on the mobility and the vacancy concentration, especially if the dopant has different charge and/or size compared to the host cation[14]. The dopant segregation at the grain boundary could alter M by scavenging Si_2O impurities[15].

For a dopant to be effective as sintering aid, it must segregate at the grain boundary instead of dissolving in the bulk of the material. Hence the solubility of the dopant in the host material can be taken as a discriminating parameter for evaluating its feasibility. The solubility of a dopant in CeO_2 is inversely proportional to the square of its "Vegard's Slope", which is defined as:

$$X = (0.0220r_i + 0.00015z_i) \qquad (4.2)$$

Where r_i is the difference in ionic radii between the dopant and the host cation in 8-fold coordination and z_i is the difference in charge between the dopant and the Ce^{4+}. Atoms with a small modulus of Vegard's slope have high solubility in the material and are more likely to diffuse in the ceria without having relevant effects on the sintering mechanism. Those characterized by a large value, are less soluble in the host lattice and can form a beneficial liquid phase at the grain boundary. If this happens, the atoms can move more easily in a liquid than through a solid thus leading to an increase in diffusion rate. If, however, the value is too large, the second phase at the g.b. might be completely insoluble for the ceria atoms, preventing their diffusion and forcing the system to sinter through the conventional and less effective solid state sintering mechanism observed for the pure material[16]. Then, the dopants that are more likely to induce a faster densification of the ceramic are those with moderate absolute value of their Vegard's slope.

In addition to giving information about the solubility, the Vegard's slope might also indicate which dopant can increase the grain boundary atom flux by creation of additional oxygen vacancies. CeO_2 is a prototypical fluorite-structured oxide (see section 1.2.1 Electrolytes) where every Ce^{4+} is coordinated with 8 oxygen atoms. Since oxygen vacancies form very readily in this structure[17], oxygen diffusion is very fast in Ce_2O and similar oxides. Therefore

the cations are the rate-limiting species for diffusion occurring during sintering. Cations diffuse in the material thanks to the presence of defects that, in pure Ce_2O, can be Frenkel or Schottky type. The defect formation equations, written in the Kröger-Vink notation, are:

$$\text{null} \overset{\Delta G_S}{\longleftrightarrow} V_{Ce}'''' + 2V_o^{\cdot\cdot} \tag{4.3}$$

$$\text{null} \overset{\Delta G_F}{\longleftrightarrow} V_{Ce}'''' + Ce_i^{\cdot\cdot\cdot\cdot} \tag{4.4}$$

Where ΔG is the Gibbs free energy of formation of a Schottky defect (S) or a Frenkel defect (F). Then the concentration of Ce^{4+} vacancies produced by a Frenkel defect is:

$$[V_{Ce}''''] = [Ce_i^{\cdot\cdot\cdot\cdot}] K_F \exp\left(-\frac{\Delta G_F}{kT}\right) \tag{4.5}$$

For Schottky type defect:

$$[V_{Ce}''''] = [V_o^{\cdot\cdot}]^{-2} K_S \exp\left(-\frac{\Delta G_S}{kT}\right) \tag{4.6}$$

Where K_F and K_S are the preexponential, temperature independent factors of the reaction constant of Eq. 4.3 and 4.4, respectively. Substituting Eq. 4.5 in Eq. 4.6, the following equation can be obtained:

$$[Ce_i^{\cdot\cdot\cdot\cdot}] = [V_o^{\cdot\cdot}]^2 \frac{K_F}{K_S} \exp\left(-\frac{\Delta G_F - \Delta G_S}{kT}\right) \tag{4.7}$$

Then the concentration of interstitial Ce^{4+} is proportional to the square of the concentration of oxygen vacancy in the lattice. Considering that for CeO_2, and other oxides with fluorite type lattice, cation diffusion occurs more likely through interstitial defects[14], the Ce^{4+} mobility along the grain boundary can be altered by modifying the oxygen vacancy concentration.

Doping with cations with smaller radius, less charged or both, means increasing the oxygen vacancy concentration due to charge compensation and the preference of undersized dopant to coordinate with fewer than 8 oxygen atom. Instead, doping with atoms with larger size or more charged leads to a decrease in oxygen vacancy concentration and thus the Ce^{4+} g.b. mobility, decreasing the sinterability of the material. Thus, dopants with a positive Vegard's slope, which are oversized, electron donating or both, should decrease the solid-state sintering temperature. Dopants with a negative value, undersized, electron accepting or both, will have the opposite effect.

In summary the Vegard's slope is a powerful criteria to evaluate the effectiveness of a dopant to induce low temperature sintering in GDC10 through either liquid phase sintering or heterogeneous doping. Among the possible dopants, the most effective as sintering aids were found[7] to have a Vegard's slope ranging between -45 and -58. In Tab. 4.1 the values of the Vegard's slope for the atoms used in this study are reported. Their belonging to the identified range confirms that the mechanism that they induce during sintering are the same of those previously proposed. It is not clear why one might perform better than another. It might be noticed that the more effective Co and Li doping have lower valence than Mn and Fe, thus leading to the creation of more oxygen vacancies for charge neutrality. However this has not been proved and their efficacy is still left to empirical evaluation.

Tab. 4.1 Vegard's slope of the dopants analyzed.

	8-fold coordinated ionic radius (A)	Vegard's slope ($x10^5$)
Mn^{3+}	0.78	-58
Fe^{3+}	0.78	-57
Co^{2+}	0.90	-45
Li^{+}	0.92	-56

The effect of the sintering atmosphere on the sintering behavior represented in Fig. 4.7 can be explained following the same arguments. In fact, sintering in a less oxidizing atmosphere led to the creation of more oxygen vacancies that, in turn, increased the concentration of interstitial cation defects and, thus, increased the mobility along the grain boundary. This behavior was already noticed for the undoped CeO_2[14], and never before for the doped material.

Finally, several studies have been carried out to analyze the effect of the sintering aids on the conductivity of electrolytic materials. On this topic, the opinions in literature are still considerably scattered. To be effective as sintering aids, the dopant must be located at the grain boundary (GB) during sintering. Depending on the maximum temperature reached during sintering, a particular dopant can diffuse inside the lattice[18], stay at the grain boundary[19] or, in case of high vapor pressure, even evaporate[7]. In one case of lithium doping of SDC, any new phase or structural change in the host lattice was observed by XRD or Raman spectroscopy sign that no diffusion in the lattice occurred at any temperature. And this was confirmed by the unchanged bulk conductivity measured on doped and un-doped samples[18]. The total conductivity of GYDC was measured after sintering at 1400°C and compared to the 1.5mol% and 3mol% $LiNO_3$ doped materials sintered at 800°C achieving the same results between

450 and 700°C[20]. In another study, the grain boundary conductivity of 5mol% Li_2O-doped GDC samples sintered at 800°C was even better than the un-doped sample[19]. And this was explained by the decrease of the Schottky barrier height caused by the aliovalent substitution of Ce^{4+} with Li^{1+} at the GB. Another work recorded better lattice conductivity because of the role of acceptor dopant in GDC giving rise to a high vacancy concentration, but worst grain boundary conductivity due to dopant segregation[21].
However, they all agree that the promoted grain growth is beneficial. In fact, the grain boundary conductivity is two orders lower than the lattice conductivity in an oxygen ion conductor and bigger grains translate into thinner and fewer grain boundaries to cross for the diffusing oxygen vacancies[22,23].

4.5 Conclusion

The enhanced sinterability of GDC10 promoted by the doping with sintering aids was studied with particular attention to the Li_2O doping. A fully dense material with relative density superior to 95% was obtained by sintering at 900°C, 600°C below the sintering temperature of pure GDC10, by doping with 2mol% of Li_2O. Their effect was discussed on the base of the mechanisms of activated sintering proposed in literature. Thanks to the reduction induced on the GDC10 sintering temperature, lithium doping was considered as the most promising to allow the full densification of the electrolyte at co-sintering temperatures compatible with the permanence of the copper oxides in the cermet supporting anodes.

References

1. Brett, D. J. L., Atkinson, A., Brandon, N. P. & Skinner, S. J. Intermediate temperature solid oxide fuel cells. *Chem. Soc. Rev.* **37**, 1568 (2008).
2. Gerhardt-Anderson, R. Ionic conductivity of CeO2 with trivalent dopants of different ionic radii. *Solid State Ionics* (1981).
3. Kuharuangrong, S. Ionic conductivity of Sm, Gd, Dy and Er-doped ceria. *Journal of Power Sources* (2007).
4. Muthukkumaran, K., Kuppusami, P., Mohandas, E., Raghunathan, V. & Selladurai, S. Ionic conductivity measurements in gadolinia doped ceria. *International Symposium of Research Students on Material Science and Engineering, Chennai (ISRS)* 1–8 (2004).
5. Inaba, H., Nakajima, T. & Tagawa, H. Sintering behaviors of ceria and gadolinia-doped ceria. *Solid State Ionics* **106**, 263–268 (1998).
6. Neumann, J., Zhong, T. & Chang, Y. The Cu– O (Copper-Oxygen) system. *Journal of Phase Equilibria* **5**, 136–140 (1984).
7. NICHOLAS, J. & DEJONGHE, L. Prediction and evaluation of sintering aids

for Cerium Gadolinium Oxide. *Solid State Ionics* **178**, 1187–1194 (2007).
8. Fu, C. J., Liu, Q. L., Chan, S. H., Ge, X. M. & Pasciak, G. Effects of transition metal oxides on the densification of thin-film GDC electrolyte and on the performance of intermediate-temperature SOFC. *Int J Hydrogen Energ* **35**, 11200–11207 (2010).
9. Reddy, K. R. & Karan, K. Sinterability, mechanical, microstructural, and electrical properties of gadolinium-doped ceria electrolyte for low-temperature solid oxide fuel cells. *J Electroceram* **15**, 45–56 (2005).
10. Jud, E., Huwiler, C. B. & Gauckler, L. J. Sintering Analysis of Undoped and Cobalt Oxide Doped Ceria Solid Solutions. *J Am Ceram Soc* **88**, 3013–3019 (2005).
11. Rahaman, M. *Ceramic processing and sintering*. (2003).
12. Herring, C. Effect of Change of Scale on Sintering Phenomena. *J. Appl. Phys.* **21**, 301 (1950).
13. Jud, E., Zhang, Z., Sigle, W. & Gauckler, L. Microstructure of cobalt oxide doped sintered ceria solid solutions. *J Electroceram* **16**, 191–197 (2006).
14. Chen, P.-L. & Chen, I.-W. Grain growth in CeO2: dopant effects, defect mechanism, and solute drag. *J Am Ceram Soc* **79**, 1793–1800 (1996).
15. Zhang, T. Iron oxide as an effective sintering aid and a grain boundary scavenger for ceria-based electrolytes. *Solid State Ionics* **167**, 203–207 (2004).
16. Kingery, W. Densification during sintering in the presence of a liquid phase. I. Theory. *J. Appl. Phys.* (1959).
17. BLUMENTHAL, R. & Sharma, R. Electronic conductivity in nonstoichiometric cerium dioxide. *Journal of Solid State Chemistry* (1975).
18. Li, S. *et al.* Feasibility and mechanism of lithium oxide as sintering aid for Ce0.8Sm0.2Oδ electrolyte. *Journal of Power Sources* **205**, 57–62 (2012).
19. Han, M., Liu, Z., Zhou, S. & Yu, L. Influence of lithium oxide addition on the sintering behavior and electrical conductivity of gadolinia doped ceria. *Journal of Materials Science & Technology* **27**, 460–464 (2011).
20. Zhang, L., Lan, R., Cowin, P. I. & Tao, S. Fabrication of solid oxide fuel cell based on doped ceria electrolyte by one-step sintering at 800°C. *Solid State Ionics* **203**, 47–51 (2011).
21. Esposito, V., Zunic, M. & Traversa, E. Improved total conductivity of nanometric samaria-doped ceria powders sintered with molten LiNO3 additive. *Solid State Ionics* **180**, 1069–1075 (2009).
22. Souza, E. C. C., Chueh, W. C., Jung, W., Muccillo, E. N. S. & Haile, S. M. Ionic and Electronic Conductivity of Nanostructured, Samaria-Doped Ceria. *J Electrochem Soc* **159**, K127 (2012).
23. Avila-Paredes, H. J., Choi, K., Chen, C.-T. & Kim, S. Dopant-concentration dependence of grain-boundary conductivity in ceria: A space-charge analysis. *J. Mater. Chem.* **19**, 4837 (2009).

5. Fabrication and co-sintering of SOFCs with Cu_2O-GDC cermet anode*

Abstract

The present chapter describes the fabrication of tubular Cu_2O-based cermet anode supported SOFCs half-cell with a dense and crack free GDC10 electrolyte in one step co-sintering. Dilatometric analysis was performed on different anode preparations to study the effects of the Cu_2O:GDC10 ratio and the effects of different quantities of Li_2O doping amounts on the sintering behavior. The densification of the electrolyte, deposited on the green anodes by dip coating, was analyzed after co-sintering on anodes with different compositions. Issues related to lack of densification during sintering and cracking of the electrolyte during cooling are discussed. A complete cell composed of Cu_2O - (GDC10 - Li_2O doped) cermet anode, GDC10 - Li_2O doped electrolyte and LSF20 – GDC10 cathode was realized in one-step co-sintering at 995°C.

Keywords: Cu_2O-based cermet, Co-sintering, Constrained sintering, Residual stress.

5.1 Introduction

The issues of carbon deposition that arise in Solid Oxide Fuel Cell (SOFC) anodes when switching from H_2 to carbon-based fuels like methane have been clearly established[1]. Despite large efforts, this issue still remains[2]. In state-of-the-art nickel-yttria stabilized zirconia (Ni-YSZ) cermet anodes, the metallic Ni phase serves as an electronic conductor and as a catalyst for the oxidation of H_2 at the triple phase boundary (TPB) allowing for reduced cell operating temperatures around 700°C. When switching to carbon-based fuels, the Ni does not effectively catalyze the oxidation of carbon resulting in the eventual deposition of coke in the anode and the eventual loss of cell performance as the TPBs are covered[3]. Careful selection of steam to gas ratios and current densities have proved to be beneficial[4,5], but the substitution of nickel with a metal immune to carbon deposition appears to be the more direct and immediate solution.

* *Part of this chapter has been submitted to the* "Journal of the European Ceramic Society" *with the title: "Fabrication and co-sintering of tubular IT-SOFCs with Cu_2O-GDC cermet supporting anode and Li_2O doped GDC electrolyte".*

Among the possible candidates, the choice is restricted to elements belonging to IB and VIIIB groups because less noble metal would oxides too easily in presence of steam. Fe and Co both catalyzes carbon formation[6] while Pt, Rh and Pd have both excellent catalytic activity and resistance to coking but they are too expensive to be feasible. Au and Ag have excellent conductivity but the former is still too expensive while the latter has practical problems due to its low melting point (920°C). After Ag, Cu is the most conductive metal existing ($5.96 \cdot 10^5$ $S \cdot cm^{-1}$), is cheaper and has lower electrical resistivity than Ni and, more importantly, is more inert to carbon deposition and coke formation[7]. Copper is then one of the most promising alternatives[8].

Several issues arise when substituting Ni with Cu. Most importantly, the low melting temperature of copper and both of its oxides strongly limits their employment. These low melting temperatures prevent the direct inclusion of either oxide in the supporting anodic cermet prior the conventional high temperature sintering treatment (>1300°C), as is common practice with NiO based cermets.

To avoid subjecting the copper oxide to the high sintering temperatures, several approaches have been proposed such as infiltration of metal salt solutions in a pre-sintered porous ceramic scaffolds[9-14], plasma spraying[15] and electroplating[16,17]. Although many of these approaches show good functionality and performance, the possibility of including copper in the supporting cermet at the point of its initial formulation can constitute a valid and timesaving alternative.

The low melting temperature of Cu (1083°C) also means that once reduced, cell operating temperature must be limited to prevent the coarsening of the Cu phase which would result again in decreased cell performance. Due to this, Cu-based anodes are suitable for operations at temperatures less than 700°C. In this temperature range the material used for the state of the art electrolyte, yttria stabilized zirconia (YSZ), does not have a satisfactory ionic conductivity causing high resistive losses in the cell.

Gadolinia doped ceria (GDC) is a very promising electrolytic material for intermediate temperature fuel cells (IT-SOFCs) because of its high ionic conductivity between 500 and 700°C[18-20]. However one of the most significant problems related to its use, is the need of high sintering temperatures (>1500°C) to obtain the required density to have a gas tight electrolyte (>95% r.d.). The employment of sintering aids can decrease the sintering temperature and increase the densification rate of GDC. In particular the addition of lithium oxide (Li_2O) has shown to be the most efficient[†].

Finally, if a Cu-GDC anode is to be co sintered with a GDC electrolyte, the main issue that arises is the low coefficient of thermal expansion (CTE) of Cu oxides. These CTE differences will cause high thermal stresses to form and the failure of

[†] *For a complete discussion about Sintering Aids see Chapter 4.*

the electrolyte and the loss of its gas impermeability. In case of NiO, its CTE is similar to both YSZ and GDC so its presence during sintering is of little note[21]. The state of the art anode generally has a CTE higher than both the electrolyte and the cathode ($CTE_{NiO}=14.1\cdot10^{-6}/°C$)[21], meaning that during the cooling phase of the sintering process, these two layers are subjected to residual compressive stresses, which are beneficial to avoid cracking of the electrolyte. Copper (I) oxide, Cu_2O, has a CTE of $4.3\cdot10^{-6}/°C$ [22] and GDC10 of $\sim13.4\cdot10^{-6}/°C$ [23], so the cermet anode has necessary a CTE lower than the other layers of the cell. Consequently, during cooling the electrolyte experiences a tensile stress state and the opening of cracks in the electrolyte is a serious eventuality that can be avoided by careful selection of the copper content in the anode.
The present work describes how to fabricate tubular Cu_2O-based cermet anode supported SOFC half-cells with a dense and crack free GDC10 electrolyte in one step co-sintering. The anode support was fabricated by extrusion and the electrolyte deposited by dip coating. Dilatometric analysis was performed on different anode preparations to study the effects of the Cu_2O:GDC10 ratio and the effects of different quantities of Li_2O doping amounts on the sintering behavior. The densification of the electrolyte, deposited on the green anodes by dip coating, was analyzed after co-sintering on anodes with different compositions. Issues related to lack of densification during constrained sintering and cracking of the electrolyte during cooling are also described and discussed.

5.2 Experimental

A 10 mol% gadolinia doped ceria (GDC10) sub-micron powder (Treibacher Industrie AG, $d_{50}=0.27\mu m$, $d_{90}=0.40\mu m$ and $SSA=9.10 m^2/g$) was used in the preparation of both the anode pastes and the electrolyte suspensions. Cu_2O powder (<5µm, 97%, Sigma Aldrich) and Hydroxy-propyl-methyl-cellulose (HPMC, average Mn~90.000, Sigma Aldrich) used as binder for extrusion, were purchased from Sigma-Aldrich.
Doping of the GDC10 used for the anode was accomplished by dissolving the suitable quantity of lithium nitrate ($LiNO_3$) in ethanol by stirring and then by slowly adding the GDC10 powder. The dispersion was kept stirring on a hot plate at 90°C until complete evaporation of the ethanol. The powder was further dried at 100°C overnight and then ground and sieved (mesh size 425µm) to eliminate the largest agglomerates. The obtained $LiNO_3$-doped powder was not calcined prior to paste formulation; instead, calcinations took place during co-sintering.
The solid phase of the extrusion paste was produced by mixing in PE bottle $LiNO_3$-doped GDC10, Cu_2O and HPMC. Depending on the solid loading desired, the appropriate quantity of de-ionized water was weighed and added to the dry powders all at once. Mixing of the solid and liquid phase was carried out using a

vertical mixer with a kneading shaft until a uniform paste was obtained (3-5min). The so obtained paste was then loaded into the ram extruder from below, to reduce the air entrapment inside the barrel. The extruder was then mounted on a specifically designed frame[24] for the Material Testing Machine (MTS) that was used to supply the force necessary to the extrusion and to monitor the extrusion pressure using the load cell in contact with the piston. After a dwell of 1 min at 450N, to consolidate the paste and to eliminate some air entrapped in the barrel, the piston speed was kept constant at 6mm/min, and the extrusion pressure was recorded. The tube where extruded with a die and spider measuring respectively 5 and 4mm of diameter (Fig. 5.1).

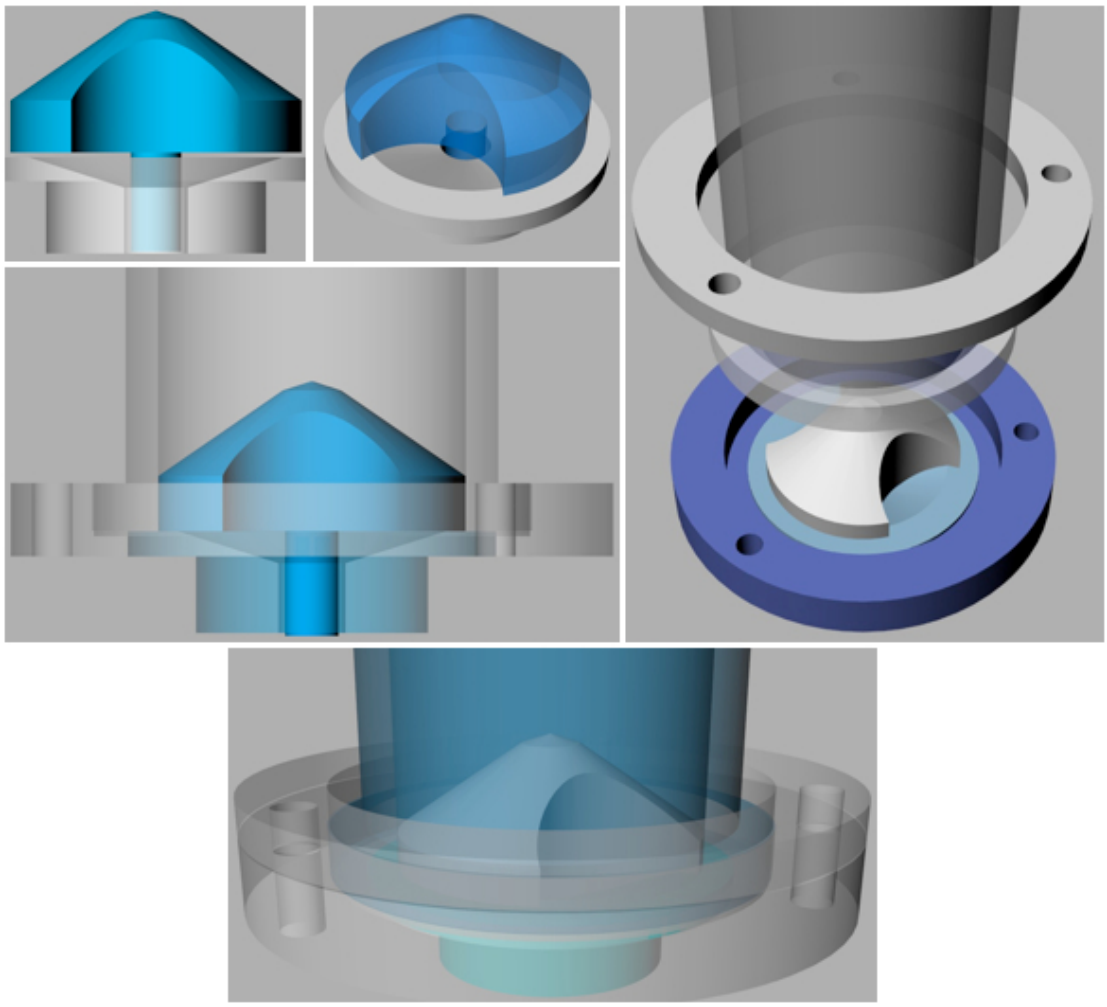

Fig. 5.1 Technical drawings of the spider-die system for extrusion of tubular supports.

The extruded tubes were cut in segments measuring ~150mm and placed in the groves of a specifically designed sponge in polyurethane. The tubes were slowly dried to avoid bending and distortion due to non-uniform drying by keeping them in a sealed container with water vapor for one hour. Then the lid was opened until the temperature and the humidity matched with the surroundings. The samples were then put in a dessicator and then at 100°C overnight. Dry

tubes were then cut in segment ~40mm long and stored in a dessicator until further use. The different paste compositions are shown in Tab. 5.1.

Tab. 5.1 Composition of the extruded anodes studied in this work.

		Rn1	Rn3	Rn4	Rn5	Rn6	Rn7	Rn8
Solid loading [vol%]		64	63	62	61	60	58	57
Solid phase composition [vol%]	GDC10-Li_2O doped	40	50	55	60	65	70	75
	Cu_2O	60	50	45	40	35	30	25
HPMC [wt% of H_2O]		2	2	2	2	2	2	2
CTE [$°C^{-1}$]		9.21	10.1	10.51	10.89	11.26	11.61	11.95

Deposition of electrolytic and cathodic layers was achieved by dip-coating the anode tubes in organic ink-based slurries. The ink was produced by dissolving 1wt% Ethyl-cellulose (EC viscosity 10cP, 5wt% in toluene/ethanol 80:20,Sigma Aldrich) in α-terpineol (mixture of isomers, ≥96%, MW: 154.25 g/mol, Sigma Aldrich) by stirring on a 90°C heating plate until the EC was fully dissolved. Lithium nitrate doping of the GDC10 (0-2mol%) was achieved by dissolving the required amount of $LiNO_3$ in ethanol, then adding the GDC10 and milling 3h with zirconia milling balls. The dispersion was then added to the amount of ink required to achieve a solid loading of 40wt%, based on only the GDC10 mass and stirred on a hot plate at 70°C until the ethanol was completely evaporated. Considering that the vapor pressure of α-terpineol is two orders of magnitude lower than ethanol, the time required to evaporate the ethanol was considered to have little influence on the quantity of α-terpineol and the final solid loading. The electrolyte was deposited by dipping the anodes in the GDC10-$LiNO_3$ ink and withdrawing at constant speed. Speeds from 0.1 to 5 mm/sec were considered. Before co-sintering of the half-cell, the samples were dried in air for not less than 6h and then further dried at 100°C overnight. In the case of fabrication of a complete cell, the latter step was not performed and the half-cell was dipped in the cathode slurry after drying at room temperature.
The cathode was produced using lanthanum strontium ferrite ($La_{0.8}Sr_{0.2}FeO_3$, SSA=9.681 m^2/g, NexTech Materials) and GDC10 powders. These were dispersed in ethanol in equal weights proportion and milled for 3 h with zirconia balls. Doping was not required for the cathodic composition. The dispersion was added to α-terpineol to achieve a solid loading of 40 wt% and stirred on a hot plate at 70°C until complete evaporation of ethanol. The cathode layer was deposited with the same dip-coating parameters used for the electrolyte on the half-cells, previously dried overnight at room temperature. After drying at room temperature for 2-3 h, the cathode deposition was performed again, to obtain a thicker coating. After drying at room temperature, the complete cell was kept at 100°C overnight before sintering.

Apparent viscosity of the electrolytic slurry was measured using a Brookfield viscometer (Myr rotational viscometer, V2-L). The sample temperature was kept constant at 25°C. The apparent viscosity was measured by increasing the rpm from 2 to 20 and taking the value after 10 revolutions.

The sintering behaviors of green anode with different Cu_2O:GDC10 ratios and different Li_2O doping were measured by dilatometry (Linseis L75 Platinum Series, Linseis Instrument) using an alumina support tube and a constant heating rate of 10°C/min to1150°C in argon flux to avoid Cu_2O oxidation. Before every measurement the instrument chamber was evacuated and filled with argon three times to ensure no excess air was left in the chamber or in the sample pores. Measurements on the electrolyte material were performed on uniaxial pressed powder compacts applying a pressure of 100MPa for 1min.

The samples were sintered in a tubular furnace at constant heating rate of 2°C/min. A 1h dwell at 500°C was performed to allow for organic burnout. The heating was continued up to the sintering temperature, which was hold for 3h. Cooling was controlled at 5°C/min down to 700°C then free cooling. The sample holder was specifically designed for this application: alumina capillaries were used to suspend the tubular samples inside the furnace without reducing or deviating the gas flux and maximizing the removal of the volatile species produced by the decomposition of the organics. Reduction of the anodes was performed at 540°C for 2h with heating rate of 5°C/min and free cooling, fluxing at a mixture of 3% H_2 in argon.

To confirm the oxidation-reduction and melting behavior of the Cu_2O used for the anode preparations, thermogravimetry and differential thermal analysis (TG/DTA, Netzsch thermobalance STA 409) were performed with a heating rate of 10°C/min using alumina crucibles and alumina powder as reference. Analyses were performed in static air and in argon flux.

5.3 Results and discussion

The main limitation regarding the employment of copper as the conductive phase of the anodic cermet is its low melting temperature. To employ the oxide into the initial paste formulation, as it is done with NiO, one of the two copper oxides should be selected along with the sintering atmosphere condition in order to minimize complications during the cermet sintering. The stable oxide at ambient conditions is CuO. However, it decomposes to Cu_2O above 1026°C, the stable form in air above this temperature, resulting in a release of O_2 gas which

would likely result in the failure of the green structure. A supplementary source of stress in the cermet would occur from cooling down from sintering temperature, caused by the oxidation of Cu_2O to CuO, associated with a volume increase of 5%. When employing Cu_2O in the initial paste, oxidation issues at low temperatures occur it the P_{O_2} is sufficiently high. Again, this will result in a volume change, and the likely failure of the green structure. This considered, studies were done using Cu_2O in a controlled atmosphere (high-purity 99.5% argon, $P_{O_2} \sim 3.23 \cdot 10^{-4}$bar). Sintering in these condition fixes the melting point and the maximum sintering temperature to be 1230°C [25] and sintering aids must lower the GDC sintering temperature below this temperature.

Even in the controlled atmosphere, it was impossible to avoid some reduction of Cu_2O to copper metal during sintering, induced by the incomplete oxidation of the organics contained in the extrusion paste. This well-known phenomenon[26], also called carboreduction, can occur during high temperature treatments in non-oxidative atmospheres and it is an important technological problem, difficult to eliminate[27]. It can be observed from Fig. 5.2 showing the TG/DTA of Cu_2O only and in presence of 15wt% of HPMC.

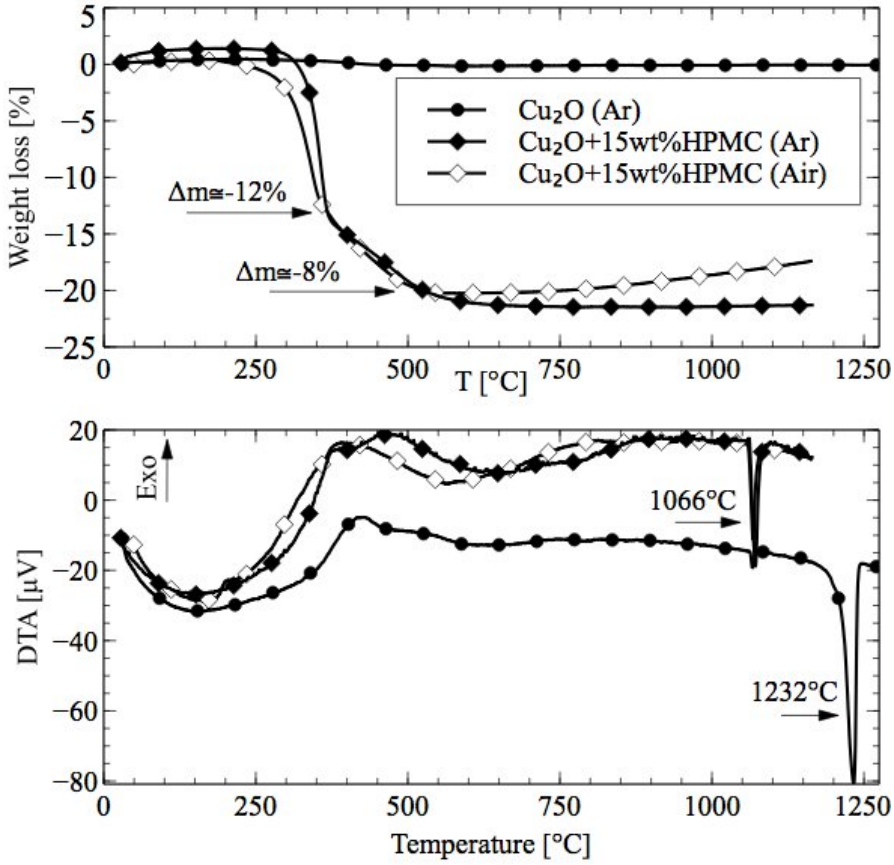

Fig. 5.2 TG/DTA measured at 10°C/min of Cu_2O only and with 15wt% of HPMC in air and Ar atmospheres.

Cu_2O is stable in argon in the whole temperature range scanned and shows an endothermic peak around 1232°C corresponding to its congruent melting[25]. When the organic binder is present, the weight loss shows two steps, the first relative to the incomplete decomposition of the organic (~12 wt%) and a second due to the carbon induced reduction of copper oxide (~8 wt%). The extra weight loss of about 5% corresponds to the reduction of about 44 wt% of the initial Cu_2O content. The Cu produced on the surface of the Cu_2O grains, forms a eutectic that melts at 1066°C[25], as indicated by the endothermic peak. The same analysis performed in air, shows the same behavior if we do not consider the successive increase in weight due to the slow oxidation of Cu and Cu_2O to CuO. The occurrence of this phenomenon even in oxidizing atmosphere, was further proof that the carboreduction of Cu_2O was a strong effect, and can not easily be avoided when preparing any pastes or suspensions with organic additives.
In Fig. 5.3, the difference between the expected and the actual weight after anode reduction is plotted against the organics wt% contained in the extrusion paste for different sintering temperatures. It can be appreciated how by increasing the organic content, more copper oxide was reduced during sintering and less was left to be reduced during the actual reduction procedure. Furthermore, this behavior was independent of the sintering temperature.

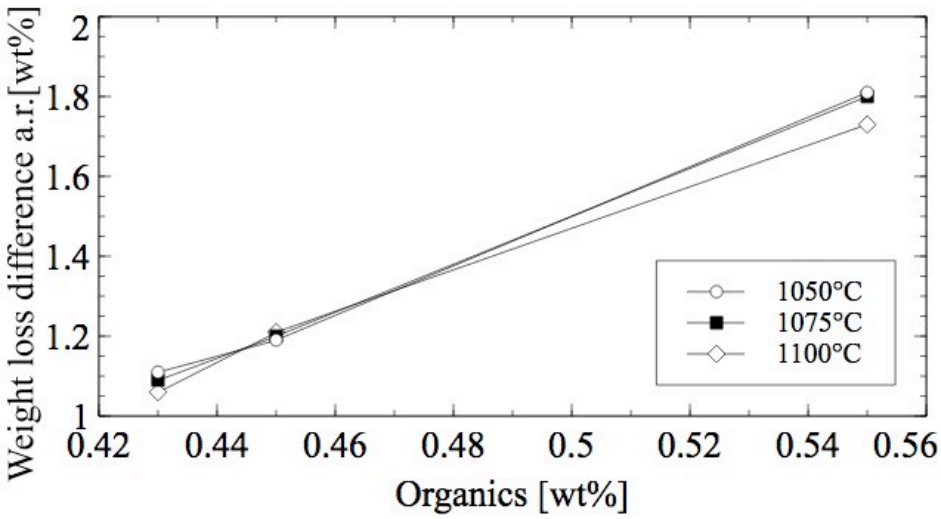

Fig. 5.3 Weight loss differences after reduction (a.r.) between theoretical and experimental values in function of the organic content and for different sintering temperatures.

Cleary the presence of a low melting eutectic during sintering represent an issue during fabrication because it limits considerably the maximum temperature that can be reached to a much lower value than the previously stated 1232°C. For sintering at temperatures higher than 1066°C, bubbles of metal were observed on the anode surface, especially in zones of the sample less exposed to the argon flux. It was also observed that the argon flux had an influence on the amount of

reduced copper oxide. This effect can be explained considering the role of the inert gas in sweeping away the incomplete decomposition products from the sample surfaces before they induce further reactions[27]. Increasing the argon flux and employing an improved sample holder where the tubular samples were suspended in the oven, directly hit by the gas flux, minimized, but not to completely eliminated, this issue until any bubbles where observed on the anodic surfaces.

The extrusion pastes were formulated with different ratios of GDC10 and Cu_2O. The binder concentration was fixed at 2wt% of the water content to obtain a liquid phase rheology independent of the solid loading. To obtain tubular samples free of defects, it was observed that the extrusion force recorded had to be between 700 and 900 N. For lower extrusion pressures, the air entrapped in the paste was not evacuated properly, leaving pinholes and imperfections on the extrudate surface. These defects are a critical aspect of the anode fabrication because if they are present during the electrolytic coating deposition, they can represent points of discontinuity in the electrolyte causing leakage during operation and a drop in performance. Extrusion pressures above this range produced a large pressure gradient along the die that induced bending and twisting of the extrudate. To extrude every composition with an extrusion force in the desired range, the solid loading was set as shown in Tab. 5.1. It can be noticed that for higher GDC10 to Cu_2O ratios, the solid loading was reduced, probably as consequence of a less efficient packing of the powders. The green anode tubes extruded following these recipes and extruded between 700 and 900 N show regular and homogenous surface, external diameter of ~5mm and constant and uniform thickness of ~500 μm.

The behavior of the cermets during sintering was analyzed as function of the Cu_2O content and the doping of the GDC10 powder. Fig. 5.4 reports the shrinkage rates for tubular cermets doped with 1 and 1.5 mol% Li_2O. The modulus of the maximum shrinkage rate increases with decreasing copper oxide content. For Cu_2O contents up to 45 vol% (Rn4) and 1 mol% Li_2O, the shrinkage rates shows two minima, the first one at about 980°C and the second at about 1080°C (Fig. 5.4a). For lower Cu_2O contents, only one principal minimum at 920°C can be identified. A similar behavior is reported for samples doped 1.5 mol% with Li_2O (Fig. 5.4b). This trend can be explained considering the cermet as formed by two powders of different particle size, a finer GDC10 and a coarser Cu_2O. In the case that the volume occupied by the Cu_2O is equal or higher than 45 vol%, sintering of GDC10 is likely retarded because the Cu2O phase starts to percolate the paste resulting in a lower amount of contact between the GDC10 particles inhibiting their ability to sinter. Then, the cermet is still shrinking when the temperature range of softening of Cu_2O is reached, causing further increase of the shrinkage rate. In case the volume occupied by the Cu_2O is lower than 45 vol%, sintering was completed at lower temperatures and the effect of the inclusion softening is not that evident except for a broadening of the sintering curves.

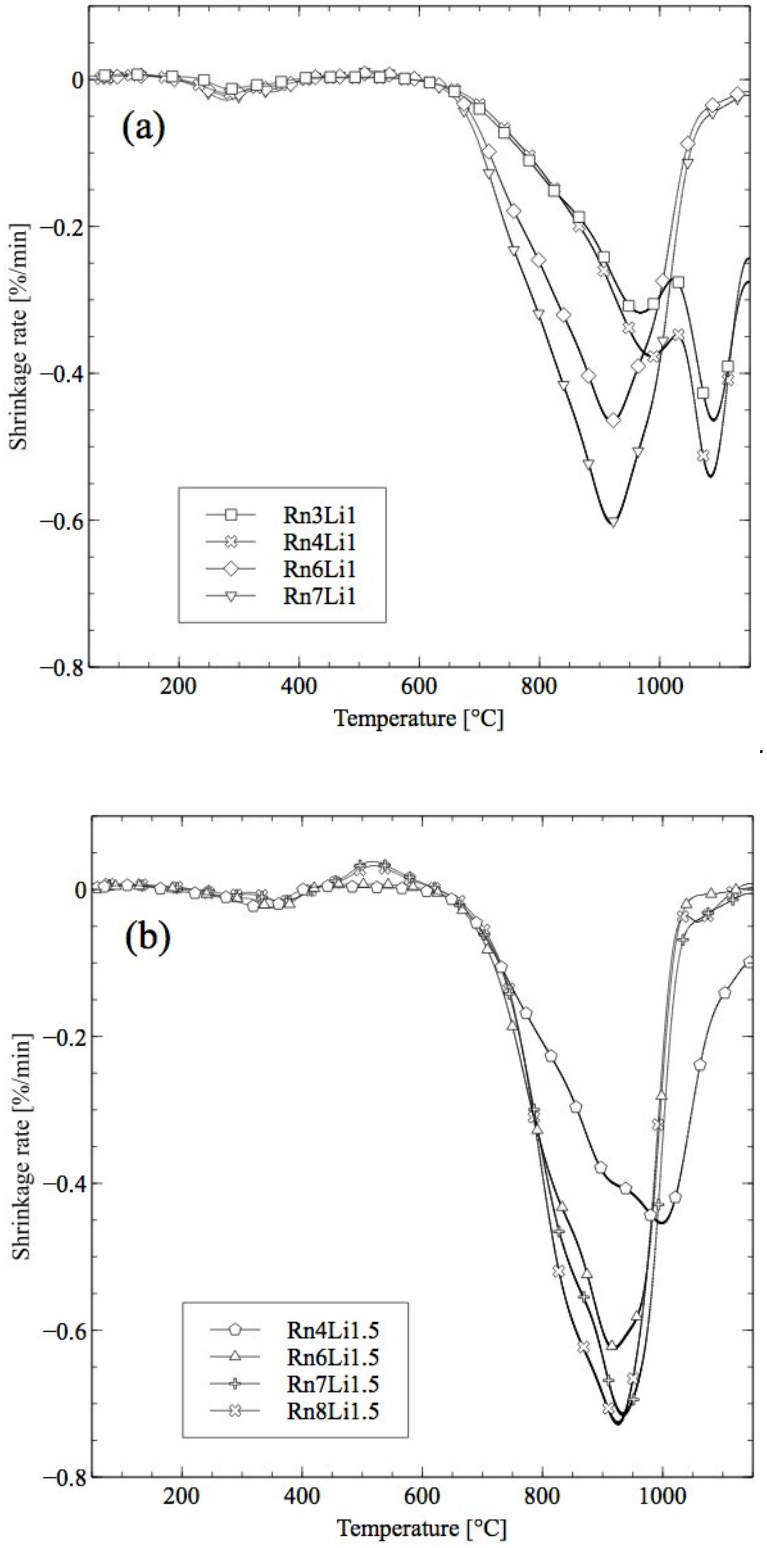

Fig. 5.4a-b Shrinkage rates of anodes with different composition and fixed GDC10 doping of 1mol% (a) and 1.5mol% (b) Li_2O.

The effect of lithium doping on Rn4 and Rn6 anodes is showed in Fig. 5.5. For both compositions, a higher doping causes an increase of the maximum shrinkage rate. The Rn4 anodes (Fig. 5.5a) with doping up to 1 mol%, exhibit the

two minima while the Rn4 1.5 mol% doped, as Rn6 with every doping analyzed (Fig. 5.5b), do not show the second minimum. As a conclusion, for Cu_2O content equal or lower than 35 vol% and doping equal or higher than 1 mol%, sintering of the cermet occurs in one regular step and it is completed below 1100°C.

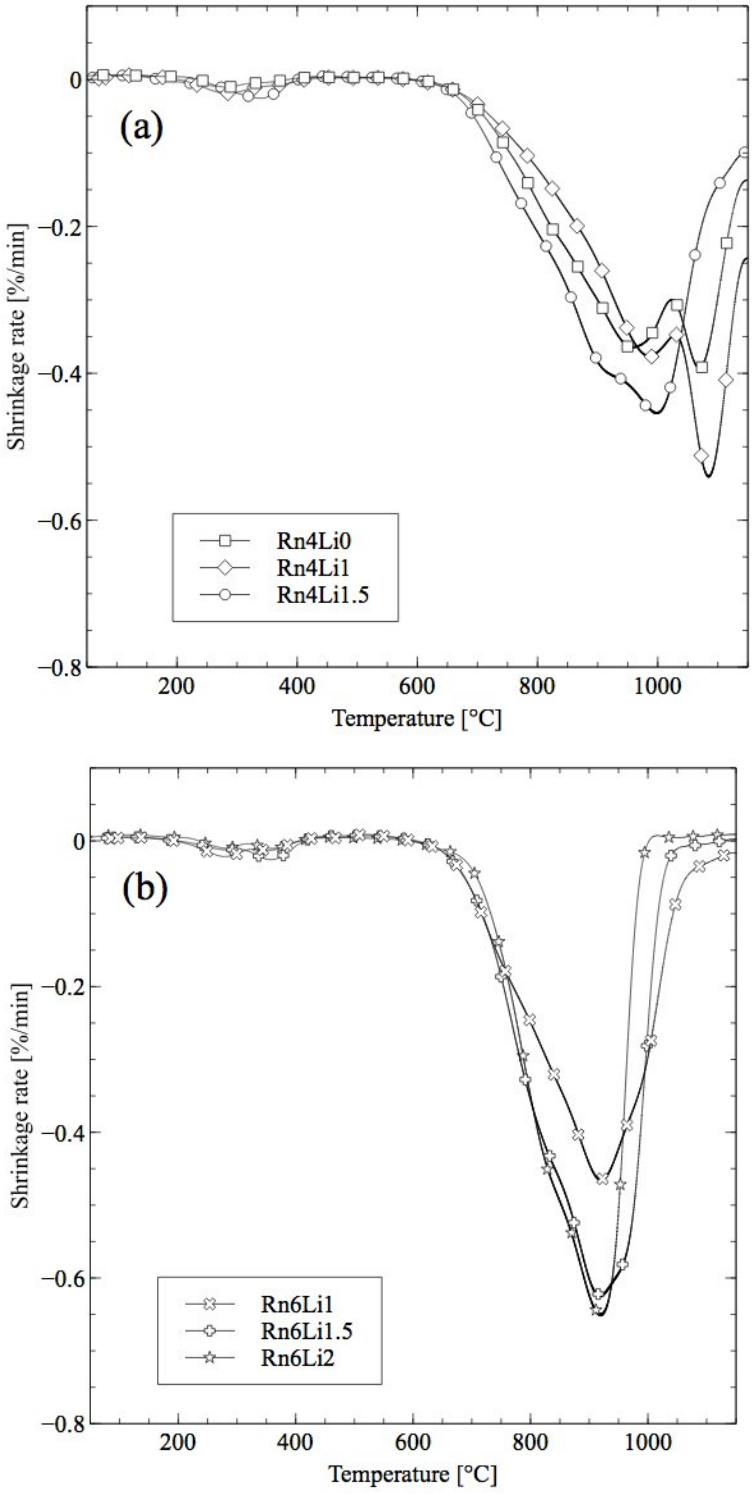

Fig. 5.5a-b Shrinkage rates of anodes with different GDC10 doping of Li_2O for 45vol% (a) and 35vol% (b) of Cu_2O.

The deposition of the electrolytic layer was performed by dip-coating the green anodes in an α-terpineol based slurry. The stabilized weight of the coating deposited after overnight drying at 100°C is reported in Fig. 5.6 in function of the withdrawal speed. Different regimes of film formation were identified for different extraction speeds, as has been previously observed[28,29] for similar suspensions. At low speeds, the so-called "draining regime" is well described by the Landau-Levich model for which the thickness of the coating is defined by the equilibrium between the adhesion of the Newtonian non-evaporating fluid on the substrate and the viscous drag induced by gravity. In this regime, the coating thickness and the speed of withdrawal are proportional. The same relationship was supposed to hold using the weight of coating instead of its thickness.
Although the model is limited to Newtonian fluids and the slurry used was not, as it can be observed from the apparent viscosity plot in Fig. 5.7, this regime was observed for withdrawal speeds of 1 mm/s or faster. For speeds slower than 0.5 mm/s, the capillary rise of the slurry is non negligible and it opposes to draining. In this "capillary regime", a decrease in the withdrawal speed produced a thicker and heavier coating. For speeds belonging to an intermediate range, between 0.5 and 1 mm/s, the capillary rise and the viscous drag were balanced and the thinnest and lightest layers were deposited. Considering that, in general, a thinner electrolyte results in a lower ohmic resistance and increased cell performance, the dip coating was performed at 1 mm/s giving a dried weight of coating of 1.11 mg/mm and a thickness of ~10 μm after sintering.

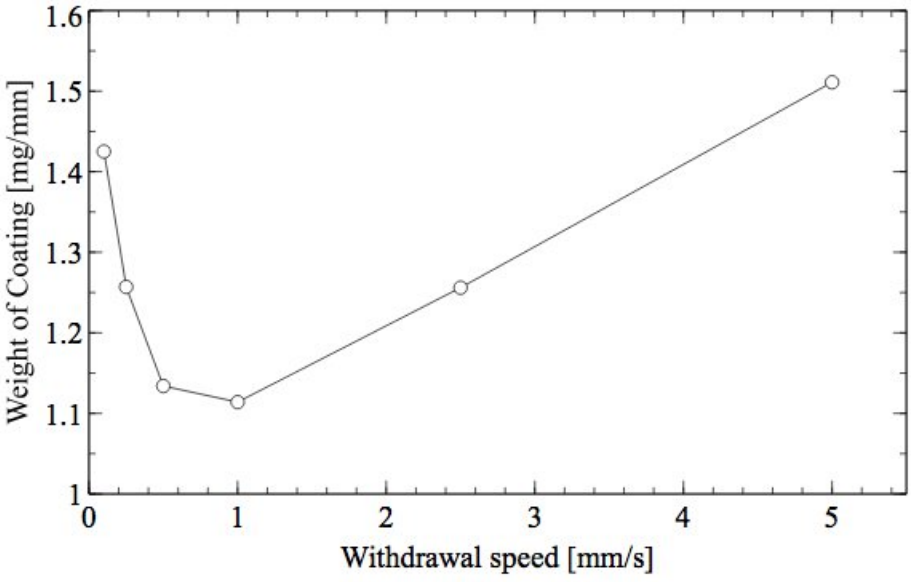

Fig. 5.6 Weight of electrolytic coating after drying 100°C as function of dip coating withdrawal speed.

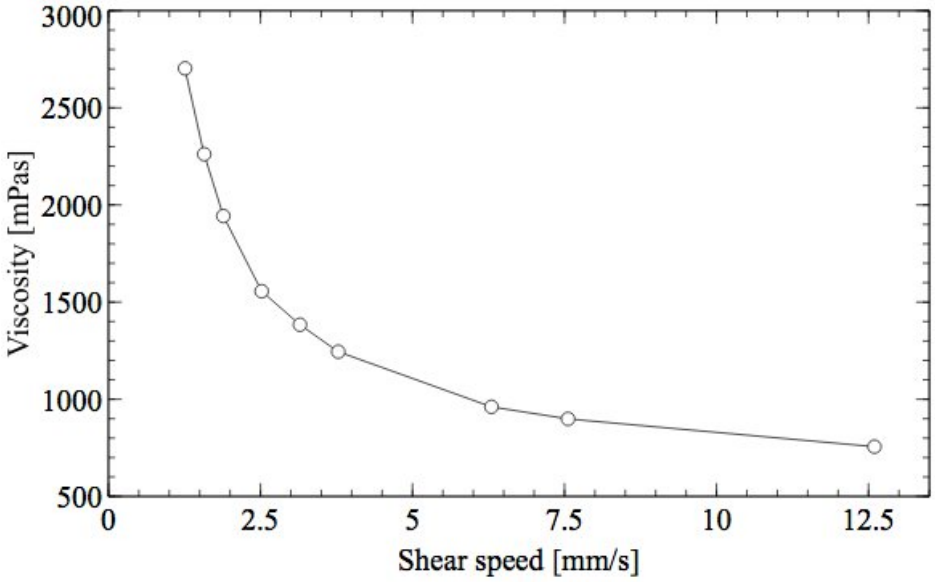

Fig. 5.7 Apparent viscosity of the electrolytic slurry with 40wt% solid loading as function of shear speed.

During co-firing of anode-supported cells, stresses may develop in the structure because of a different sintering behavior of the heterogeneous layers. In this case distortion, delamination, debonding, lack of densification, and damage of the fired structure are likely to occur. It has been shown that a sintering ceramic compact can be treated as a linear viscous material during densification[30]. Applying this model to a system made by two constrained infinite planes it was demonstrated that the equi-biaxial stresses that arise in the layer 1 far away from its free surfaces is given by[30]:

$$\sigma_1 = -\frac{1}{1+mn} E'_{p1} \Delta\dot{\varepsilon} \qquad (5.1)$$

Where $m = t_1/t_2$ is the thickness ratio between the layer 1 (t_1) and 2 (t_2), $\Delta\dot{\varepsilon} = \dot{\varepsilon_1} - \dot{\varepsilon_2}$ is the strain rate mismatch between the two layers and $E'_p = E_p/(1-\nu_p)$, where E_p is the uniaxial viscosity and ν_p the viscous Poisson's ratio. For the case of layer 2 being much thicker than layer 1, $t_1/t_2 \longrightarrow 0$ and the biaxial stress in layer 1 reduces to:

$$\sigma_1 = -E'_{p1} \Delta\dot{\varepsilon} \qquad (5.2)$$

While the stress in the thicker layer 2 due to the thinner layer can be considered negligible. This approach can be applied with good approximation also to tubular structures composed of a thicker anode coated by a thin electrolyte. In this case the principal stress to which the electrolyte is subjected is a hoop stress that can be expressed as:

$$\sigma_{h_{ele}} = -E'_{p_{ele}}(\dot{\varepsilon}_{ele} - \dot{\varepsilon}_{anode}) \qquad (5.3)$$

Then the hoop stress developed in the electrolyte during firing depends on the strain rate difference between the electrolyte and the supporting anode. In the case that the electrolyte is the faster shrinking layer, the difference is positive and a tensile stress will develop in the electrolyte. This will tend to obstruct its densification by lowering the internal sintering pressure and result in a density lower than in the free sintered material. Instead, for a negative value of the strain rate difference, when the anode is the faster shrinking layer, the electrolyte will be in a compressive stress state that will add to the sintering potential, increasing the driving force for sintering and positively influence the densification mechanism causing higher densities than expected[31].

Fig. 5.8 shows the shrinkage rate differences between the stand-alone GDC10 2 mol% Li_2O electrolyte and several different anodes. Although the actual shrinkage rate during firing of each layer depended from its transient relative density, and so it was clearly influenced by the presence of a bonded layer[32] or residual stresses, the difference between the unconstrained shrinkage rates could give a qualitative indication on the magnitude and sign of the stresses developed in the electrolyte.

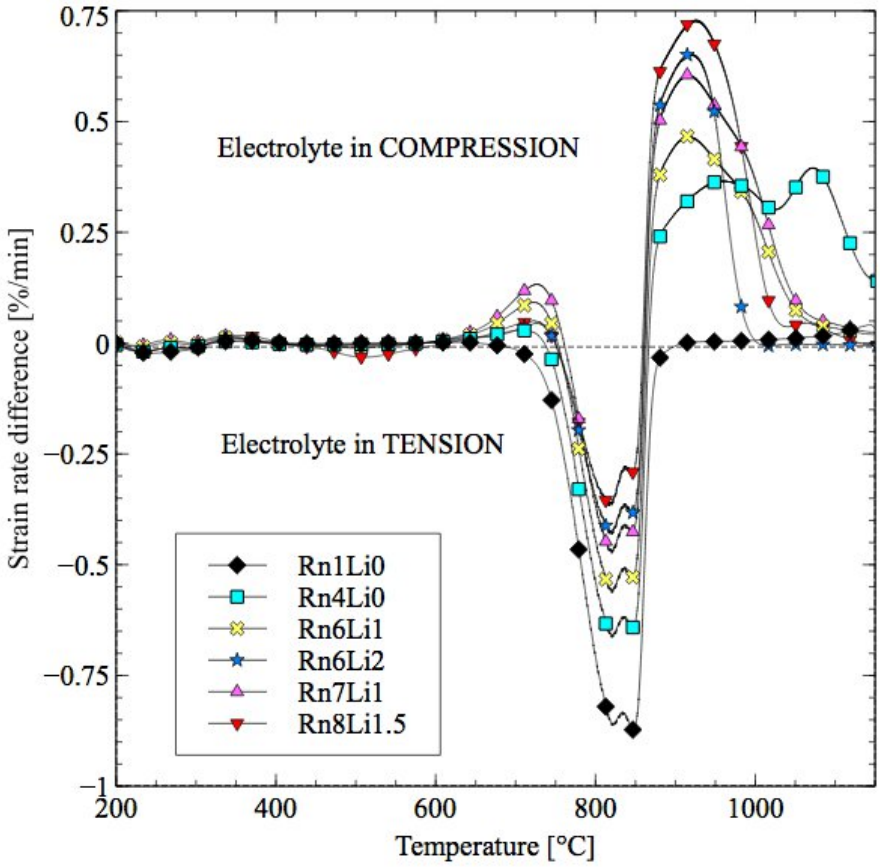

Fig. 5.8 Strain rate difference between the stand-alone GDC10 2 mol%Li_2O doped electrolyte and anodes with different doping and composition with heating rate of 10 °C/min.

In the worst scenario analyzed in Fig. 5.8, the electrolyte was constrained to the Rn1Li0 anode that experienced a very small shrinkage during sintering and could be considered as a rigid substrate. This created a tensile stress state in the electrolyte that hindered its densification. In this case, the only possible densification was in the thickness direction and very limited[31], as it can be appreciated form the SEM micrograph in Fig. 8a. By reducing the Cu_2O content and increasing doping of GDC10 in the anodic composition, the rate difference progressively decreased in the tensile region. Moreover, considering that the substrates keep shrinking also after the stand-alone electrolyte reached its maximum density, the stress sign changed above 860°C, passing from tensile to compressive and aiding the densification of the electrolytic layer.
Comparison of the effect of the anode sintering on the electrolyte densification can be seen in Fig. 5.9, where all the cells were sintered at 1020°C for 3h. Fig. 5.9a-b shows the incomplete densification of the electrolyte when sintered on the undoped Rn1Li0 and Rn4Li0 anodes. The porosity of the electrolyte visibly decreases when Rn6Li1 (Fig. 5.9c) is employed. By co-sintering the electrolyte on the Rn8Li1.5 anode (Fig. 5.9d), full densification of the electrolyte was obtained.

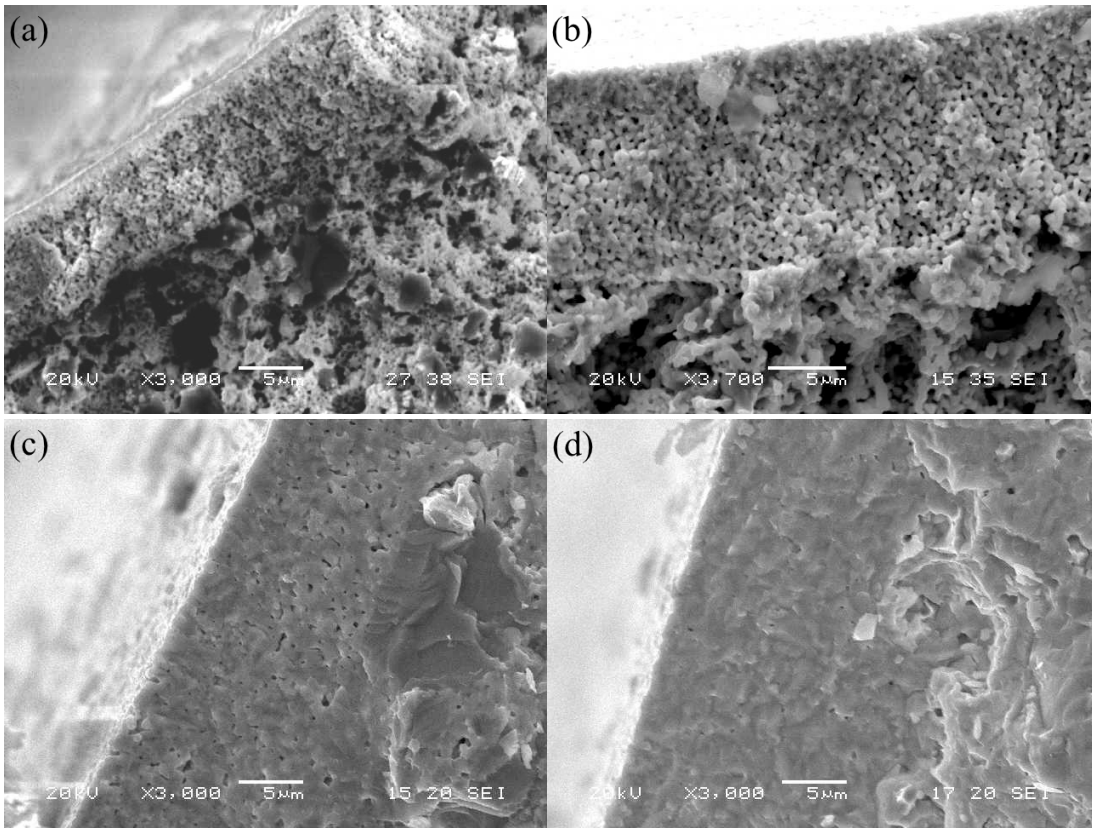

Fig. 5.9 SEM micrographs of half-cell sections sintered at 1020°C for 3h with Rn1Li0 (a), Rn4Li0 (b), Rn6Li1 (c) and Rn8Li1.5 (d) anodes.

In addition to the stresses that can result from sintering, other residual stresses can also develop during the cooling stage of the firing process due to differences of Coefficients of Thermal Expansion (CTEs) in the layer. Once the layered structure reached the end of the high temperature sintering process, it is cooled down from the maximum temperature T^{max} to room temperature T^{r}. The two materials would contract depending on their CTEs. If they are bonded together, they suffer from a mismatch strain in layered materials given by[33]:

$$\varepsilon_M = \int_{T^r}^{T^{max}} (\alpha_{anode} - \alpha_{ele})\, dT \qquad (5.4)$$

Where α_i is the CTE of the anode or electrolyte. This difference in strain causes the onset of a residual stress that, if larger than the mechanical resistance of the electrolyte would cause its rupture. Although during the initial phase of cooling the material can still creep and alleviate the stress state, for most of the cooling temperature range the layers can be considered as purely elastic[30]. Defects occurring during cooling are discernible from those created during firing because they act on an already brittle structure while cracks resulting from sintering mismatch have wider opening and rounded crack edges[34]. Fig. 5.10 shows a SEM micrograph of the electrolytic surface of a half-cell where both type of defects are visible. It can be appreciated how the sintering defects constitute a stress concentration zone for the cooling stress and a defect for the start of crack propagation from where the fracture originate.

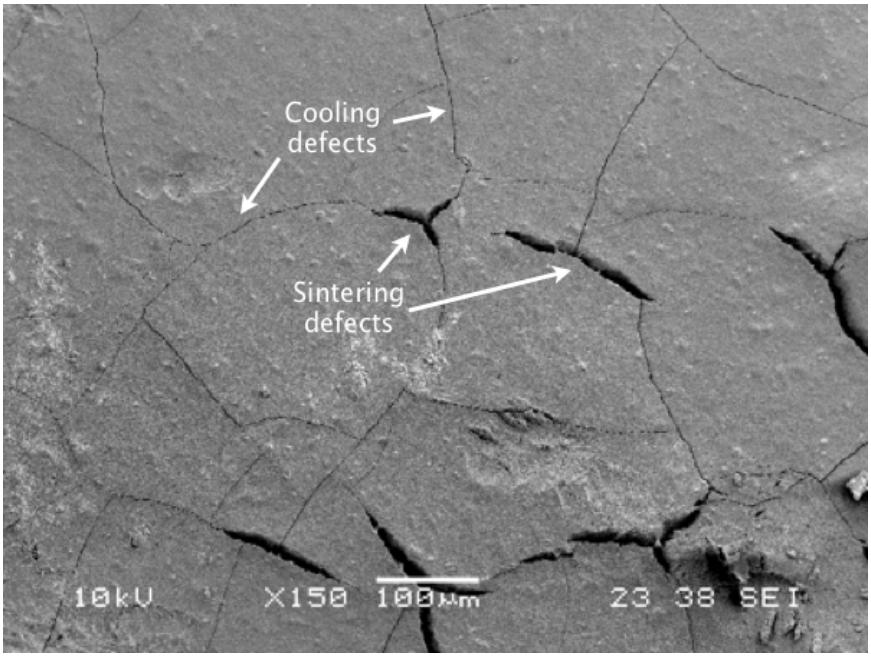

Fig. 5.10 SEM micrograph of a half-cell external surface showing sintering and cooling defects.

To avoid this eventuality, which would allow the direct mixing of fuel with air, the anode and electrolyte CTE mismatch has to be reduced. One of the principal issues encountered during fabrication of copper-based anode-supported SOFCs was related to the low CTE of Cu_2O (~$4.3 \cdot 10^{-6}$/°C) compared to GDC10 (~$13.4 \cdot 10^{-6}$/°C). This means that even a relatively small Cu_2O content would cause a severe reduction of the anode CTE compared to the electrolyte, imposing a tensile stress state during cooling which could likely cause cracking in the thin layer. Another method to reduce ε_M is to reduce T^{max}, which is the maximum temperature reached during firing. It was previously showed that decreasing the Cu_2O content and increasing the doping of the GDC10 permit good densification and complete the sintering process at lower temperature. Although low Cu2O content was then beneficial for the integrity of the electrolytic layer during every phase of the sintering process, on the other side it decreased the electronic conductivity of the anode. Fig. 5.11 shows SEM micrographs of electrolytes co-sintered on different anodes and the development of brittle cracks on their surfaces. It can be noticed that decreasing both the Cu_2O and the sintering temperature produced a better electrolytic integrity. The only anode that resulted in a complete elimination of visible fracture was the Rn8Li1.5 sintered at 1020°C for 3 h and containing 25 vol% of Cu_2O in its initial formulation.

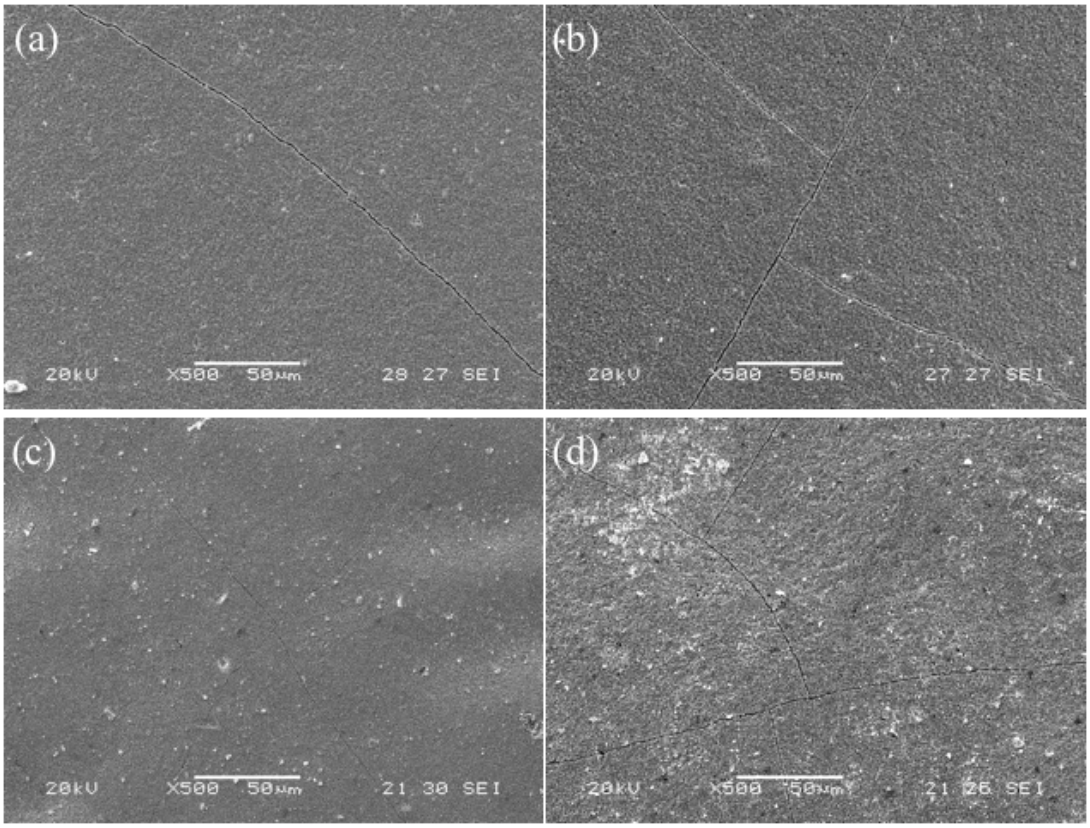

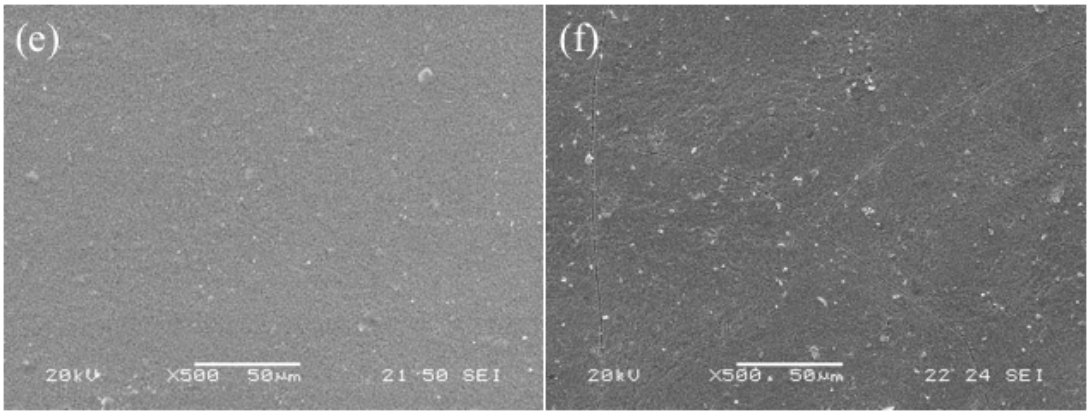

Fig. 5.11 SEM micrographs of half-cells external surface with Rn4Li2 anode sintered at 1020°C (a) and 1070°C (b), with Rn6Li2 at 1020°C (c) and 1070°C (d) and with Rn8Li1.5 at 1020°C (e) and 1070°C (d). Maximum sintering temperature was held constant for 3h.

However, after reduction, this Cu_2O content was found to be insufficient for copper interconnectivity and percolation of the electronically conductive phase. The minimum content required for anode percolation after sintering at 1020°C was found in Rn6Li2 with 35 vol% of Cu_2O. However, the presence of fractures on its surface imposed to further decrease the sintering temperature to 995°C. Based on these results, the anode-electrolyte combination recommended for co-sintering is the Rn6Li2 anode with 2 mol% Li_2O electrolyte sintered at 995°C for 3h. This combination allows for the co-sintering of GDC-based cells below the melting temperature of Cu_2O, ensures a sufficiently dense electrolyte, minimized surface fractures due to stresses resulting from differential cooling, and ensures the interconnectivity of the copper phase after cell reduction. Fig. 5.12 shows a picture of the fabrication stages of the fuel cell, from the green anode to the complete co-sintered fuel cell.

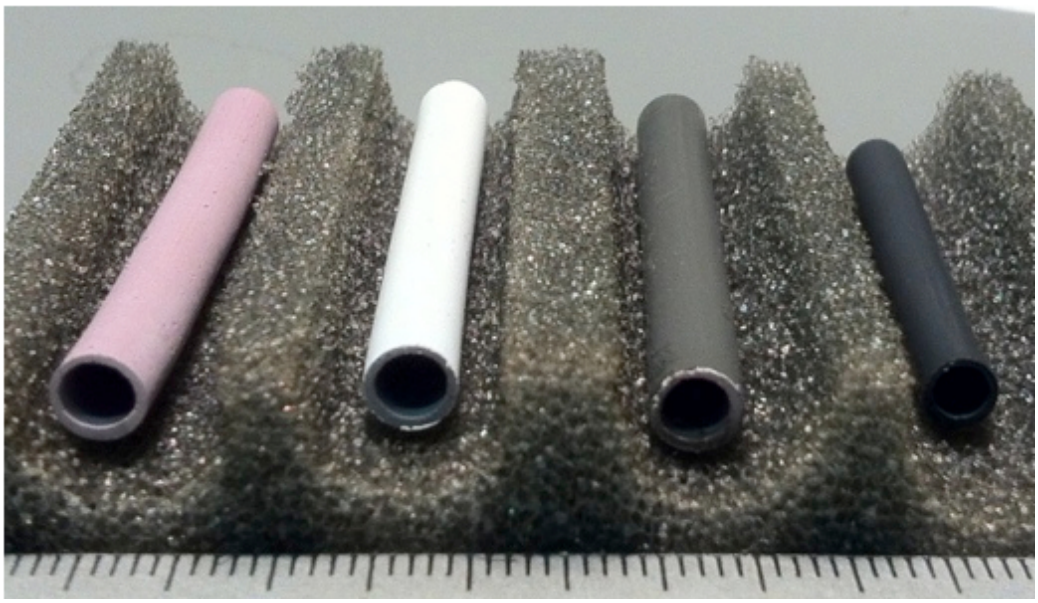

Fig.5.12 Picture of the fuel cell after every fabrication step. From left to right: dried anode, coated with electrolyte, coated with the cathode and sintered.

The SEM micrograph of the fuel cell cross section with the above mentioned recommended condition is shown in Fig. 5.13. Although the electrolyte densification was not particularly advanced, there is not any evidence of interconnected porosity as of interruption of layers integrity and through thickness fractures. However, presence of small fractures not visible by optical microscope observation cannot be totally excluded. The adhesion of the layers, thanks to the one-step co-sintering process, is optimal and any signs of delamination or debonding are observed. The cathode has adequate porosity and regular thickness of ~30μm.

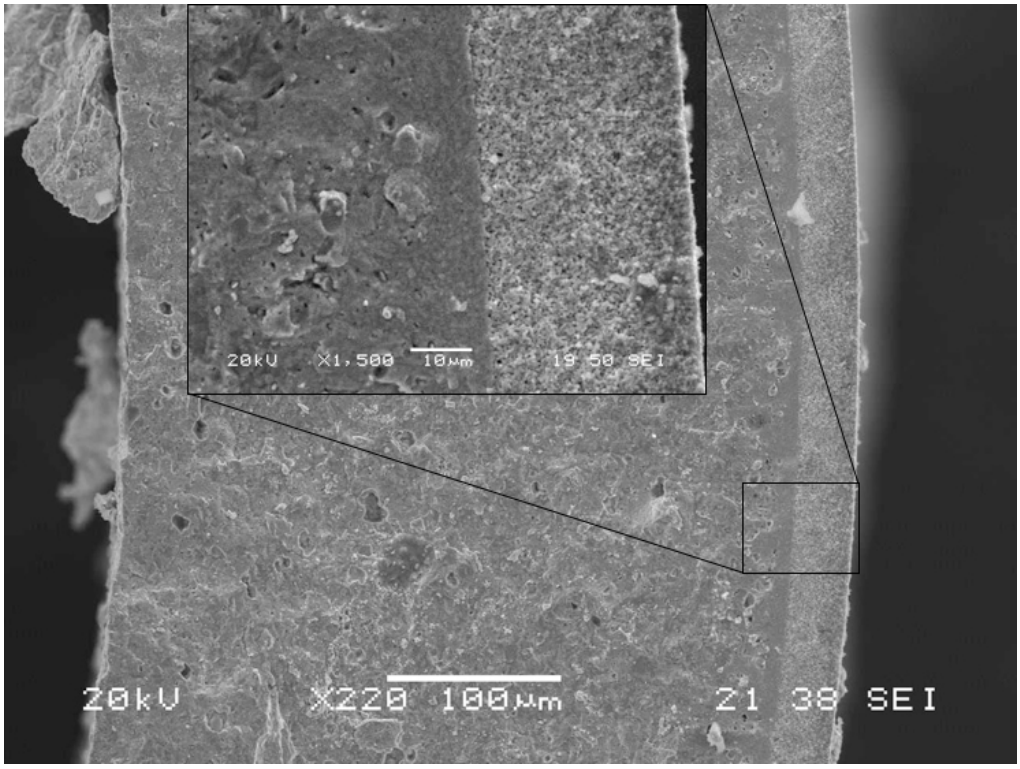

Fig. 5.13 SEM micrograph of a complete cell with Rn6Li2 anode, GDC10-Li_2O 2mol% doped electrolyte and LSF20-GDC10 cathode sintered at 995°C for 3h.

5.4 Conclusions

In this chapter, the feasibility of fabrication of anode-supported Cu_2O based SOFCs by one-step co-sintering when using lithium oxide as sintering aid is showed. Both the reduction of the Cu_2O content and the increase of lithium oxide doping were beneficial to decrease the sintering temperature and increase the sintering rate. For Cu_2O content lower or equal than 35 vol% and doping equal or higher than 1 mol%, sintering of the cermet occurs in one regular step

and it is completed below 1100°C. A thin GDC lithium oxide doped electrolyte was deposited by dip coating at 1 mm/s giving a dried weight of coating of 1.11 mg/mm and a thickness of ~10 µm after sintering. To completely avoid cracks formation due to large CTEs mismatches between anode and electrolyte, the Cu_2O content had to be reduced to 25vol%, but this was insufficient to achieve electronic conductivity after reduction. A complete SOFC with LSF20-GDC cathode and anode containing 35vol% Cu_2O was sintered at 995°C for 3h, ensuring a sufficiently dense electrolyte, minimizing surface fractures due to stresses resulting from differential cooling, and guaranteeing the interconnectivity of the copper phase after cell reduction.

References

1. Finnerty, C., Coe, N., Cunningham, R. & Ormerod, R. Carbon formation on and deactivation of nickel-based/zirconia anodes in solid oxide fuel cells running on methane. *Catal Today* **46**, 137–145 (1998).
2. Gross, M. D., Vohs, J. M. & Gorte, R. J. Recent progress in SOFC anodes for direct utilization of hydrocarbons. *Journal of Materials Chemistry* **17**, 3071–3077 (2007).
3. Toebes, M. L., Bitter, J. H., Van Dillen, A. J. & de Jong, K. P. Impact of the structure and reactivity of nickel particles on the catalytic growth of carbon nanofibers. *Catalysis today* **76**, 33–42 (2002).
4. LIN, Y., ZHAN, Z. & LIU, J. Direct operation of solid oxide fuel cells with methane fuel. *Solid State Ionics* (2005).
5. Borowiecki, T., Grzegorczyk, W., Denis, A. & Golebiowski, A. Resistance to coking determination by temperature programmed reaction of n-butane with steam. *Catal Lett* **79**, 119–124 (2002).
6. Ruckenstein, E. & Hu, X. The effect of steam on supported metal catalysts. *J Catal* (1986).
7. KIM, H., Park, S., Vohs, J. & Gorte, R. Direct oxidation of liquid fuels in a solid oxide fuel cell. *J Electrochem Soc* **148**, A693–A695 (2001).
8. Gorte, R. & Vohs, J. Novel SOFC anodes for the direct electrochemical oxidation of hydrocarbons. *J Catal* **216**, 477–486 (2003).
9. Craciun, R. *et al.* A novel method for preparing anode cermets for solid oxide fuel cells. *J Electrochem Soc* **146**, 4019–4022 (1999).
10. Jung, S. *et al.* Influence of composition and Cu impregnation method on the performance of Cu/CeO2/YSZ SOFC anodes. *Journal of Power Sources* **154**, 42–50 (2006).
11. Jiang, S. A review of wet impregnation - An alternative method for the fabrication of high performance and nano-structured electrodes of solid oxide fuel cells. *Mat Sci Eng a-Struct* **418**, 199–210 (2006).
12. Lee, S., Ahn, K., Vohs, J. & Gorte, R. Cu-Co bimetallic anodes for direct utilization of methane in SOFCs. *Electrochem Solid St* **8**, A48–A51 (2005).

13. KIM, H., LU, C., Worrell, W., Vohs, J. & Gorte, R. Cu-Ni cermet anodes for direct oxidation of methane in solid-oxide fuel cells. *J Electrochem Soc* **149**, A247–A250 (2002).
14. Gorte, R., Park, S. & Vohs, J. Anodes for Direct Oxidation of Dry Hydrocarbons in a Solid-Oxide Fuel Cell. *Adv. Mater.* (2000).
15. BENYOUCEF, A., KLEIN, D., CODDET, C. & BENYOUCEF, B. Development and characterisation of (Ni, Cu, Co)-YSZ and Cu-Co-YSZ cermets anode materials for SOFC application. *Surface and Coatings Technology* **202**, 2202–2207 (2008).
16. Park, E. W., Moon, H., Park, M.-S. & Hyun, S. H. Fabrication and characterization of Cu–Ni–YSZ SOFC anodes for direct use of methane via Cu-electroplating. *Int J Hydrogen Energ* **34**, 5537–5545 (2009).
17. Gross, M. D., Vohs, J. M. & Gorte, R. J. A study of thermal stability and methane tolerance of Cu-based SOFC anodes with electrodeposited Co. *Electrochimica Acta* **52**, 1951–1957 (2007).
18. Gerhardt-Anderson, R. Ionic conductivity of CeO2 with trivalent dopants of different ionic radii. *Solid State Ionics* (1981).
19. Kuharuangrong, S. Ionic conductivity of Sm, Gd, Dy and Er-doped ceria. *Journal of Power Sources* (2007).
20. Muthukkumaran, K., Kuppusami, P., Mohandas, E., Raghunathan, V. & Selladurai, S. Ionic conductivity measurements in gadolinia doped ceria. *International Symposium of Research Students on Material Science and Engineering, Chennai (ISRS)* 1–8 (2004).
21. Mori, M., Yamamoto, T., Itoh, H., Inaba, H. & Tagawa, H. Thermal Expansion of Nickel-Zirconia Anodes in Solid Oxide Fuel Cells during Fabrication and Operation. *J Electrochem Soc* **145**, 1374–1381 (1998).
22. P A Korzhavyi, B. J. Literature review on the properties of cuprous oxide Cu2O and the process of copper oxidation. 1–41 (2012).
23. Atkinson, A. & Selcuk, A. Residual stress and fracture of laminated ceramic membranes. *Acta Materialia* **47**, 867–874 (1999).
24. Azzolini, A., Sglavo, V. & Downs, J. Novel method for the identification of the maximum solid loading suitable for optimal extrusion of ceramic pastes. *J Adv Ceram* (2014).
25. Neumann, J., Zhong, T. & Chang, Y. The Cu– O (Copper-Oxygen) system. *Journal of Phase Equilibria* **5**, 136–140 (1984).
26. Feng, L., Yu, X. & Zhang, Y. Preparation of Cu2O-Cu Cermets by In situ Reduction Method. *Int J Appl Ceram Tec* (2014).
27. Higgins, R. The chemistry of carbon retention during non-oxidative binder removal from ceramic greenware. *Thesis (Sc. D.)--Massachusetts Institute of Technology, Dept. of Materials Science and Engineering, 1990.* (1990).
28. Faustini, M., Louis, B., Albouy, P. A., Kuemmel, M. & Grosso, D. Preparation of Sol–Gel Films by Dip-Coating in Extreme Conditions. *J. Phys. Chem. C* **114**, 7637–7645 (2010).
29. Grosso, D. How to exploit the full potential of the dip-coating process to better control film formation. *Journal of Materials Chemistry* (2011).
30. Cai, P. Z., Green, D. J. & Messing, G. L. Constrained densification of alumina/zirconia hybrid laminates, II: viscoelastic stress computation. *J Am Ceram Soc* **80**, 1940–1948 (1997).
31. Green, D. J., Guillon, O. & Rödel, J. Constrained sintering: A delicate balance

of scales. *Journal of the European Ceramic Society* **28**, 1451–1466 (2008).
32. Cai, P. Z., Green, D. J. & Messing, G. L. Constrained densification of alumina/zirconia hybrid laminates, I: experimental observations of processing defects. *J Am Ceram Soc* **80**, 1929–1939 (1997).
33. Ho, S., Hillman, C., Lange, F. & Suo, Z. Surface cracking in layers under biaxial, residual compressive stress. *J Am Ceram Soc* **78**, 2353–2359 (1995).
34. Li, W., Feingold, A., Palanisamy, P. & Lorenz, G. Co-sintering Zirconia Electrolyte and Insulator Tapes for Sensor Applications. *J Am Ceram Soc* **95**, 3815–3820 (2012).

6. Production and performance of copper-based anode-supported SOFC*

Abstract

The cell configuration and fabrication technique developed for the Cu_2O based anodes and discussed in the previous chapter were applied to the composition with CuO. The formulations that achieved better microstructure and minimized crack formations for both oxides were compared during co-sintering and reduction. The issues related to the employment of cuprite during the reduction step were identified. Finally, the electrochemical tests of the tenorite based SOFC are reported.

Keywords: CuO-based cermet, Reduction, Electrochemical test.

6.1 Introduction

In the previous chapter, the main issues relative to the employment of Cu_2O in the anodic cermet and the co-sintering in non-oxidative atmosphere were identified. Here, the same cell configuration and fabrication process is applied to the formulation with the other oxide form of copper, tenorite (CuO). Although CuO has a lower melting point than Cu_2O, which imposes an even lower co-sintering temperature, its employment carries also some benefits. Being the most oxidized form of copper, in fact, means that the co-sintering process can be performed in air, decreasing the waste of protective argon and permitting the complete burn-out of the organics additives used for fabrication without the issues related to carboreduction. Also, CuO is characterized by a higher CTE than Cu_2O ($CET_{CuO}=9.3\cdot10^{-6}/°C$)[1], decreasing the strain mismatch between anode and electrolyte during cooling and the probability of brittle cracks on the cell surface. In this chapter the extruded anodes were prepared mixing GDC10 with both copper oxides in order to determine the most convenient to use. The GDC10 employed in the cermet and the electrolyte was doped with lithium nitrate to reduce the co-sintering temperature below the melting temperature of the copper oxides. Both electrolyte and cathode were deposited by dip-coating an

* *Part of this chapter has been submitted to* "Journal of Power Sources" *with the title: "Electrochemical performance of Copper-GDC anode supported IT-SOFC produced by one step sintering".*

organic-based slurry. The complete cell was sintered between 970°C and 1020°C and subjected to electrochemical tests; hydrogen was preliminarily used as fuel to determine the functionality of the produced cells and detect the best processing conditions.

6.2 Experimental

The raw powders used in this chapter were the same listed in the previous chapter except from copper (II) oxide (<10 µm, 99%, Sigma Aldrich). A detailed description of the fabrication steps for the supporting tubular anodes is contained in Section 5.2. In the case of Cu_2O, the formulation that was found to be most promising in Chapter 5 was used (35vol% of Cu_2O). Considering the slightly larger decrease in volume under reduction compared to Cu_2O (~3vol%), the tenorite-based anodes were formulated with 40vol% of CuO. The two different paste compositions are reported in Tab. 6.1, where the theoretical and experimental weight losses after every step of the fabrication of the cermets, from extrusion to reduction, are also reported. The electrolyte and cathode preparation/deposition are also described in Section 5.2.

Tab. 6.1 Composition of the produced anodes. The weight losses expected and recorder after each fabrication steps are also reported.

		Bn5Li2	Rn6Li2
Solid phase [vol%]	GDC10 (2mol%Li_2O)	60	65
	CuO	40	/
	Cu_2O	/	35
Solid Loading [vol%]		51	61
Binder [wt% on liquid phase]		3	2
Weight loss aft. drying [100°C overnight]	Experimental	13.96%(±0.13%)	8.46%(±0.48%)
	Theoretical	14.23%	8.76%
Weight loss aft. firing	Experimental	1.32%(±0.09%)	1.90%(±0.14%)
	Theoretical	1.20%	1.05%
Weight loss aft. reduction [2hrs @ 540°C]	Experimental	7.80%(±0.11%)	2.72%(±0.03%)
	Theoretical	7.62%	3.56%
Total weight loss, from extrusion to reduction.	Experimental	20.15%(±0.98%)	12.6%(±1.2%)
	Theoretical	20.10%	12.93%

To study the oxidation-reduction and melting behavior of the CuO and Cu_2O used for the anode preparations, thermogravimetry and differential thermal analysis (TG/DTA, Netzsch thermobalance STA 409) were performed with a heating rate of 10°C/min using alumina crucibles and alumina powder as reference. Analyses were performed in static air and in argon flux.

The sintering behavior of green anodes, half-cells and complete cells were measured by dilatometry (Linseis L75 Platinum Series, Linseis Instrument) using an alumina support tube and a constant heating rate of 10°C/min up to 1150°C. The behavior of cells formulated with CuO and Cu_2O were compared. In the case of Cu_2O containing anodes, the measurement was performed in argon flux to avoid the Cu_2O oxidation. Before every measurement the instrument chamber was evacuated and filled with argon three times to remove the air from the chamber or the sample pores. For the CuO containing anodes, the measurement was performed in static air, because no oxidation of CuO was expected. Dilatometric measurements were also performed on the complete sintered cells formulated with both oxides in forming gas (3% H_2 in Ar) flux to study their behavior during reduction.

Half-cells and complete cells were sintered in a tubular furnace at constant heating rate of 2°C/min. During heating, an isothermal step at 500°C for 1h allowed the organics burnout. Heating was continued up to the sintering temperature, which was hold for 3h. Cooling was controlled at 5°C/min down to 700°C followed by free cooling. The sample holder was specifically designed and produced for this application: alumina capillaries were used to suspend the tubular samples within the furnace without reducing or deviating the gas flux and maximizing the removal of the volatile species produced by the organics decomposition. For cells formulated with CuO, sintering was performed in air flux while for those with Cu_2O high-purity argon was fluxed to avoid oxidation of cuprite. The anodes reduction was completed at 540°C for 2h with heating rate of 5°C/min and free cooling, under 3% H_2 in Ar flux.

Produced tubular SOFC were tested using H_2 as fuel (H_2:N_2=1:1) and air as oxidant. The ceramic sealing was applied and dried at 80°C overnight. The reduction of the cells was carried out fluxing the hydrogen mixture from room temperature and heating up to the testing temperature at 5°C/min. During this phase the sealing cured and insured no leakage. As for current collectors, a gold mesh was used for the cathode and a nickel mesh for the anode. The tests were performed after the OCV reached a stable value for not less than 30 min.

6.3 Results and Discussion

Copper oxidizes in two structures: simple cubic (Cu_2O or cuprite) and monoclinic (CuO or tenorite). TG/DTA analysis (Fig. 6.1) allowed identifying the stability range, phase changes and melting temperature for the two compounds and for two firing atmospheres. Tenorite (Fig. 6.1a) is the stable oxide in standard condition.

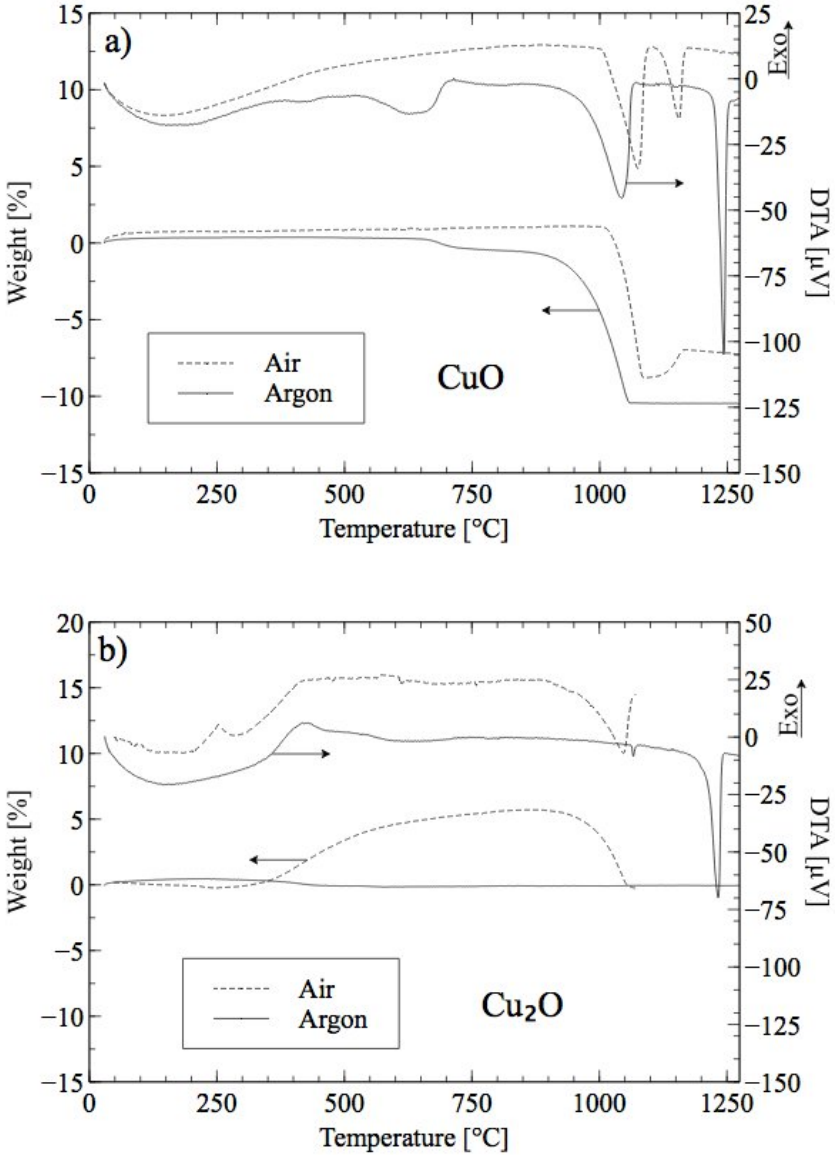

Fig. 6.1 TG/DTA analysis of CuO (a) and Cu_2O (b) in air and argon flux with heating rate of 10°C/min.

Heated in air, it began to reduce to cuprite at ~1026°C, with 10% weight loss, as expected. The successive endothermic peak corresponds to cuprite melting at 1152°C. In case of high purity argon atmosphere and low oxygen partial pressure

(P_{O_2} ~$3.23 \cdot 10^{-4}$ bar), the reduction happened at lower temperature: a first reduction step, probably corresponding to the outer layer of tenorite particles, occurred already around 700°C, followed by a major step that completed the reduction at 1056°C. In this condition, cuprite melted congruently at higher temperature compared to the air treatment, as indicated by the sharp endothermic peak at 1230°C. When the starting phase was cuprite (Fig. 6.1b), heating in air caused its immediate oxidation to tenorite. However, the kinetic of this reaction is considerably slow and the weight gain is observable above 400°C. Oxidation of cuprite interested initially the external surface of the oxide particle, then slowly penetrates within the bulk[2]. The weight gain trend confirms this, showing an initial faster step below 500°C followed by a slower step for bulk oxidation up to 900°C. The recorded total weight gain is ~6%, compared to the expected 10.1%, thus indicating that the process was not completed. Above 900°C, the tenorite produced by the oxidation reduced back to cuprite in one quick step of less than 150°C. In Ar atmosphere, the oxidation could be completely avoided and cuprite did not record any weight change in the whole analyzed range. Except for the small endothermic peak at 1066°C corresponding to the eutectic Cu-Cu_2O melting, that indicates the possible presence of some metallic copper already in the starting powder, cuprite melted congruently at 1230°C.

During sintering it is desirable that the employed oxide is stable in the widest temperature range without experiencing any phase changes, being usually associated with volumetric variations that can compromise the cermet integrity.

Then, two possible approaches were identified: considering that the highest melting temperature recorded for any oxides was 1230°C for cuprite in Ar atmosphere, the approach explored in Chapter 5 consisted in including cuprite in the anode and performing the sintering in high-purity argon atmosphere. Conversely, the use of tenorite would have simplified the sintering process in air since no further oxidation was possible. Then, a second approach consisted in the use of CuO in the anodic composition and sintering in air. In this case the maximum sintering temperature had to be limited below 1026°C because cooling from higher temperature would have caused to oxidize back the cuprite formed, with increase in volume and probable damaging of the cermet.

The anodic cermet formulations are reported in Tab. 6.1 for the two oxides used (Bn5Li2 for the CuO and Rn6Li2 for the Cu_2O). Photographs of the green anodes are shown in Fig. 6.2. The weight loss after every step of the cermet fabrication process (drying, firing and reduction) and the comparison between the expected and recorded values averaged on more than 10 samples, are also reported in Tab. 6.1. While the weight losses for the tenorite containing anodes matched the expected values for every step, the weight losses of the cuprite containing anodes during sintering were always larger that the estimated ones. In addition, although performed at temperatures below 1230°C, sintering of the Rn6Li2 was accompanied by formation of bubbles of molten metal on the anode surface. The

explanation of these effects could be found in the reduction of some cuprite induced by the incomplete oxidation/removal of the organics used in the extrusion paste in non-oxidative sintering atmosphere (see section 5.3).

Fig. 6.2 Green Bn5Li2 (left) and Rn6Li2 (right) anodes.

The shrinkages during sintering and the influence of the electrolytic and cathodic coatings are reported in Fig. 6.3a and 6.3b. For both stand-alone anodes, sintering began at ~700°C and could be considered completed at 1000°C and 920°C for Rn6Li2 and Bn5Li2, respectively. The shrinkages of the cermets followed a regular curve and reached a similar maximum value of 10.5%. Although its thickness was by far lower than that of the anode, the influence of the electrolytic layer is evident for both compositions and resulted in increasing the maximum shrinkage by ~1.5% and ~2% for Rn6Li2 and Bn5Li2, respectively. While the cathodic coating seemed to be ineffective on sintering of Rn6Li2, it caused a further shrinkage of 1% for the Bn5Li2 together with a small shift of the sintering curve toward higher temperatures. Complete cells with both anodic compositions followed a regular sintering curve and reached full densification in a single step below ~1000°C and ~970°C for Rn6Li2 and Bn5Li2, respectively. Then, it was feasible to complete the sintering process below the safe temperature for both compositions.

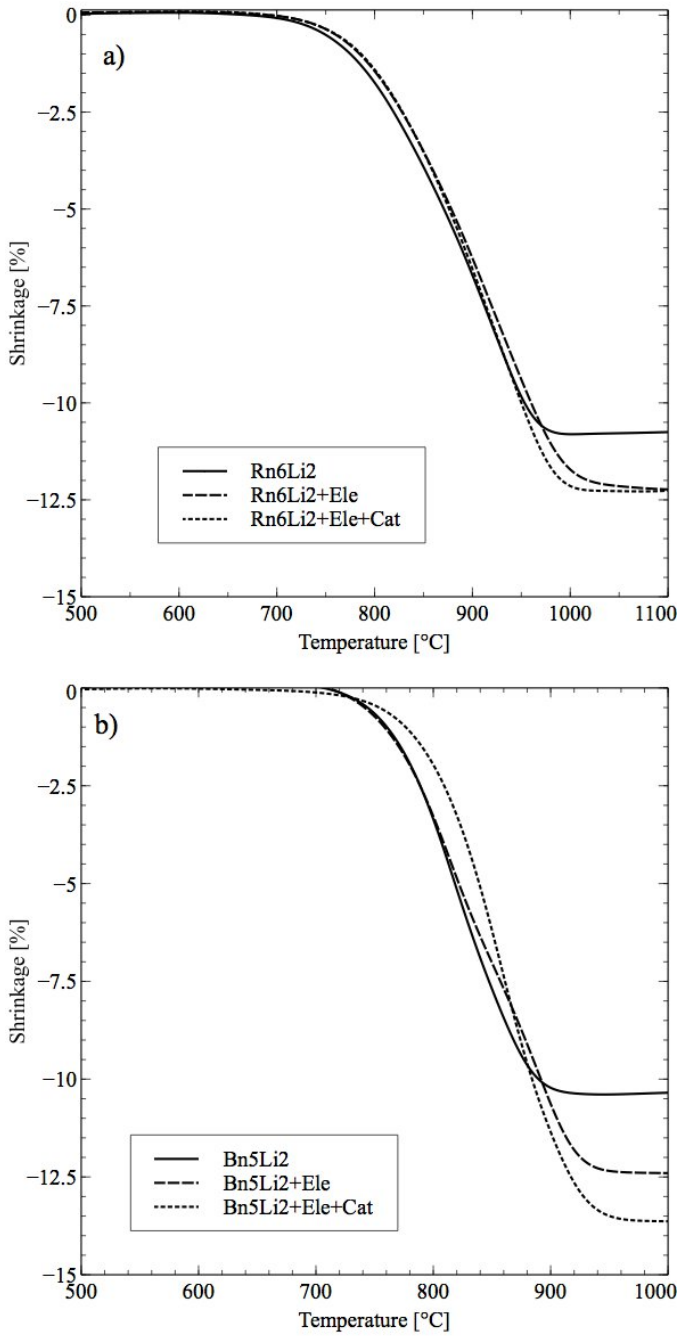

Fig. 6.3 Dilatometric analysis of cuprite (a) and tenorite (b) containing anodes, half-cells and complete cells carried out in argon and air flux, respectively.

SEM micrographs of the sections and surfaces of the complete cells and of the electrolytic surfaces of the half-cells are shown in Fig. 6.4 and 6.5.

Regarding Rn6Li2 (Fig. 6.4), the observation of the electrolyte from the top view (right column) shows that it reached an advanced stage of densification for the three temperatures of treatment. In case of co-sintering with the cathode, some porosity can be spotted from the cross section view of the sample sintered at 995°C and 1020°C (left column). Apparently, the presence of the cathode might be detrimental for the growth of the GDC10 grains of the electrolyte during co-

sintering, although it insures very good bonding and perfect adhesion at the interface.

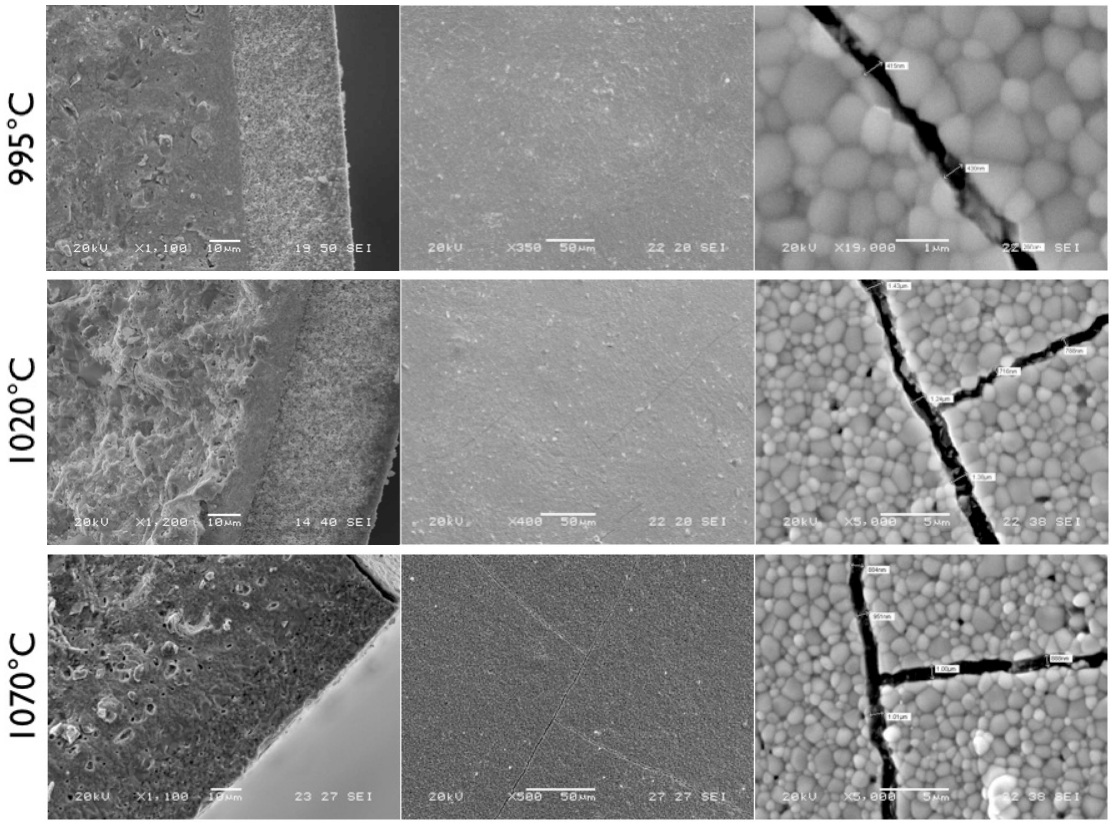

Fig. 6.4 SEM micrographs of half and complete cells with Rn6Li2 anodes sintered at 995°C, 1020°C and 1070°C for 3h; from left to right: cross section of the fracture surface of complete cells, surface of complete cells and surface of the half-cells.

However, the electrolytes of every Rn6Li2 sample suffered by the presence of surface fractures that can be explained considering the large thermal expansion coefficient (CET) mismatch between anode and electrolyte. In fact, both Cu_2O ($4.3 \cdot 10^{-6}$/°C) and CuO ($9.3 \cdot 10^{-6}$/°C)[1] have lower CET compared to GDC10 ($13.4 \cdot 10^{-6}$/°C)[3]. This means that during cooling after sintering, the anode shrank less than the electrolyte, creating the onset of a tensile stress and promoting fractures in the latter. In the case of Rn6Li2, there is almost a magnitude of difference, and this issue was particularly severe. As observed in Chapter 5, decreasing the mismatch by reducing the oxide content in the cermet, caused the opening of fewer fractures and completely eliminated them for the formulation with 25vol% of Cu_2O, but also compromised the electronic conductivity of the anode. The reduction of sintering temperature was also beneficial and caused a decrease in residual stress. Its effect on the surface integrity is evident and shown in Fig. 6.4. The width and the number of the fractures increased with increasing sintering temperature, even by only 25°C (central column). For the

sample sintered at 995°C, the fractures were initially not visible by optical microscope observation, and revealed their presence only at high magnifications of the surface. It has to be said, however, that the cells were broken appositely before observation and this may have caused the worsening of the electrolyte integrity. Then, if on one side decreasing the sintering temperature to 995°C helped to reduce the number and width of the cracks, but without completely eliminate them, on the other did not bring the electrolyte to the full densification. The same trade-off problem held for the cells formulated with tenorite (Fig. 6.5) although the higher CET of CuO was definitely an improvement. Sintering at 1020°C produced a fully densified electrolyte but decreases notably the cathode porosity and some cracks could be spotted on the surface. By decreasing the sintering temperature of 50°C, the cracks disappeared but the densification of the electrolyte was not complete, leaving out some porosity (right column).

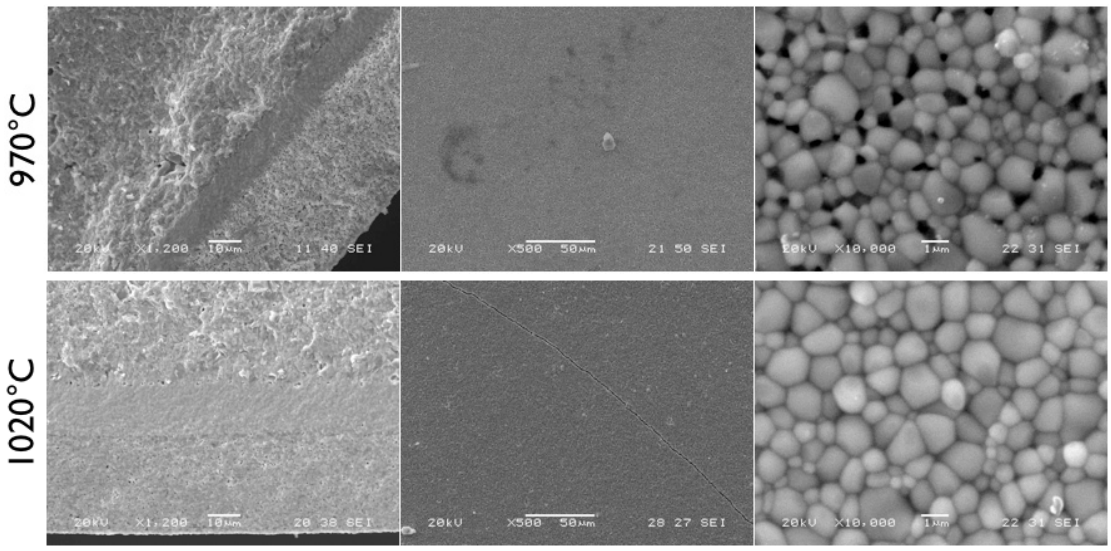

Fig. 6.5 SEM micrographs of half and complete cells with Bn5Li2 anodes sintered at 970°C and 1020°C for 3h; from left to right: cross section of the fracture surface of complete cells, surface of complete cells and surface of the half-cells.

The dilatometric behavior during anodic reduction with forming gas (3% H_2 in Ar) was tested for cells with both formulations and is reported in Fig. 6.6. The cell containing tenorite sintered at 970°C (Fig. 6.6a), shows an increase in the expansion slope at about 200°C. Above this temperature, the expansion is linear and a $CET_{200\text{-}600°C}$ = $12.0 \cdot 10^{-6}$/°C was obtained by fitting with good approximation. This value is lower than the expected $13.9 \cdot 10^{-6}$/°C relative to the reduced stand-alone anode. However, the weight loss after the measurement matched the theoretical expectation in case of complete reduction of the CuO and the anode was proved to be conductive, thus indicating that the measured mismatch was probably caused by the effect of the electrolytic and cathodic

layers on the thermal expansion. The external surface of the reduced cell was scanned by optical microscope to check the presence of fractures, revealing any.

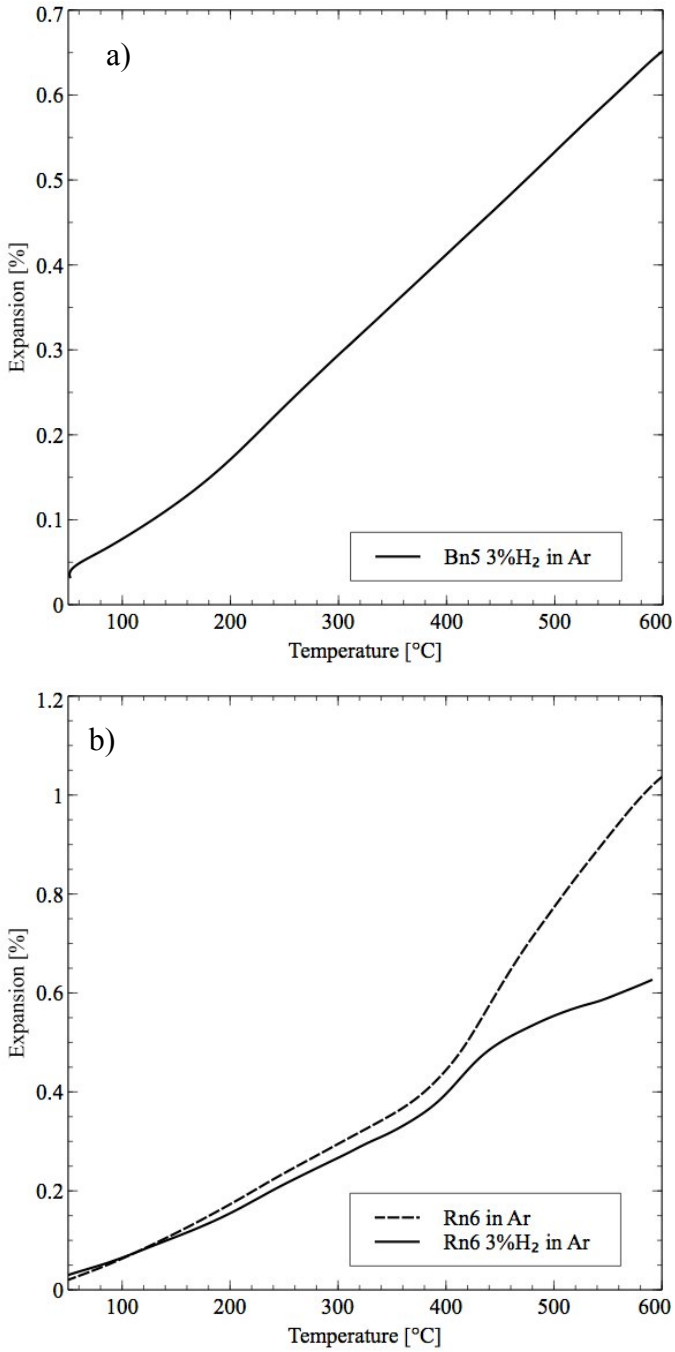

Fig. 6.6 Dilatometric analysis: (a) in forming gas flux at 5°C/min of complete cell with Bn5Li2 anode, sintered at 970°C for 3h; (b) in forming gas flux and argon flux at 5°C/min of complete cell with Rn6Li2 anode, sintered at 995°C for 3h.

For the cell formulated with Cu_2O and sintered at 995°C (Fig. 6.6b), the dilatometric analysis in forming gas shows a clear step at about 400°C. Under high-purity argon flux the step occurred in the same temperature range but the expansion continued with steeper slope. A possible explanation for this behavior

could be the oxidation of a part of cuprite to tenorite, that in air occurs around 400°C, as shown by TG/DTA plots in Fig. 6.1b or, more likely, in the oxidation of some Cu caused by the carboreduction during sintering. Nevertheless, it is not clear yet where the required oxygen came from, considering that particular care was used to create and maintain a non-oxidative environment. After the dilatometric tests, the observation of the cell surface showed that both treatments, in forming gas and in argon, resulted in the formation of additional cracks. In conclusion, the cell containing cuprite was believed to necessitate special care also during the reduction step because the oxidation, even partial, of the anode appeared to be difficult to avoid also in mildly reducing atmospheres.

Complete cells of both compositions were tested using H_2 as fuel (H_2:N_2=1:1) and air as oxidant using the set-up showed in Fig. 6.7.

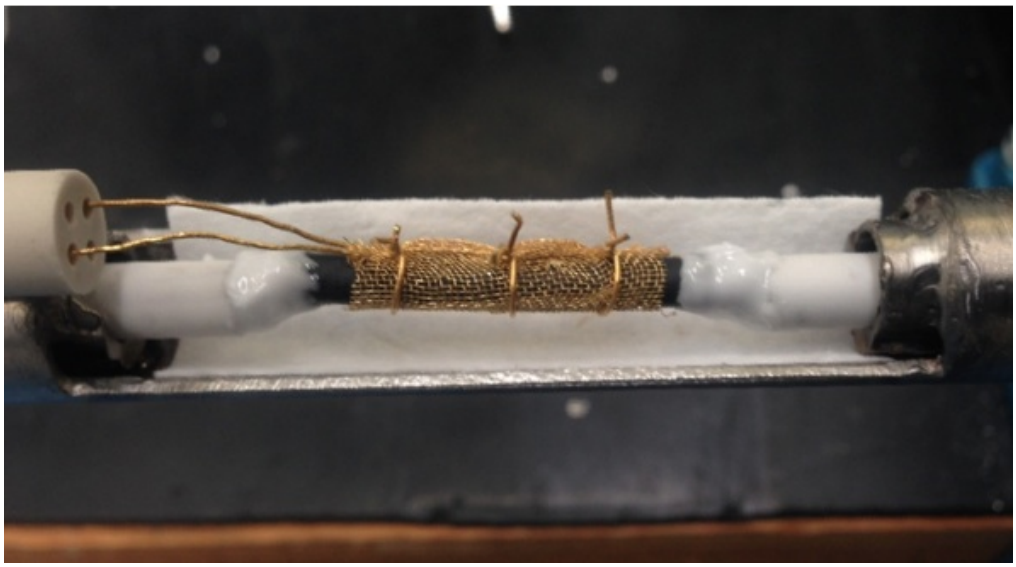

Fig. 6.7 Detail of the set-up used for testing the cells.

For Rn6Li2 cells the electrochemical tests were always unsuccessful. The open circuit voltage (OCV) dropped to zero when the cell reached 400°C, this pointing out that the integrity of the electrolyte was lost. The same results were obtained flowing either reducing or inert gas from room temperature. Post mortem analysis showed that the cell broke in several pieces and the anode was dark in color, this indicating the occurrence of oxidation. A possible explanation could be related to the oxidation of the anode, similarly to what happened during the dilatometric analysis. However, it was not clear if the oxidation caused the failure or if it is the consequence of leakage of air through the cracks already present on the surface of the sintered cell.
The performance of cells with Bn5Li2 anode is shown in Fig. 6.8. During testing, the maximum current density was limited to 20 $mA \cdot cm^{-2}$ to protect the cell.

Because of this, the peak power density was not necessarily measured. Results are reported as the peak power density if it was reached or the maximum measured power density if the current density limit was reached first. Extrapolation of the current-voltage behavior was used to estimate the theoretical maximum power density. The cell sintered at 970°C showed a low OCV and at 450°C had an OCV of 0.29 V. Increasing the temperature to 500°C left the OCV relatively unchanged at 0.28 V. The polarization plots are shown in Fig. 6.8a. The peak power density measured at 450°C was 1.68 $mW \cdot cm^{-2}$. At 500°C, the maximum measured power density was 3.46 $mW \cdot cm^{-2}$. The power curve was starting to flatten, and the maximum power density was estimated to be 3.75 $mW \cdot cm^{-2}$. Testing at 550°C resulted in the loss of OCV and failure of the cells. Failure was verified by post mortem analysis: the cell broke in several fragments when removed from the set-up and the oxidation was considerable.

The cell sintered at 1020°C, showed a OCV twice as high as the cell sintered at 970°C and was thus tested at higher temperatures. The OCVs were 0.50 V, 0.54 V and 0.54 at 500°C, 550°C, and 600°C respectively. Again, the current density was limited to protect the cell. At 500°C, the maximum measured power density was 5.41 $mW \cdot cm^{-2}$, very near the peak power density. When measured at 550°C and 600°C, the power density was still increasing with current density. The highest values measured were 7.64 $mW \cdot cm^{-2}$ and 8.98 $mW \cdot cm^{-2}$ respectively with the estimated peak power densities being 10.1 $mW \cdot cm^{-2}$ and 27.5 $mW \cdot cm^{-2}$. Increasing the temperature beyond 600°C resulted in instability of the OCV indicating the deterioration of the cell so measurements were stopped. Even in this case, the lower OCV compared to the Nerst voltage could be caused by leakage. It is plausible, although some cracks were initially presents, that the leakage was lower in this case because of a more advanced stage of sintering reached by the electrolyte and, more probably, of denser anode and cathode. The post mortem analysis revealed some new surface flaws but the cell was still intact and resistant to handling even after removing from the test set-up. The anode was conductive even after testing, pointing out limited oxidation.

With optimization of the CuO content to minimize cracking, sintering temperature to ensure a sufficient electrolyte density, and use of pore former to improve electrode porosities, the performance of these cells can most certainly be improved.

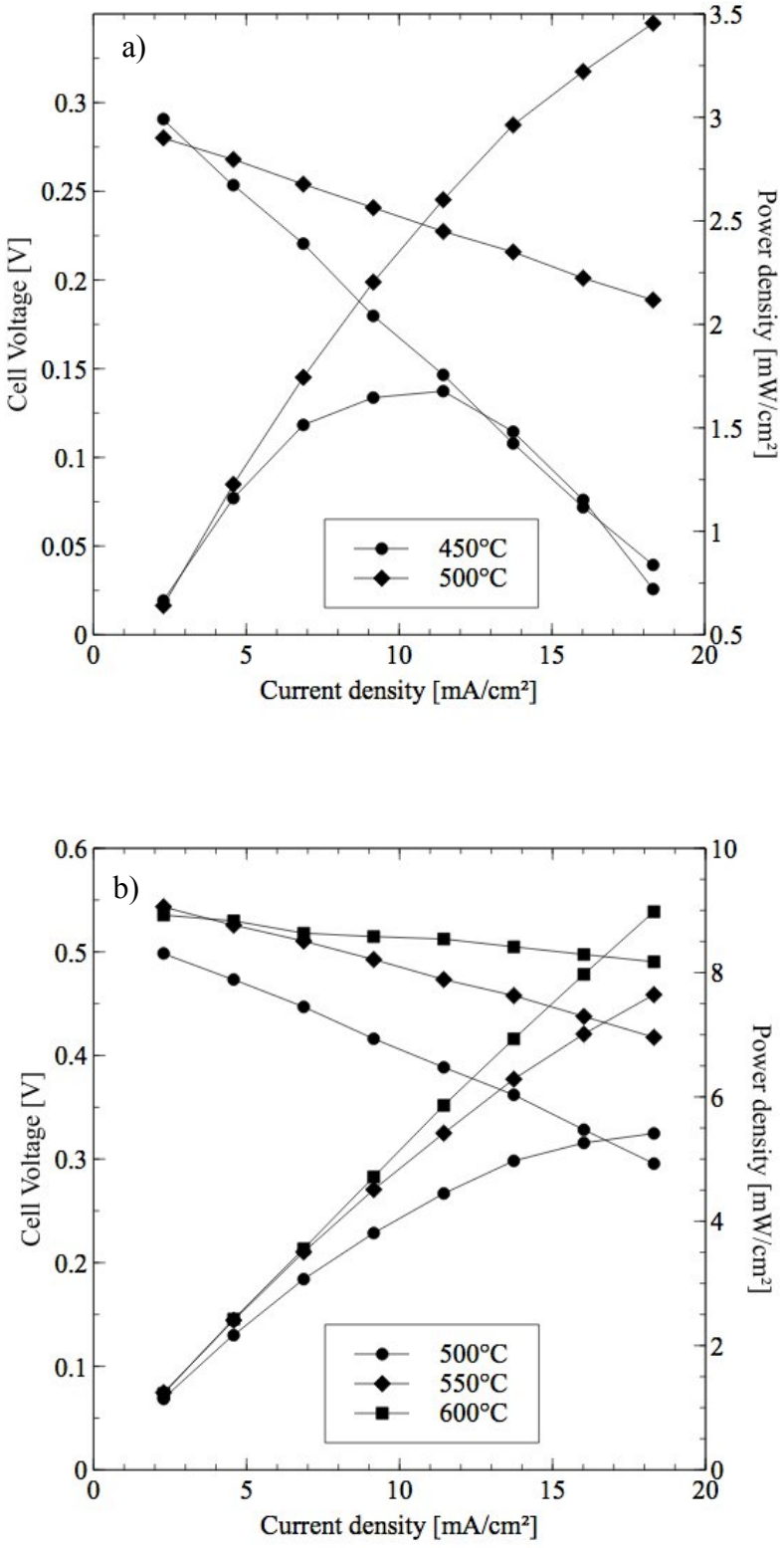

Fig. 6.8 I-V plot of the fuel cells with Bn5Li2 anode sintered at 970°C (a) and 1020°C (b) for 3h in H_2:N_2=1:1 flux.

6.4 Conclusions

SOFCs formulated with both copper oxides with thin and perfectly densified electrolytes (~10 μm) were obtained at temperature more than 500°C below the conventional sintering temperature for GDC10. The instability of cuprite in air and its tendency to oxidize required performing sintering in inert atmosphere. Then, some carbo-reduction of cuprite to metallic copper was unavoidable. Although cuprite-containing cells were fabricated, the partial oxidation of the anode during the reduction step, likely caused their failure before measuring their electrochemical performances.

Conversely, the use of tenorite (CuO) was less problematic owing to the possibility of sintering in oxidative atmosphere thus avoiding carbo-reduction reactions. The higher CET of tenorite resulted in a lower mismatch between anode and electrolyte, which allowed including more CuO and obtaining electrolytic surfaces without any detectable defects, even after reduction. When tested with hydrogen, these cells had a low OCV and failed at 550°C even with reserved testing conditions. Sintering at 1020°C resulted in a fully dense electrolyte with a fine grain structure, but resulted in cracks due to differential shrinkage. Despite this, the cell had a maximum OCV of 0.54 V and the highest measured power density was 8.98 $mW \cdot cm^{-2}$ with a peak power density projected to be 27.5 $mW \cdot cm^{-2}$.

These values are lower than those measured in other systems with copper-containing anodes†, although the comparison is believed to be inadequate because there are no examples of cell made with similar materials, architecture and fabrication technique in the literature. It is expected that the performance can be further improved by increasing the electrodes porosity by using suitable pore-formers. In addition, the use of finer CuO powder could result in an additional decrease of the required content for guaranteeing the electronic percolation, further decreasing the CET mismatch and the issues related to the presence of fractures.

References

1. P A Korzhavyi, B. J. Literature review on the properties of cuprous oxide Cu2O and the process of copper oxidation. 1–41 (2012).
2. Zhu, Y., Mimura, K. & Isshiki, M. Oxidation mechanism of Cu2O to CuO at 600–1050 C. *Oxidation of Metals* **62**, 207–222 (2004).
3. Atkinson, A. & Selcuk, A. Residual stress and fracture of laminated ceramic membranes. *Acta Materialia* **47**, 867–874 (1999).

† *see Section 2.4 for a complete review.*

7. Conclusions

The production of tubular SOFCs supported by a cermet anode formulated with copper was successfully achieved. The optimization and the experience developed in the process of extrusion allowed to produce the composite anodes quickly and with good reliability. The low melting temperature of copper and its two oxides imposed a limit on the maximum temperature reachable during co-sintering of the cell. The study of the effect of different sintering aids on the densification of the GDC10 permitted to select Li_2O as the most effective, being able to enhance the sinterability of the material and to decrease of more than 600°C its sintering temperature. Although its effect was remarkable, the densification of the thin electrolytic layer when bonded to the supporting anode could not be accomplished without analyzing and solving the issues related to its constrained sintering. A complete cell with a 10 um perfectly dense and crack free Li_2O-GDC10 electrolyte, Li_2O-GDC10:Cu_2O 75:25 vol% anode and GDC10:LSF20 50:50 vol% cathode was obtained after one step sintering for 3h at 1020°C in argon atmosphere. The co-sintering permitted perfect adhesion of the three layers and no sign of debonding. One of the main fabrication problems related to the employment of Cu_2O in the cermet anode was its low coefficient of thermal expansion that caused the onset of tensile stress in the electrolyte during cooling and the opening of brittle fractures on its surface. When the Cu_2O was increased to 35vol% to insure the electrical conductivity of the anode, the sintering temperature had to be decreased to 995°C to minimize the cracks formation, although this affected the densification of the electrolyte layer. Cells formulated with Cu_2O suffered from incomplete densification, cracks and oxidation of the cuprite during reduction. These issues made impossible to perform electrochemical tests.

Employment of CuO was less problematic, thanks to its resistance to oxidation and its higher CET. SOFCs were fabricated with Li_2O-GDC10 electrolyte, Li_2O-GDC10:CuO 60:40 vol% anode and GDC10:LSF20 50:50 vol% cathode. Sintering at 1020°C resulted in a fully dense electrolyte with a fine grain structure, although some cracks due to differential shrinkage could not be completely avoided. Despite this, the cell had a maximum OCV of 0.54 V and the highest measured power density was 8.98 mW cm^{-2} with a peak power density projected to be 27.5 mW cm^{-2} when tested at 600°C in dry H_2.

These results do show that SOFCs can be produced with a copper cermet anode using similar methods used with NiO-based anodes by a one-step firing procedure at relatively low temperatures, thus having cost and high energy savings. The use of copper can allow for the use of light hydrocarbons in the cell without external reforming equipment or need of high steam to carbon ratio, and without the risk of carbon deposition in the cell.

Ringraziamenti

Ringrazio il mi babbo e la mi mamma, Marco e Tiziana per essere i migliori genitori che io conosca. Senza il loro continuo incoraggiamento e la loro fiducia niente sarebbe stato possibile.
Ringrazio Carli, il mio amore, che mi sopporta anche quando sono insopportabile. Spero che continui a farlo per il resto della nostra vita.
Ringrazio John, un amico insostituibile ed un collega eccezionale che mi ha insegnato a fare ricerca.
Ringrazio i miei fratelli anche se sono figlio unico perché sono tutti speciali a modo loro e spero che la nostra amicizia duri per sempre.
Ringrazio la musica, perché senza non potrei vivere.
Ringrazio gli amici del laboratorio, Livio e Alexia che ha passato un momento difficile ma sono sicuro che tornerà più forte di prima.
Ringrazio Alessandro e Dario per avermi aiutato a testare le celle, mettendoci la passione come se fossero le loro. Ringrazio Massimiliano per averci provato.
Ringrazio le persone che mi hanno voluto bene in questi quattro anni a Trento e tutti gli amici che ho conosciuto ma in particolar modo ringrazio le persone che non mi hanno voluto bene perché mi hanno fatto capire che non si può piacere a tutti, e va bene così.

Infine ringrazio il Prof. Sglavo perché ha creduto in me fin da quando ci siamo conosciuti e perché mi ha dato la possibilità di scoprire cosa mi piace davvero fare.

Grazie,

Andrea